THESIS

Optical Loss Study of Molecular Layers Using a Cryogenic Folded Cavity for Future Gravitational-wave Detectors

Satoshi Tanioka
Department of Astronomical Science
School of Physical Sciences
SOKENDAI (The Graduate University for Advanced Studies)

January, 2021

Abstract

The first direct detection of gravitational-wave (GW) opened a new window to the Universe. A number of detections of GWs have been reported, and the existence of intermediate mass black hole was revealed. The Einstein Telescope (ET), a 3rd-generation gravitational-wave detector (GWD) in Europe, and LIGO Voyager, a substantial upgrade of aLIGO, are planning to employ cryogenic silicon mirrors to reduce thermal noise. It is expected that such future cryogenic GWDs will enable us to constrain the formation process of such massive black holes or discover new GW sources with improved sensitivity. The realization of cryogenically cooled mirror is an important key and big challenge to achieve the future cryogenic GWDs.

In the future GWDs such as the ET and LIGO Voyager, a molecular layer formed on the cryogenic mirror surface can become one of the problems due to its optical loss. We theoretically estimated the optical loss induced by the molecular layer and revealed that the optical absorption induced by the molecular layer can exceed the cooling capacity even if its thickness is only 1 nm, which can hinder the cryogenic operation.

We developed 10 K folded optical cavity to investigate the optical loss of not only the coatings but also the molecular layer. In this experiment we realized the cryogenic optical cavity with folded configuration for the first time ever, and achieved cavity enhanced ellipsometry at both room temperature and cryogenic temperature. These measurements enabled the characterization of the molecular layer even if its thickness is only a few nm.

Besides, we simulated the molecular layer formation rate for the case of the ET and LIGO Voyager. The results show the molecular layer formation can become a problem for long term operation. Finally, based on the experimental study here, we propose a monitoring system which probe the cryogenic mirror surface and measure the thickness of molecular layer. Such monitoring system will be able to identify the molecular layer formation and be useful not only operation but also commissioning works.

The theoretical and experimental works have investigated the feasibility of the future cryogenic GWDs. This thesis reports the details of these results.

Contents

Acronyms

AOM	acoust-optical modulator
ASC	alignment sensing and control
AR	anti-reflective, anti-reflection
BS	beam splitter
CEE	cavity enhanced ellipsometry
CLIO	Cryogenic Laser Interferometer Observatory
CML	cryogenic molecular layer
CTN	coating thermal noise
DC	direct current
DoF	degrees of freedom
DRSE	detuned resonant sideband extraction
EOM	electro-optic modulator
ET	Einstein Telescope
ETM	end test mass
FI	Faraday isolator
FP	Fabry-Perot (cavity)
FSR	free spectral range
FWHM	full width at half maximum
GW	gravitational wave
GWD	gravitational-wave detector
HR	high-reflection
HWP	half-wave plate
IMC	input mode cleaner
ISCO	innermost stable circular orbit
ITM	input test mass
PBS	polarizing beam splitter
PD	photodetector, photodiode
PDH	Pound-Drever-Hall (method)
PRG	power recycling gina
PZT	piezoelectric transducer
QPD	quadrant photodiode
QWP	quarter-wave plate
WFS	wavefront sensing

Introduction

First of all, the purpose of this thesis is to study the feasibility of future cryogenic gravitational-wave detectors in terms of the optical loss induced by the molecular layer formed on the cryogenic mirror surfaces.

There have been large efforts to directly observe gravitational-wave (GW) with the ground-based laser interferometric detectors. In order to detect GWs, so-called 2nd generation interferometers such as advanced LIGO, advanced Virgo, and KAGRA were built. Advanced LIGO achieved direct detection of GW from a binary black hole system in 2015, and the new window to probe the Universe was opened. Following observing run, advanced LIGO and advanced Virgo detected a GW from a binary neutronstar merger. So far, a number of detection of GW events are reported by them.

Future gravitational-wave detectors (GWDs) are planning to employ cryogenically cooled mirrors to improve the sensitivity by reducing thermal noise. A cryogenically cooled mirror is an important key and a challenge for the realization of future GWDs.

Difficulties in such cryogenic mirror come from several facts. One is that the development of high-end mirror substrate and coatings. Both mirror substrate and coatings need to have not only small optical loss, but also small mechanical loss. Development of such state-of-the-art mirrors is indispensable. Another is that the issue of frosting of mirrors, which is caused by the adsorption of residual gas molecules. An adsorption of molecules on the mirror surface induces unwanted optical loss, resulting in degradation of the sensitivity. Therefore, the investigation in the impacts by frosting on a cryogenic mirror is important to realize the future GWDs.

In this thesis, a development of optical loss characterization system, and a theoretical study and experimental studies of the molecular layer formation on the mirror surface are presented. It is shown that the optical loss in the cryogenically cooled mirrors in future GWDs can exceed the requirement due to the adsorption of molecules. In addition, the optical loss estimation by a cryogenic folded cavity is demonstrated. Moreover, a study using Monte-Carlo simulation, which can predict the molecular layer formaton rate on the mirror

surface is presented, and a monitoring system for cryogenic mirror surface are presented based on the folded cavity experiment. Thus the study presented in this thesis should play an important role to design and construct the future GWDs.

The following paragraphs are dedicated to explain the contents of this thesis.

Chapter 1 briefly describes the background of this research, In this chapter, the derivation of GW, its astrophysical sources and an introduction of the laser interferometric GWDs are given.

Chapter 2 describes several cryogenic GWDs and their features. KAGRA is a cryogenic GWD, and the author contributed to its first cryogenic test operation and first observation. In addition, one of the most critical problems in KAGRA which can also happen in the future GWDs is described — molecular layer formation on a cryogenically cooled mirror. This problem is the one of the motivation of this thesis.

Chapter 3 describes the theoretical calculation of the optical loss induced by cryogenic molecular layer (CML). Theoretical estimation shows remarkable optical absorption by the CML in future cryogenic GWDs, and exceed the cooling capacity even if its thickness is a few nanometer. The results are published as an article by the author.

Chapter 4 explains a cryogenic folded cavity to measure an optical loss at a mirror surface which is developed by the author. The cryogenic folded cavity has not been realized so far, and this is the first time ever. This device currently enables the optical loss measurement at broadband temperature range. The optical setup and measurement methods are introduced. The cavity enhanced ellipsometry is also introduced in this section. The spacer for the cavity was designed by the author using 3D CAD soft, and manifactured by the company. The installation of this setup was done by the author.

Chapter 5 describes the experimental results to evaluate the optical loss in the mirror. Furthermore, the measurement of optical loss induced by the CML is also estimated by combining the ringdown and cavity enhanced ellipsometry. The author built the model to analyze the results of cavity enhanced ellipsometry. The characterization of the CML by cavity enhanced ellipsometry is presented for the first time by the author.

Chapter 6 describes the implications to the cryogenic GWDs. Here a simulation is done by the author to estimate the CML formation for the case of future GWDs. The model for the simulation was made by the author. Possible solutions to avoid the affects of CML is also introduced here. The monitoring system for CML formation on mirror surface is proposed here by the author inspired by the cryogenic folded cavity experiment.

Chapter 7 describes the summary and conclusion of this thesis.

Appendix A is dedicated for the upgrade of this setup for direct measurement of coating thermal noise. Low thermal noise coatings at cryogenic temperature is a key to realize the future GWDs. The cryogenic folded cavity will enable direct measurement of coating thermal noise directly which promotes the development of high-end coatings. A possible upgrade plan toward the direct measurement of coating thermal noise, and related noise sources are introduced.

Appendix B is dedicated for the analytical calculation of angular response which enables the compute WFS signals of an optical cavity with less cost. The original ides of this method was proposed by the collaborator of the author. A further analysis and interpretation was done by the author.

Chapter 1

Background

A direct detection of gravitational-wave (GW) is a challenging because the interaction of gravity with masses is remarkably weak. A creation of GW with a detectable amplitude in a laboratory is impossible with the current technologies. In order to detect GWs, one have to rely on astronomical sources, which can be extremely massive and highly accelerated. From this point of view, astronomy and GW are inseparable. Moreover, the detection of GWs from astronomical sources provides us unique information of the Universe. This is because GWs are unaffected by the matter they encounter.

The laser interferometric GW detector is in mainstream, and it is most sensitive at around 100 Hz. In 2015, Advanced LIGO (aLIGO) constructed in America detected the GW from binary black hole merger. This first direct detection of GW opened a new window to the Universe — this window is called Gravitational-wave Astronomy. In 2017, aLIGO and Advanced Virgo in Europe detected a GW from binary neutron star merger, and the electromagnetic counterpart was also observed by telescopes. The sensitivity of the detector has been continuously improved over the course of the years and dozens of detection are achieved by aLIGO and Virgo.

This chapter is dedicated to explaining GW astronomy and the laser interferometric detector as a background of this thesis. First, we briefly introduce the derivation of GW based on the general theory of relativity. Second, we describe the astrophysical sources of GW. Then, we introduce the laser interferometric detector and its noise sources.

1.1 Nature of Gravitational-waves

GW is a ripple of space-time and propagates as a wave at the speed of light. GW was predicted by A. Einstein on the basis of the general theory of relativity

[1, 2].

GW is derived form Einstein's equation within the scheme of the general theory of relativity. In the theory, gravitation is considered as distortion in space-time, expressed by a physical quantity called the metric. Moreover, the metric follows Einstein's equation which contains the second derivative of the metric with respect to time. Thus, the metric can evolve as a function of time. In fact, a small perturbation in the metric can propagate as a wave through space-time.

1.1.1 GW as a Solution of Einstein's Equation

In this subsection, we review the derivation of GWs which can be derived as a solution of Einstein's equation when a small perturbation in space-time is introduced [3].

The interval of two separated events in space-time is described with the metric tensor $g_{\mu\nu}$ as,

$$ds^2 = g_{\mu\nu} dx^\mu dx^\nu, \tag{1.1}$$

where Greek indices run from 0 to 3, so that $\mu, \nu = 0, 1, 2, 3$. With this notation, space-time can be simply expressed by $x^\mu = (ct, x, y, z)$.

Einstein's equation, which is the most important equation, is expressed as

$$R_{\mu\nu} - \frac{1}{2} R g_{\mu\nu} = \frac{8\pi G}{c^4} T_{\mu\nu}, \tag{1.2}$$

where the left-hand side represents the geometrical nature of space-time and the right-hand side represents the mass and energy of the system. Here, $R_{\mu\nu}$, $R = g^{\mu\nu} R_{\mu\nu}$, and $T_{\mu\nu}$ are the Ricci tensor, the Ricci scalar curvature, and the stress-energy-momentum tensor, respectively.

We consider the case that a small perturbation, $h_{\mu\nu}$, is introduced to the flat space-time as

$$g_{\mu\nu} = \eta_{\mu\nu} + h_{\mu\nu}. \tag{1.3}$$

Assuming vacuum, $T_{\mu\nu} = 0$, then applying the above equation to Eq. 1.2, and neglecting the higher order terms while leaving the first order terms of h, one can obtaing the linearized Einstein's eq,

$$\left(-\frac{1}{c^2} \frac{\partial^2}{\partial t^2} + \frac{\partial^2}{\partial x_i^2} \right) h_{\mu\nu} = 0. \tag{1.4}$$

This describes the propagation of GW $h_{\mu\nu}$ as a three-dimensional wave which travels at the speed of light.

When we choose a spatial coordinate such that a GW travels in the z direction, the plane wave solution can be summarized as,

$$h_{\mu\nu} = A_{\mu\nu} \exp[i\omega_g(t - z/c)], \tag{1.5}$$

where

$$A_{\mu\nu} = \begin{pmatrix} 0 & 0 & 0 & 0 \\ 0 & h_+ & h_\times & 0 \\ 0 & h_\times & -h_+ & 0 \\ 0 & 0 & 0 & 0 \end{pmatrix}. \tag{1.6}$$

Here ω_g is the angular frequency of the GW, h_+ and $h_\times$ are independent constants.

1.1.2 Polarization

We consider a case where two free particles are placed at separated locations — one at the origin of the coordinate and the other at $x^i = (L, 0, 0)$. Suppose that each of them is at rest initially, and GW passes along the z-axis. The proper distance between them, L', can be expressed as

$$L' \equiv \int |ds^2|^{1/2} = \int_0^L |g_{11}|^{1/2} dx \approx L + \frac{1}{2} h_{11} L. \tag{1.7}$$

Therefore, GW changes the proper distance when it passes through. The amount of change in the distance, $\Delta L \equiv L' - L$, is proportional to both the initial distance L and amplitude h.

As shown in Fig. 1.1, there are two independent polarizations in GWs — amplitude of which are expressed as h_+ and $h_\times$, and they are referred as *plus*- and *cross*-mode, respectively. In order to understand the characteristic of those modes, consider a similar thought experiment in which a plane wave passes through along z-axis with a number of free particles arranged on the x-y plane. According to Eq. 1.7, if an initial proper distance between them was $L^i = (L^x, L^y, 0)$, the displacement ΔL can be written as

$$\begin{pmatrix} \Delta L^x \\ \Delta L^y \end{pmatrix} = \frac{1}{2} \begin{pmatrix} h_+ & h_\times \\ h_\times & h_+ \end{pmatrix} \begin{pmatrix} L^x \\ L^y \end{pmatrix} \exp[i\omega_g(t - z/c)], \tag{1.8}$$

$$= \frac{1}{2} h_+ \begin{pmatrix} L^x \\ L^y \end{pmatrix} \exp[i\omega_g(t - z/c)] + \frac{1}{2} h_\times \begin{pmatrix} L^y \\ L^x \end{pmatrix} \exp[i\omega_g(t - z/c)]. \tag{1.9}$$

Fig. 1.1 shows how free particles respond to GWs for both the plus- and cross-modes. The plus mode distorts space as a "plus"-shape, while the cross mode makes it a "cross"-shape.

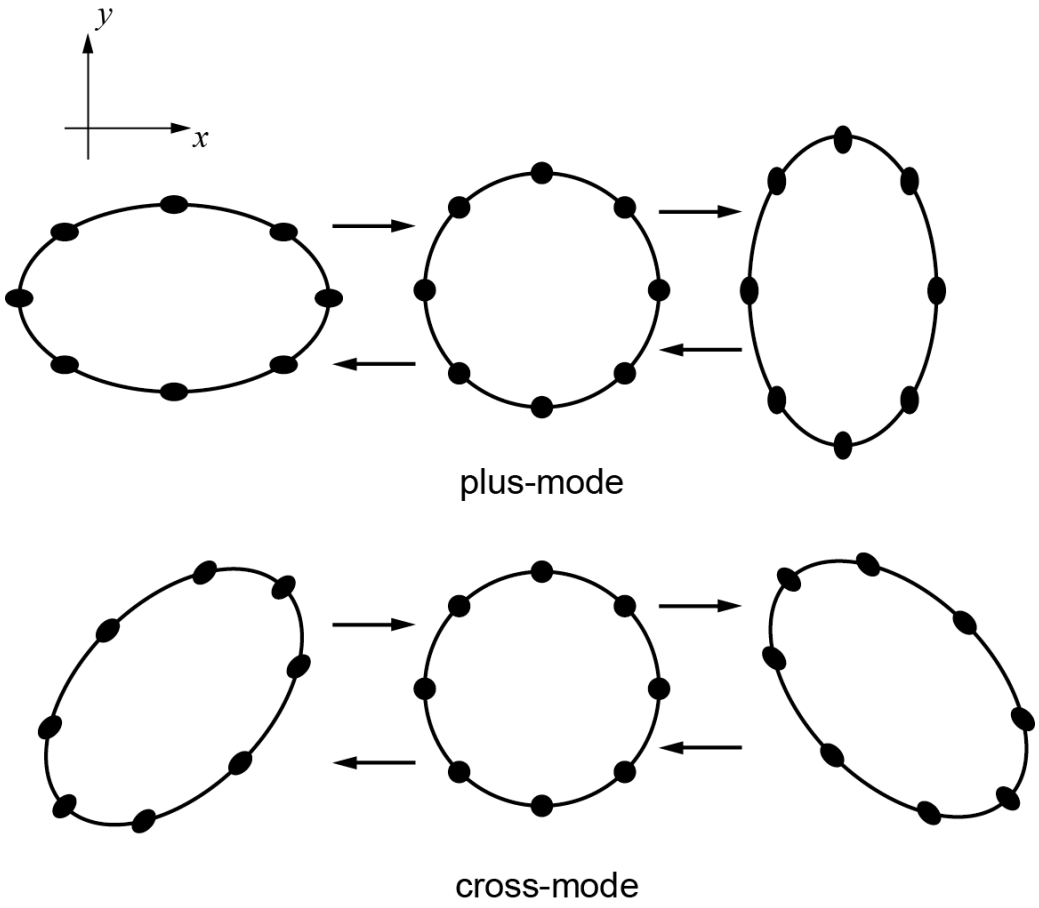

Figure 1.1: Polarization of gravitational-wave. Upper figure shows the plus-mode, and lower shows the cross-mode, respectively.

1.1.3 Radiation

GWs can be radiated by masses when they accelerate similarly to the radiation of electro-magnetic waves which are generated by a charged particle when it accelerates. A big difference, however, is that the radiation of GW requires a quadrupole moment though electro-magnetic radiation is induced by a dipole moment.

First, we consider the Lamor formula as an example which denotes the luminosity of an electro-magnetic waveL_{e} as

$$L_{\mathrm{e}} = \frac{2}{3c^2}\ddot{\boldsymbol{d}}^2, \tag{1.10}$$

where $\boldsymbol{d} = \sum_i q_i \boldsymbol{r}_i$ is the sum over the electric dipole moment of charged

particles.

For the case of the radiation of GW, the GW luminosity, $L_{\rm g}$, becomes

$$L_{\rm g} \propto \frac{G}{c^3}\ddot{\boldsymbol{d}}^2, \ddot{\boldsymbol{d}}^2 = \sum_i m_i \ddot{\boldsymbol{r}}_i = \sum_i \dot{\boldsymbol{P}}_i, \tag{1.11}$$

where $\boldsymbol{P}_i$ is the kinematic momentum of i-th particle. Instead of charged particles, the kinematic momentum is introduced as GW is generated from masses. However, as the kinematic momentum is always conserved in an isolated system, the kinematic dipole $\boldsymbol{d}$ does not evolve as a function of time. Therefore, GW cannot be radiated by a kinematic dipole moment.

The next lowest moment is the quadrupole moment. By introducing the mass quadrupole moment I_{jk}, a GW version of Lamor formula [4] can be expressed as,

$$L_{\rm g} = \frac{G}{5c^5}\langle(\dddot{I}_{jk})^5\rangle, \tag{1.12}$$

$$I_{jk} \equiv \sum_A m_A \left[x_j^A x_k^A - \frac{1}{3}\delta_{jk}\left(x^A\right)^2\right], \tag{1.13}$$

where A represents the label of A-th particle. Therefore, radiation of GW requires a quadrupole moment so as to evolve as a function of time.

Order Estimation of Radiated Energy

Here, we briefly show the energy of gravitational wave radiation from Eq. 1.12. The third derivative of the quadrupole moment with respect to the time scales as

$$\dddot{I}_{ij} \sim \frac{MR^2}{T^3} \sim \frac{Mv^3}{R}, \tag{1.14}$$

where M, R, T, and v are the typical mass, spatial size, time scale, and velocity of the system, respectively. Plugging Eq. 1.14 into Eq. 1.12, one can obtain

$$L_{\rm g} \sim 1.8 \times 10^{58} \left(\frac{R_{\rm sch}}{R}\right)^2 \left(\frac{v}{c}\right)^6 \ [\rm erg/s], \tag{1.15}$$

where $R_{\rm sch} \equiv 2GM/c^2$ is the Schwarzschild radius. Considering the case of an astronomical system which is bounded by its self-gravity, the kinetic energy and the potential energy are comparable, so that

$$Mv^2 \sim \frac{GM^2}{R}. \tag{1.16}$$

With this relation, the luminosity 1.15 can be rewritten as

$$L_{\mathrm{g}} \sim 2.3 \times 10^{57} \left(\frac{R_{\mathrm{sch}}}{R} \right)^{5} \ [\mathrm{erg/s}]. \tag{1.17}$$

This result indicates that the GW luminosity depends on the size of the object. This is the reason why the compact stars are considered as the main GW sources.

Order Estimation of Amplitudes

We estimate the order of the amplitude of GW, h, based on the approximation [4]

$$h \sim \frac{R_{\mathrm{sch}}}{r} (v/c)^2, \tag{1.18}$$

where r is the distance between the GW source and an observer. The emission efficiency of GW can be parameterized as

$$\varepsilon \sim \left(\frac{R_{\mathrm{sch}}}{R} \right)^{7/2}. \tag{1.19}$$

Plugging Eq. 1.19 into Eq. 1.18, one can obtain

$$h \sim \varepsilon^{2/7} \frac{R_{\mathrm{sch}}}{2r} \sim 1.5 \times 10^{-21} \left(\frac{\varepsilon}{0.1} \right)^{2} /7 \left(\frac{M}{M_{\odot}} \right) \left(\frac{r}{17\,\mathrm{Mpc}} \right). \tag{1.20}$$

Here, the mass M and the distance r are scaled by the solar mass $M_{\odot} = 1.989 \times 10^{30}$ [kg] and that from the earth to the Virgo cluster of about 17 Mpc, respectively.

1.2 Sources of Gravitational-waves

In this section, we briefly review the GW sources, which have been observed or expected for the detection. More details can be seen in the reference [5].

1.2.1 Compact Binary Coalescence

A binary system formed by two compact objects such as a black hole or a neutronstar is one of the most promising sources of GW, and a number of compact binary coalescence have been detected [6]. A wave form of the compact binary coalescence is known as the chirp signal.

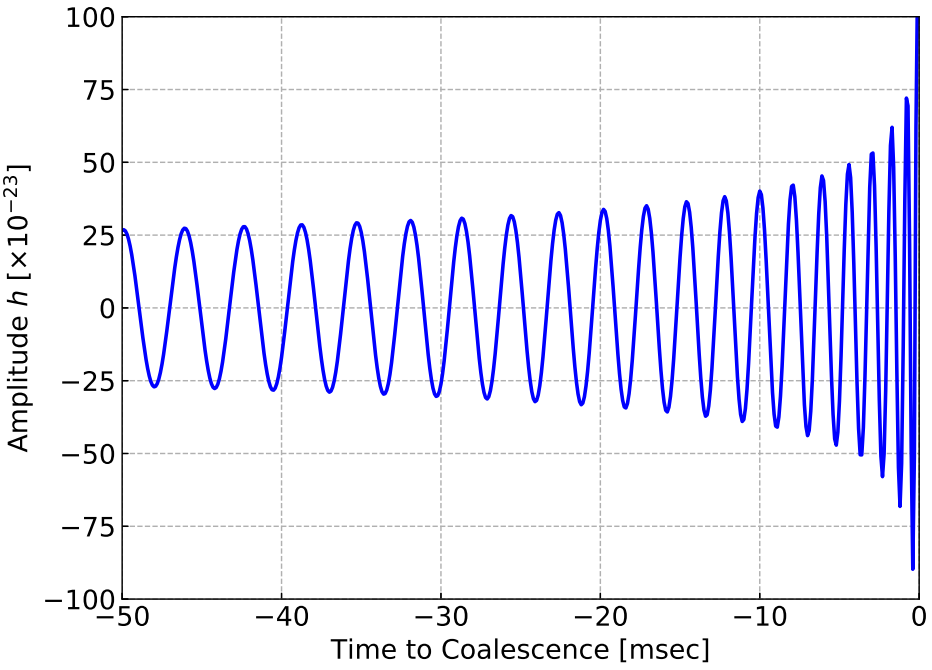

Figure 1.2: The calculated chirp signal from a $1.4M_{\odot}$-$1.4M_{\odot}$ neutronstar binary at the Virgo cluster of about 17 Mpc.

A chirp signal, f_{GW}, grows up as a function of the time. This is a consequence of the fact that the angular momentum of the system is deposited as the GW radiation. Therefore, the separation distance of the stars gradually becomes smaller, resulting in the frequency evolution of a signal. The frequency evolution of a chirp signal can be approximated as

$$f_{\mathrm{GW}} \approx 134\,\mathrm{Hz} \left(\frac{1.21M_{\odot}}{\mathcal{M}}\right)^{5/8} \left(\frac{1\,\mathrm{s}}{\tau}\right)^{-3/8}, \tag{1.21}$$

$$\mathcal{M} \equiv \frac{(m_1 m_2)^{3/5}}{(m_1 + m_2)^{1/5}}, \tag{1.22}$$

where τ is the time to coalescence, $\mathcal{M}$ is the chirp mass defined by the masses of the binary stars, m_1 and m_2. Fig. 1.2 shows how chirp signal evolves over time. The chirp signal from $1.4M_{\odot}$ binary neutronstar merger at the Virgo cluster is assumed.

A GW radiation in a chirp waveform ends when the orbital radius becomes

smaller than the innermost stable circular orbit (ISCO), where stable circular orbits are no longer allowed. Then the two stars plunge toward each other and coalesce. For the case of a nutronstar-neutronstar binary, when they are at the ISCO, the expected frequency $f_{\rm ISCO}$ is about 800 Hz.

In addition, such binary systems can be used as a standard siren [7]. When a chirp signal is detected, the amplitude provides the information of the luminosity distance. In addition to that, the frequency gives the information about the red shift. Thus, the detection of GW from such binary systems allows one to perform cosmological distance measurement.

1.2.2 Spin of Compact Stars

Spinning compact stars, such as pulsars, are expected to be sources of continuous GWs, frequency of which can be stable. In order to radiate GWs by the spin, the mass density must not be axisymmetric about the spin axis because the axisymmetric system does not have a quadrupole moment.

The expected amplitude of GW from a spinning of compact stars can be estimated as

$$h \approx 1.06 \times 10^{-25} \left(\frac{\epsilon}{10^{-6}}\right) \left(\frac{I}{10^{38}\,\mathrm{kgm}^2}\right) \left(\frac{10\,\mathrm{kpc}}{r}\right) \left(\frac{f_g}{1\,\mathrm{kHz}}\right)^2, \tag{1.23}$$

where ϵ is the ellipticity, I is the inertia along the spin axis. It should be noted that the frequency of the GW is twice of the actual spinning frequency $f_{\rm spin}$, hence $f_g = 2f_{\rm spin}$.

1.2.3 Supernovae

A supernova explosion can become a GW source because it dramatically accelerates a large amount of masses within a short time scale. If non-axisymmetric components are involved in the core collapse of supernovae, burst GW signals can be emitted.

The prediction of the waveform is, however, difficult because the explosion mechanism is uncertain. Assuming that the mass of a system is about $M_\odot$ and the characteristic velocity of $v/c \sim 0.1$, the amplitude can be estimated as

$$h \sim 9.6 \times 10^{-20} \left(\frac{10\,\mathrm{kpc}}{r}\right). \tag{1.24}$$

Therefore, a supernova in the Galaxy can be a target. Most of the explosion models suggest that the typical frequency is below 1 kHz, hence in the observational band of GWDs.

1.2.4 Stochastic Gravitational-wave Background

A stochastic GW background is expected to arise from a superposition of a number of unresolved GW sources. It can carry unique features from the early epochs of the Universe, which cannot be accessed by standard astronomical observations. Therefore, direct measurements of the amplitude of the stochastic background are important to understand the evolution of the Universe.

Recently a simultaneous observation of GWDs has set an upper limit on the spectral density of the GW background, hence the cosmological energy density of GW [8].

1.3 Laser Interferometric Gravitational-wave Detectors

Current terrestrial gravitational-wave detectors (GWDs) adopt laser interferometric technique and are based on the Michelson interferometer. The Michelson interferometer can be considered as an optical phase detector, while it is broadly used as a Fourier transform spectrometer in astronomical telescopes. Comparing the optical phase difference between each arm in the Michelson interferometer, one can detect a GW. The working principle is described in the following section.

1.3.1 Working Principle

As shown in Fig. 1.3, the concept of current ground-based GWDs are based on the Michelson interferometer with mirrors suspended by wires. The suspended mirror not only provides but also makes the mirrors effectively free masses longitudinally with respect to the propagation direction of the laser beam in the observational frequency range.

When GW passes through the interferometer, it modulates the optical length of each arm by ΔL at the same frequency. The lengths change is differential in each arm, resulting the change in the interferometric condition of the output laser field.

Therefore, GWs can be detected as an intensity variation at a photo detector (PD) placed at the output side of the Michelson interferometer. When the wavelength of the GW is much longer than thearm lengths, the amount of the change is proportional to the macroscopic arm lengths L, so that

$$\Delta L \sim hL, \tag{1.25}$$

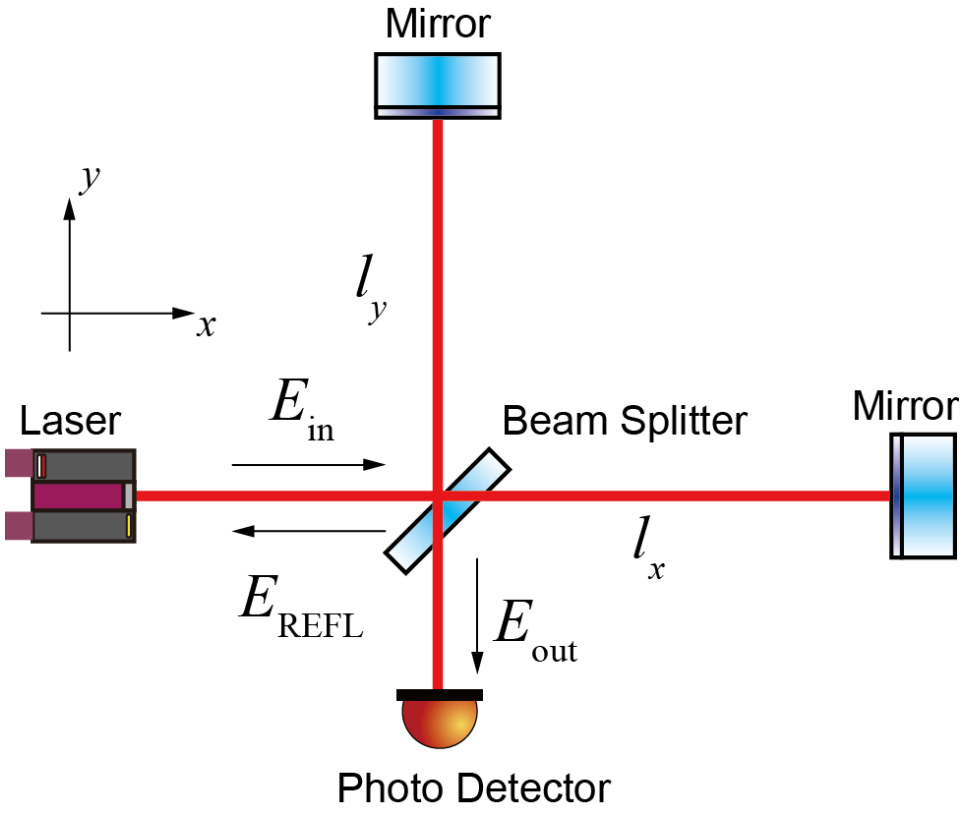

Figure 1.3: Schematic drawing of the Michelson interferometer.

where h is the amplitude of the GW. Thus, it is reasonable to construct a large size interferometer to increase the sensitivity.

In the following subsection, we see the principle of the detection of GWs by the interferometer.

Detection with Michelson Interferometer

The Michelson interferometer (MI) is an interferometric device which provides us the optical phase of laser field. It consists of a beam splitter (BS) and two end mirrors as shown in Fig. 1.3. The BS splits the laser beam into two paths — one is transmitted through it and the other is reflected. Each beam is reflected back to the BS by the end mirror and is re-combined which results in interference. At the detection port, called anti-symmetric (AC) port, a PD observes the power of the electric field.

We assume that a GW, polarizing in the plus-mode, passes along the z-axis through the MI placed in the x-y plane. The interval of two separated objects

can be expressed as

$$ds^2 = -(cdt)^2 + \{1 + h(t)\}dx^2 + \{1 - h(t)\}dy^2 + dz^2. \tag{1.26}$$

As the light travels along the world line of $ds^2 = 0$, the light traveling on the x-axis satisfies

$$cdt = \sqrt{1 + h(t)}dx. \tag{1.27}$$

By integrating dx over the round trip path from the BS to the end mirror, one can obtain

$$\int_{t-\tau_x}^{t} \frac{t'}{\sqrt{1 + h(t')}} dt' \approx \int_{t-\tau_x}^{t} \left\{1 - \frac{1}{2}h(t')\right\} dt' = \frac{2l_x}{c}, \tag{1.28}$$

where τ_x represents the duration for the light to round-trip in the x arm and l_x denotes the length of x arm. Therefore, τ_x can be calculated as

$$\begin{aligned} \tau_x &= \frac{2l_x}{c} + \frac{1}{2}\int_{t-\tau_x}^{t} h(t')dt' \\ &\approx \frac{2l_x}{c} + \frac{1}{2}\int_{t-2l_x/c}^{t} h(t')dt'. \end{aligned} \tag{1.29}$$

As $h \ll 1$, τ_x can be approximated by $2l_x/c$. Therefore, the net change in the optical phase is

$$\phi_x = \omega_0\tau_x = \frac{2\omega_0 l_x}{c} + \frac{\omega_0}{2}\int_{t-2l_x/c}^{t} h(t')dt', \tag{1.30}$$

where ω_0 is the angular frequency of the laser field. In the right-hand-side of the equation, the first term denotes the static phase rotation due to the light traveling a length of $2l_x$ while the second term denotes the phase derivation induced by the GW. The net phase change of the light traveling along the y arm is acquired in the same manner and expressed as

$$\phi_y = \omega_0\tau_y = \frac{2\omega_0 l_y}{c} - \frac{\omega_0}{2}\int_{t-2l_y/c}^{t} h(t')dt', \tag{1.31}$$

where the l_y is the length of the y arm.

Assuming that the arm lengths are almost identical, $l_x \approx l_y = l$, the phase difference between that of x and y arm is

$$\phi_x - \phi_y = \frac{2\omega_0(l_x - l_y)}{c} + \Delta\phi_g, \tag{1.32}$$

where

$$\Delta\phi_g \equiv \omega_0 \int_{t-2l/c}^{t} h(t')dt'. \tag{1.33}$$

The GW changes the interference condition, and it can be observed as power fluctuation at the PD. Assuming that a GW has a long wavelength such that the induced phase shift does not vary as fast as the round trip time of $2l/c$, it is approximated as,

$$\Delta\phi_g \approx \frac{2\omega_0 l}{c} h. \tag{1.34}$$

Frequency Response of the Michelson Interferometer

Assuming that a GW is monochromatic and has an angular frequency of $\omega_{\rm g}$, it can be expressed as,

$$h(t) = he^{i\omega_{\rm g}t}. \tag{1.35}$$

Plugging this into Eq. 1.33, one can obtain the frequency response of a Michelson interferometer to a GW as [9]

$$H_{\rm MI}(\omega_{\rm g}, l) \equiv \frac{\Delta\phi_{\rm g}}{he^{i\omega_{\rm g}t}} = \frac{2\omega_0}{\omega_{\rm g}} \sin\left(\frac{\omega_{\rm g} l}{c}\right) e^{-i\frac{\omega_{\rm g} l}{c}}. \tag{1.36}$$

The response curve is shown in Fig. 1.4 when the length of both arms is set to be 3 km. At low frequencies the response can be approximated as

$$H_{\rm MI} \approx \frac{2\omega_0 l}{c}. \tag{1.37}$$

When the frequency of GW becomes higher than the inverse of the round trip time $c/2l$, the above approximation is not valid any more because the phase of the GW signal starts cancellation during the light trips in the arms. This effect appears as a cut off in the response curve in figure 1.4.

1.3.2 Enhancement by the Fabry-Perot Arm Cavities

The optical cavity or equivalently Fabry-Perot (FP) cavity is a device formed by two or more partial reflectors to store photons (or to reject them) in the cavity. In particular, those formed by two mirrors facing each other is known as the FP cavity, as depicted in Fig. 1.6. In order to increase the sensitivity with a given arm length, the Fabry-Perot (FP) cavity is embedded in each arm

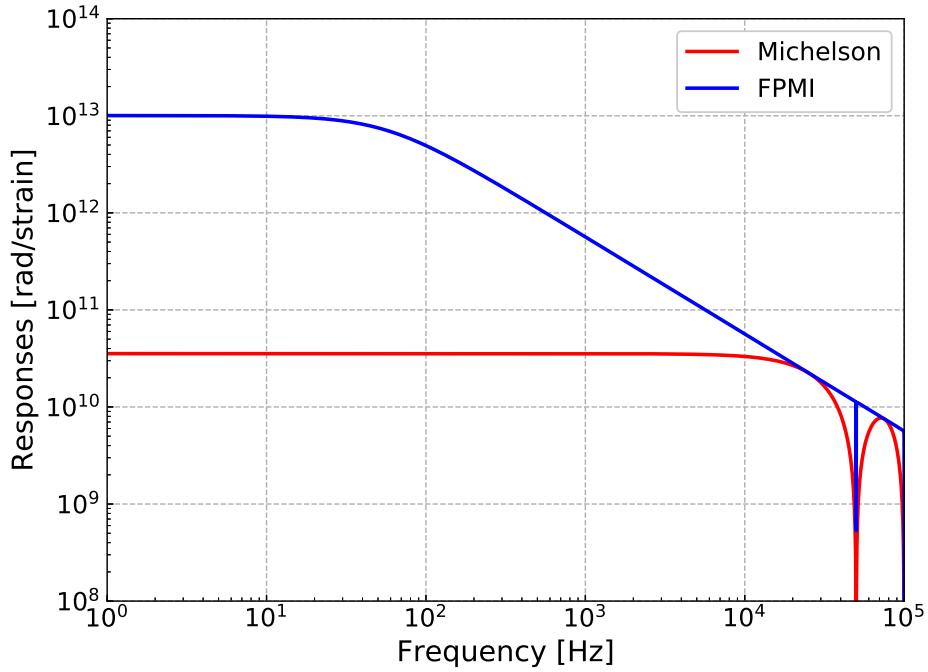

Figure 1.4: Frequency responses of the Michelson and Fabry-Perot Michelson interferometers. In both cases, the length of the arms are assumed to be $l = 3\,\mathrm{km}$. For the Fabry-Perot Michelson configuration, $t_1^2 = 0.014$, and $t_2^2 = 50\,\mathrm{ppm}$ are assumed.

of the Michelson interferometer. The optical configuration is shown in Fig. 1.5. Employing the FP arm cavity enables the laser field to bounce multiple times in the arm, and the interaction time of the light with GWs is increased. In other words, the effective length of the arm is elongated.

Here we describe the response of the FP Michelson interferometer. First, we will focus on a single FP cavity as shown in Fig. 1.6. Then we introduce a perturbation which is due to GW. Successively, we derive the response of the single cavity. Finally, we compute the response of the FP Michelson interferometer.

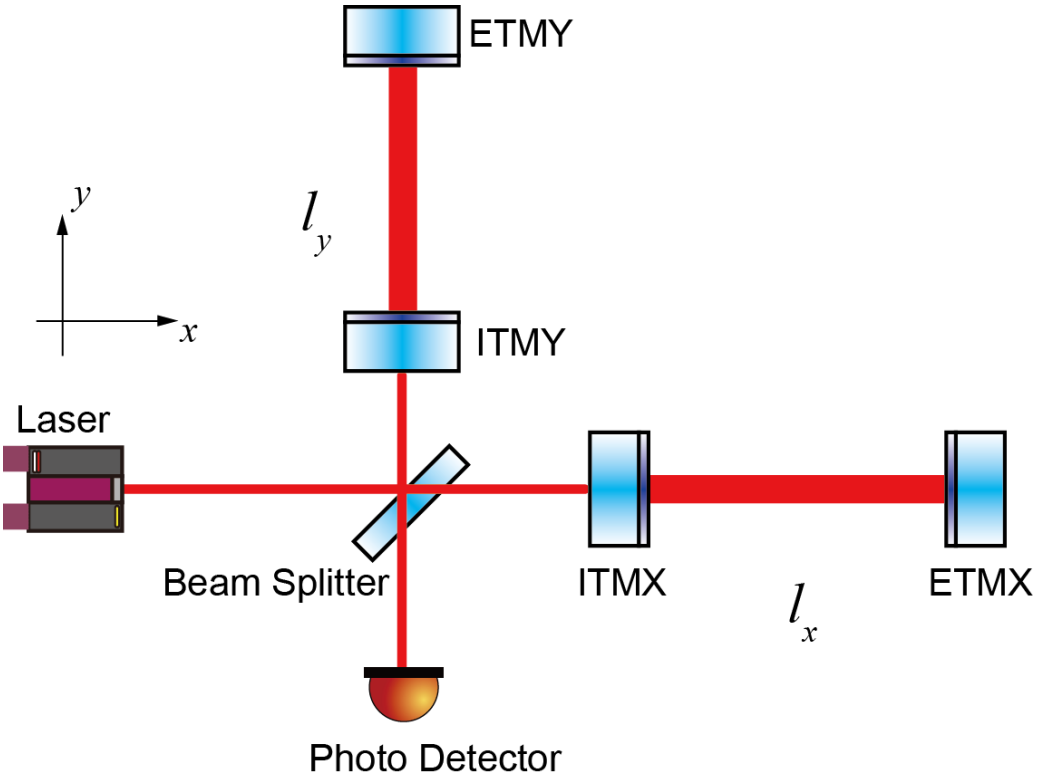

Figure 1.5: Schematic drawing of FPMI.

Response of a Single Fabry-Perot Cavity to a Perturbation

We consider a static case of a single FP cavity. A set of the field equations can be written as

$$E_{\rm cav}(t) = t_1 E_{\rm in} + r_1 r_2 E_{\rm cav}(t-2T)e^{-i\Delta\phi(t)}, \tag{1.38}$$

$$E_{\rm r}(t) = -r_1 E_{\rm in} + t_1 r_2 E_{\rm cav}(t-2T)e^{-i\Delta\phi(t)}, \tag{1.39}$$

where $E_{\rm in}(t)$, $E_{\rm cav}(t)$, and $E_{\rm r}(t)$ are the incident, intra-cavity, and reflected fields, respectively. r_j and t_j are the amplitude reflectivity and transmissivity of j-th mirror. L represents the distance between two mirrors, $T \equiv L/c$ is the one way trip time, and $\Delta\phi$ denotes the phase rotaion. From Eq. 1.30, the phase shift can be redefined as

$$\Delta\phi(t) = \frac{\omega_0}{2}\int_{t-2L/c}^{t} h(t')dt'. \tag{1.40}$$

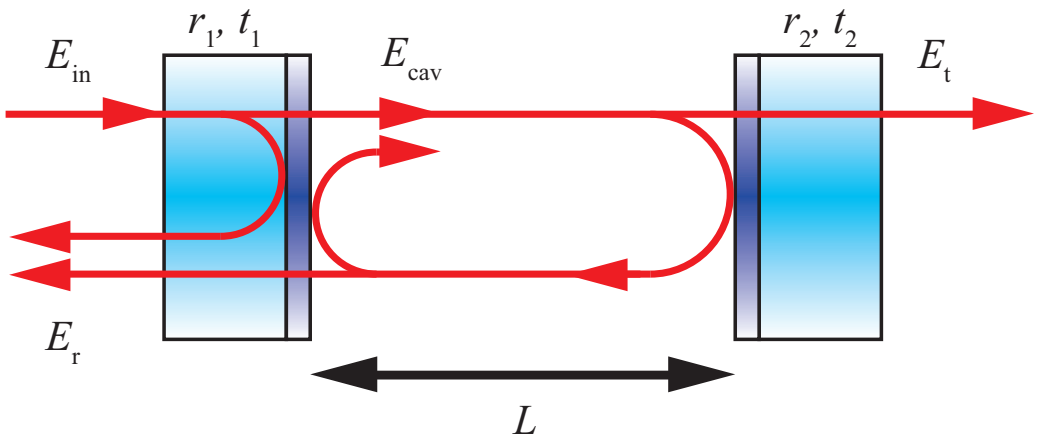

Figure 1.6: The schematic drawing of the Fabry-Perot cavity with two mirrors.

Here we assumed that the FP cavity is kept on resonance, i.e., the static phase rotation satisfies $2\omega_0 L/c = 2\pi n$ with n and integer. Therefore, $\Delta\phi$ is induced purely by GW in this case.

Suppose that $\Delta\phi$ introduces a small perturbation in the intra-cavity field. In this case, the intra-cavity field can be redifined as

$$E(t) = \bar{E} + \delta E(t), \tag{1.41}$$

where $\bar{E}$ is the static solution and $\delta E(t)$ represents the deviation from the static solution. We assume that the phase resolution is so small that the phase term can be approximated by

$$e^{-i\Delta\phi} \approx 1 - i\Delta\phi. \tag{1.42}$$

Plugging Eqs. 1.41 and 1.42 into Eq. 1.38, we obtain

$$\bar{E}_{\rm cav} + \delta E(t) \approx -r_1 E_{\rm in} + r_1 r_2 \bar{E} + r_1 r_2 \delta E(t - 2T) - i r_1 r_2 \bar{E}\Delta\phi. \tag{1.43}$$

Here we ignored higher order terms which contain the product of $\Delta\phi$ and $\delta E_{\rm cav}$. Using the static solution, $\bar{E} = t_1 E_{\rm in} + r_1 r_2 \bar{E}$, we can obtain

$$\delta E(t) = r_1 r_2 \delta E(t - 2T) - i r_1 r_2 \bar{E}\Delta\phi. \tag{1.44}$$

By applying the Laplace transform, the fluctuation in the intra-cavity fields can be expressed by

$$\delta E_{\rm cav}(s) = -i\frac{r_1 r_2 \bar{E}}{1 - r_1 r_2 e^{-2sT}}\Delta\phi(s). \tag{1.45}$$

This is the deviation introduced by the GW in the intra-cavity field.

Combining Eqs. 1.38 and 1.39, one can obtain

$$E_{\rm r}(t) = \frac{t_1}{r_1}E(t) - \frac{t_1^2 + r_1^2}{r_1}E_{\rm in}. \tag{1.46}$$

A deviation in the intra-cavity field $\delta E_{\rm cav}$ leads to a small deviation in the reflected field via

$$\delta E_{\rm r}(s) = \frac{t_1}{r_1}\delta E_{\rm cav}(s). \tag{1.47}$$

From Eqs. 1.45 and 1.47, one can derive the phase rotaion in the reflected fiels as

$$\Delta\phi(s) \equiv \frac{\delta E_{\rm r}(s)}{\bar{E}_{\rm r}} = \frac{t_1^2 r_r}{(t_1^2 + r_1^2)r_2 - r_1}\frac{\Delta\phi(s)}{1 - r_1 r_2 e^{-2sT}}. \tag{1.48}$$

This equation shows that the induced phase shift $\Delta\phi$ is amplified by the frequency dependent factor when it is observed at the reflected field.

Response of the Fabry-Perot Michelson Interferometer

Usually, the arm lengths of the short Michelson interferometer is much shorter than the baseline of the arm FP cavity. Thus, it is reasonable to neglect the contribution from the Michelson interferometer. In this case, the Michelson interferometer works as a device which subtracts the optical phase difference between the x and y arms.

When a plus-mode GW passes along the z-axis through the FP Michelson interferometer placed in the x-y plane, the phase shift due to GW in the x arm has a different sign compared to that of y arm. Therefore, the output field from the Michelson has a phase shift of $2\Delta\phi_r$ if both arms have the same length. As a result, the frequency response of the FP Michelson interferometer is expressed as

$$H_{\rm FPMI} \equiv \frac{2\Delta\phi_r(\omega_{\rm g})}{h(\omega_{\rm g})}, \tag{1.49}$$

$$= \frac{t_1^2 r_2}{(t_1^2 + r_1^2)r_2 - r_1}\frac{H_{\rm MI}(\omega_{\rm g}, L)}{1 - r_1 r_2 \exp(-2i\omega_{\rm g}L/c)}. \tag{1.50}$$

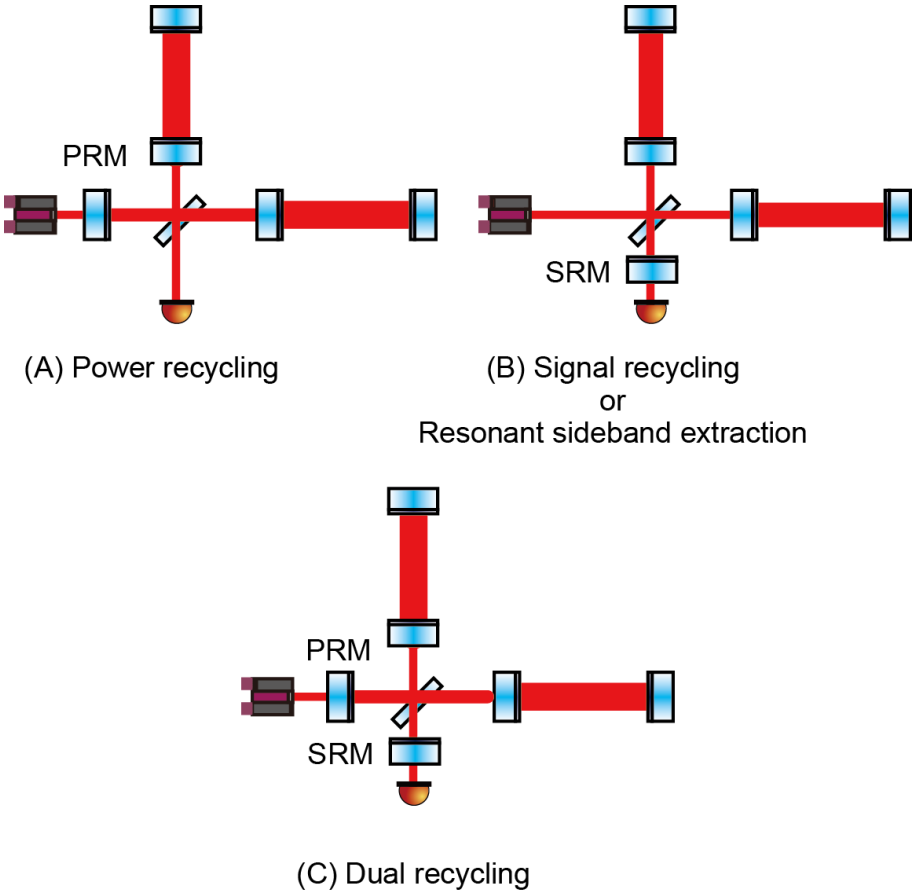

Figure 1.7: Schematic of GWD's configurations. (A) Power recycling configuration. (B) Signal recycling or resonant sideband extraction configuration. (C) Dual-recycling configuration.

Here we used the fact that $\Delta\phi = H_{\rm MI}h/2$. Thus, the addition of the FP arm cavities changes the frequency response and improve the sensitivity as shown in Fig. 1.4.

1.3.3 Further Improvement

In addition to the FP arm cavities, current GWDs employ the scheme called the dual-recycling. This scheme improves the sensitivity and optimizes the observational frequency band by adding two more mirrors to the FPMI. The FPMI enhanced by the dual-recycling system is referred to as dual-recycled Fabry-Perot Michelson interferometer (DRFPMI). The configuration is shown

in Fig. 1.7.

The dual-recycling is a conjunction of two independent techniques — power recycling and signal recycling techniques. The signal recycling technique can be further divided into two modes — the signal recycling and resonant sideband extraction modes.

Power Recycling Technique

The power recycling technique uses an additional mirror, called power recycling mirror (PRM), at the input side of the Michelson interferometer as shown in Fig. 1.7. By employing the additional mirror, one can reflect the light back to the interferometer again. Thus, one can increase the laser power stored inside the arm cavities to reduce shot noise.

Signal Recycling Technique

The signal recycling technique utilizes an additional mirror, called signal recycling mirror (SRM), at the output side of the Michelson interferometer as shown in Fig. 1.7. This scheme enables us to recycle GW signals and propagate them back to the interferometer [10]. The SRM couples with the differential motion of two FP arm cavities to increase the effective finesse for GW signals. Therefore, the storage time increases, resulting in a higher sensitivity at low frequencies. However, it leads to a narrower observational bandwidth.

Resonant Sideband Extraction

The resonant sideband extraction is the scheme which employs the same optical configuration as that for the signal recycling. In this scheme, the effective finesse is reduced in order to expand the observational bandwidth at the expense of the sensitivity at low frequencies.

The signal recycling and the resonant sideband extraction can be switched to each other by changing the interference condition without modifying the optical configuration.

Dual-Recycling

The power recycling, and the signal recycling (or resonant sideband extraction) schemes can be independently employed together. This configuration is called the dual-recycling configuration. The dual-recycling configuration is shown in Fig. 1.7.

1.3.4 Noise Sources

The sensitivity of GWDs is determined by the summation of lots of noise sources. Here we introduce several noises which limit the sensitivity.

Quantum Noise

Quantum noise is a fundamental noise which limits the sensitivity at broad band frequency. At the lower frequency band, radiation pressure noise is one of the dominant noise sources. The radiation pressure noise fluctuates the momentum of the suspended mirrors and is proportional to $\sqrt{P}$. Therefore, the smaller beam power and heavier test mass mirror can reduce the radiation pressure noise. The shot noise, which limits the sensitivity at higher frequency, can be reduced by increasing the laser power because it is in proportional to $1/\sqrt{P}$. Therefore, these two quantum noise are in trade-off relationship and one needs to choose appropriate laser power to optimize the sensitivity.

Employing a filter cavity is a promising approach to reduce the quantum noise. This technique reduces both radiation pressure and shot noise without changing the parameters such as laser power. In order to realize this technology in GWDs, several studies are ongoing [11, 12]

Seismic Noise

Seismic noise is one of the biggest and inevitable noise sources which dominants at the lower frequency band. It introduces displacement to the position of the mirrors and results in variation in the optical lengths. Besides, the misalignment in the cavity axis can be induced by the seismic noise. Such a misalignment can deteriorate detector sensitivity and stability by increasing a few noise couplings including those to length fluctuation and beam jitter. Moreover, angular misalignment causes light in the fundamental mode to be coupled into higher-order spatial modes, reducing the amount of power stored in the main part of gravitational wave detector. This directly decreases the detector sensitivity. Although the mirrors are suspended as pendulums to reduce the seismic noise, there still remains non-negligible amount of vibration which hinders one to keep resonant condition. Therefore, a feedback control is indispensable to reduce the amount of vibration.

Laser Noises

A free running laser shows fluctuation in both the amplitude and frequency of its field. As any photon detection measurements involves an intensity measurement of the laser, the amplitude noise can couple with the resultant photo

current in various ways. Therefore, the amplitude noise can introduce errors via photon detection. The frequency noise directly couples with the interferometric condition of the detector, resulting in an issue of the length sensing control. Thus, the frequency noise must be suppressed.

Thermal Noise

The mirrors and their suspensions are thermally fluctuated because they have a finite temperature. These thermal fluctuations induce variations in the optical path lengths of the interferometer, called thermal noise. When the suspension is at a finite temperature, it excites the mechanical mode of suspension, resulting in the displacement of the suspended mirror [13]. The thermal noise caused by the suspension wires is called suspension thermal noise. The mirror itself also exhibits the thermally induced fluctuation. They are categorized into two kinds: Browninan noise and thermo-optic noise [14]. Cryogenic operation of a GWD is a promising approach to reduce the thermal noise, resulting in the improved sensitivity. In order to achieve higher sensitivity, several GWDs are operated or planned to be operated with cryogenically cooled test masses.

1.4 Summary of this Chapter

- Gravitational-wave is predicted on the basis of the general theory of relativity.
- The first direct detection of GW by aLIGO opened a new window to the Universe, called gravitational-wave astronomy. A number of GW events are detected by terrestrial gravitational-wave detectors.
- The current gravitational-wave detectors are based on the Michelson interferometer enhanced by the additional mirrors for recycling technique.
- The sensitivity of laser interferometric gravitational-wave detector is determined by the various noises. Reduction of these noises are indispensable to improve the sensitivity of the detector.

Chapter 2

Cryogenic Gravitational-wave Detectors

A laser interferometric GWD achieved first detection of GW and opened a new window to the Universe. A GWD with improved sensitivity enables wider range of detection of GW sources and enrich the GW astronomy. Thermal noise induced by coatings deposited on the test mass surface is a dominant noise source around 100 Hz where the current GWDs have the highest sensitivity. As the thermal noise is proportional to the temperature of the system, the use of cryogenically cooled test masses and suspensions is a promising way to reduce the thermal noise. Therefore, cryogenic operation of GWDs efficiently improves the sensitivity and enables to achieve further discoveries in the Universe.

This chapter is dedicated to introduce the cryogenic GWDs which is constructed or planned to be constructed. First, we introduce CLIO as a prototype for KAGRA. Second, we explain KAGRA which employs cryogenically cooled sapphire test masses. Then, we introduce the future cryogenic GWDs, the Einstein Telescope and LIGO Voyager. After that, the technologies which are being developed to realize the future GWDs are described. Finally, the issue which originated from the cryogenic system in KAGRA is described.

2.1 CLIO

CLIO (Cryogenic Laser Interferometer Observatory) is a prototype interferometric GWD toward KAGRA [15]. CLIO was constructed underground in Kamioka mine, which can reduce the seismic noise. CLIO has two 100 m length arm, and a Fabry-Perot cavity is embedded in each arm. One of the notable features of CLIO is the employment of cryogenically cooled sapphire

test masses, aiming at the demonstration of thermal noise reduction. In order to achieve the cryogenic operation of CLIO, a number of studies were conducted such as measurement of cryogenic contamination [16], and development of a low-vibration cryocooler [17]. Through these works, CLIO achieved a cryogenic operation, and demonstrated the thermal noise reduction in a GWD [18]. Thus, CLIO paved a path to large-scale cryogenic interferometric GWDs.

2.2 KAGRA

KAGRA, a gravitational-wave detector constructed in Japan, is operated with cryogenically cooled sapphire mirrors, aiming to reduce the thermal noises and to improve the sensitivity [19, 20]. In this section, we briefly describe the characteristics of KAGRA. More details can be found in Refs [21, 22]. The parameters are listed in Tab. 2.2.

2.2.1 Configuration

KAGRA employs DRFPMI configuration with 3 km arm cavities as shown in Fig. 2.1. The optical configuration of KAGRA can be divided into five systems — the input optics, FPMI, power recycling optics, signal recycling optics and output optics.

The input optics consist of three parts. An input mode cleaner (IMC), which is a triangular cavity in the form of isosceles triangle with the length of one side much shorter than the other two, is employed in the input optics. The IMC provides three critical functionalities — spatial mode cleaning, polarization selection and frequency stabilization [23, 24] The input mode matching telescopes (IMMTs) are used to adjust the spatial mode of input beam. The FPMI part consists of the BS, which splits the beam into two, and two FP cavities embedded in each 3 km length arm. The test mass mirrors which compose arm cavities are sapphire mirrors with temperature of 22 K. The power recycling and signal recycling systems are adopted to improve the sensitivity by reducing the quantum noise. The output optics remove the unwanted output beam such as higher-order modes which are generated by misalignments, impurities of mirrors, and so on.

KAGRA is also constructed underground to reduce the seismic noise which limits the sensitivity at lower frequency range as shown in Fig. 2.7. These two features, the cryogenically cooled mirrors and underground location, are unique for KAGRA which are not found in current other GWDs.

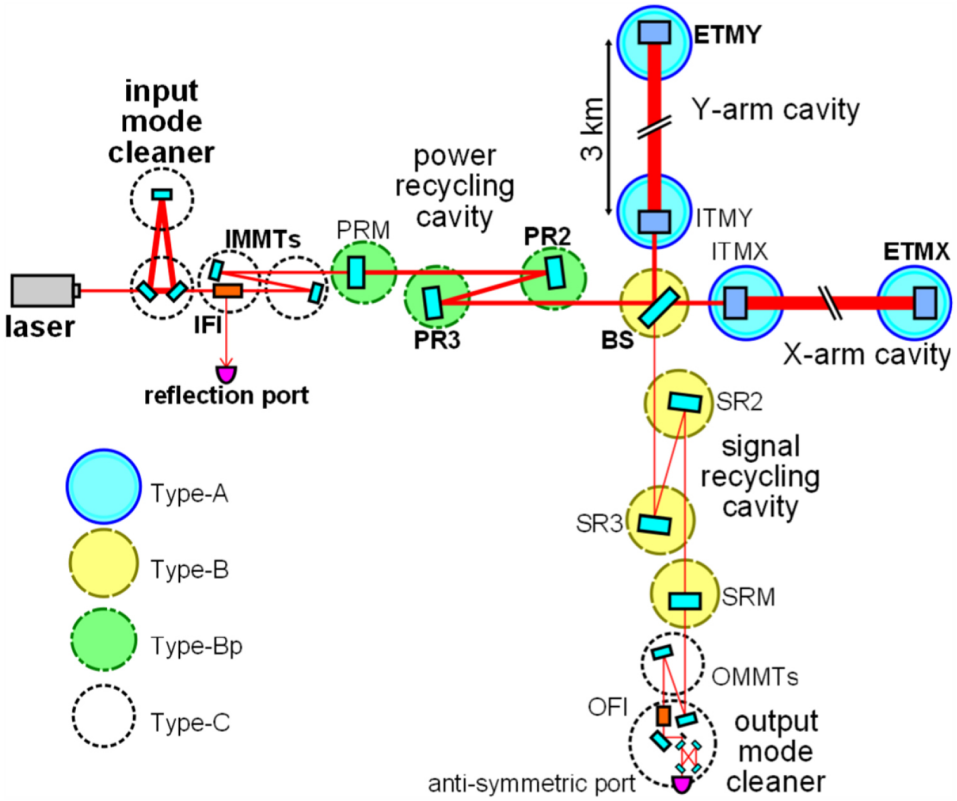

Figure 2.1: Configuration of KAGRA [21]. Each arm has 3-km length which is composed of the sapphire mirrors. Several types of suspensions are installed in KAGRA. Test masses which compose arm cavities are suspended by Type-A suspension in order to reduce the impacts of seismic motion. The types of suspensions are shown in Fig. 2.2.

2.2.2 Vibration Isolation System

Seismic motion is an inevitable noise source for ground-based precision measurements. The vibration isolation system which reduces the seismic motion of the mirrors are indispensable for GWDs. Fig. 2.2 shows the vibration isolation systems employed in KAGRA. A km-scale GWD requires large seismic attenuation factor of 10^{-8} - 10^{-10} around 10-100 Hz. In order to achieve such high vibration isolation ratio, 13.5 m height mutlistage pendulum suspension, called Type-A, is used for test mass mirrors. At the bottom of Type-A tower, a cryogenically cooled payload, called cryopayload, is hanged. A cryopayload plays an important role to achieve a cooling and vibration isolation simultaneously.

Other main optics are also suspended for seismic attenuation. Type-B

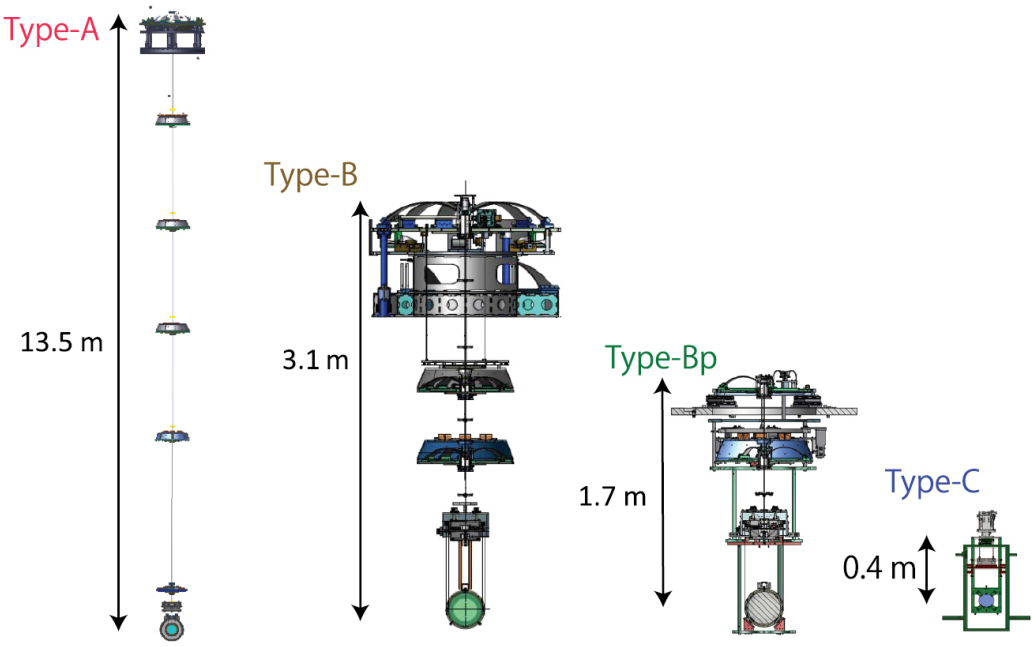

Figure 2.2: The vibration isolation systems used in KAGRA [25]. Type-A suspensions are used for test masses. Type-B is a suspension for signal recycling cavity mirrors and beam splitter. Type-Bp suspension is for power recycling mirrors. Type-C suspensions are employed for other important optics such as input mode cleaner (IMC) or input mode matching telescope (IMMT).

is a suspension for signal recycling mirrors and the beam splitter. Type-B suspension has approximately 3.1 m height. Type-Bp suspension, simplified compared to Type-B suspension, is used for power recycling mirrors. Type-C suspensions are employed for other important optics such as input mode cleaner (IMC) or input mode matching telescope (IMMT). Thanks to these suspensions, displacements induced by the seismic motion are mitigated, and the detector is operated with higher sensitivity.

2.2.3 Cryogenic Systems of KAGRA

The use of cryogenically cooled sapphire test mass mirrors is one of the notable features of KAGRA. Its diameter, thickness, and weight are 22 cm, 15 cm, and 23 kg, respectively. On the sapphire mirror surface, dielectric multilayer coatings are deposited in order to reflect or anti-reflect the laser beam. The multilayer coatings are composed of SiO_2 and Ta_2O_5 stacked alternately in

Table 2.1: Cooling methods and temperature of GWDs.

Name	Temperature	Cooling method
KAGRA	22 K	conduction
LIGO Voyager	123 K	radiation
The Einstein Telescope	10 K	conduction

order to achieve high reflection to the laser beam.

The sapphire test masses are suspended by sapphire fibers which have large thermal conductivity at cryogenic temperature. In addition, sapphire fiber has low mechanical loss, resulting in in low thermal noise. On the other hand, the diameter of the fiber is thicker than that of fused silica fiber used in aLIGO to achieve enough heat extraction from sapphire test mass to maintain cryogenic temperature. This leads to larger suspension thermal noise and lower resonant frequencies of fibers which is called violin modes as shown in Fig. 2.7.

Tab. 2.1 describes the cooling methods of various GWDs. The way of cooling down the mirror depends on its target temperature. As radiative cooling is dominant above ~ 100 K, LIGO Voyager plans to employ radiative cooling. On the other hand, radiative cooling is not dominant below 100 K. Therefore, in order to cool down the mirror below 100 K, one have to employ heat conduction for cooling down the mirror. For the case of KAGRA and the ET, heat links is or will be used which can introduce vibration contamination. Low vibration cryocoolers are used for cooling down the mirrors in order to reduce the amount of vibration which can be transferred to the mirror [17]. Besides, aluminum heat links are employed, aiming effective cooling and mitigate vibration contamination [26]. However, the vibration induced by heat links can still degrade the sensitivity, and the heat link vibration isolation systems (HLVISs) are installed to reduce the vibration noise in KAGRA.

Fig. 2.3 shows the cryogenic part of KAGRA. The sapphire mirror is suspended by cryopayload to reduce the seismic noise. Heat links are connected to the cryopayload though the HLVISs for conductive cooling. Fig. 2.4 shows how the test mass is cooled by conductive cooling.

The cryopayload is hanged by 13.5 m length suspension, called Type-A suspension. Cryogenically cooled duct shields are installed to reduce the radiation from room temperature environment. The length of duct shield is approximately 5350 mm, and its diameter is 370 mm as shown in Fig. 2.5. Baffles are installed inside the duct shield in order to mitigate the impacts of scattered light which can appear in output signal of GWD by recombining to

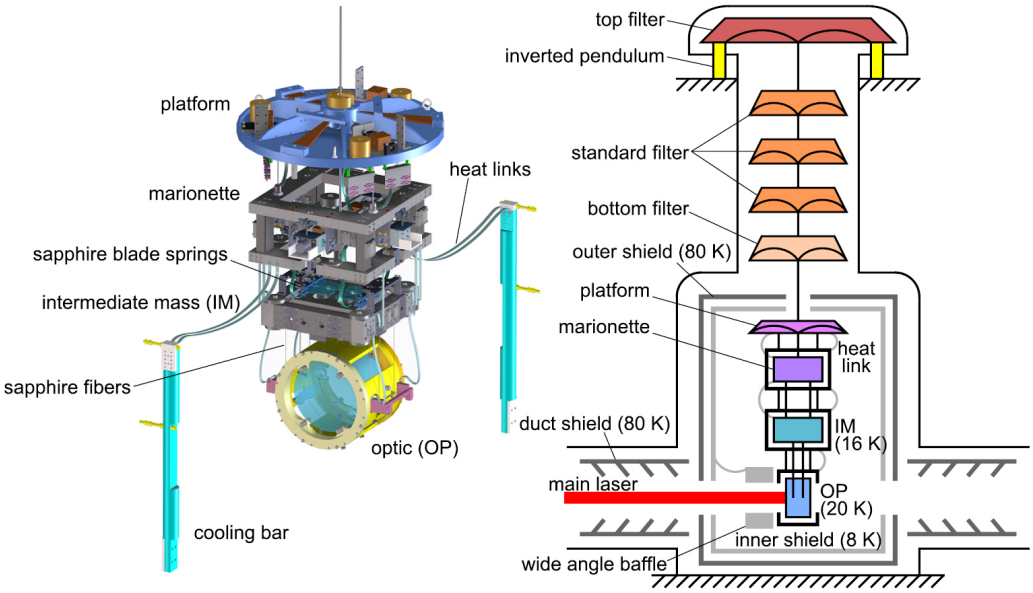

Figure 2.3: Schematic wiwe of the cryogenic payload (Left) and tower for test mass (right) in KAGRA [21]. The sapphire mirror is suspended by cryopayload. Heat links are connected to the cryopayload for conductive cooling. The beam from the arm cavity comes though the duct shield which reduces the radiation from room temperature environment.

the main beam. This shield also reduces the thermal input by radiation from the room temperature environment to 0.1 W. The extractable heat is designed as 0.72 W. This value is considered enough for maintain the temperature of sapphire mirror at 22 K. Thanks to the cryogenic system, KAGRA can operate with cryogenically cooled sapphire mirrors.

Fig. 2.6 shows the cooling curve of sapphire test mass. In order to reach the cryogenically cooled sapphire test mass, it takes about one month. Therefore, the time which can be spent for commissioning before an observing run becomes shorter than other room temperature GWDs due to the cooling period. Studies for shortening the cooling time are important for cryogenic GWDs.

2.2.4 Sensitivity of KAGRA

The designed sensitivity of KAGRA is shown in Fig. 2.7. Quantum noise dominates broad band frequency range — radiation pressure noise and shot noise limit the sensitivity at lower and higher frequency range, respectively. Thermal noise induced by sapphire mirrors is still one of the dominant noise

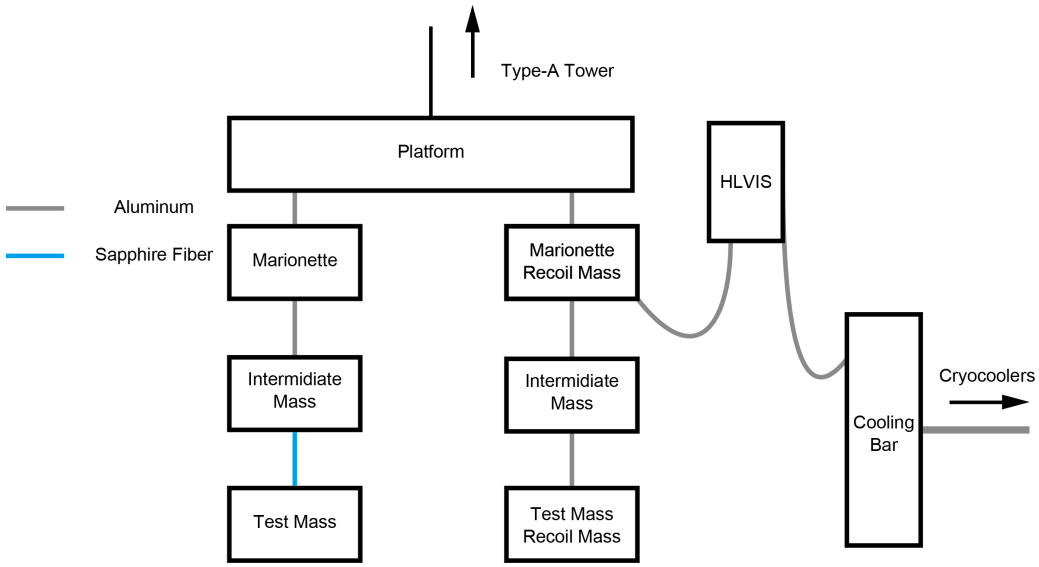

Figure 2.4: Schematic of the thermal connection of cryogenic payload in KAGRA. The sapphire test mass is suspended by sapphire fibers which extract heat, and other stages are connected by aluminum heat links.

sources around 100 Hz where KAGRA hase the highest sensitivity. Especially, thermal noise from coatings on the sapphire mirrors are dominant noise source. Not only quantum noise, but also thermal noise, especially coating thermal noise, are needed to be reduced for further improvement in the sensitivity. One can see several peaks in suspension thermal noise. Two peaks at lower frequency is due to the resonance of the suspension. The peak around 180 Hz is so-called violin mode which originates from the sapphire fibers hanging test mass mirrors.

Historically, the binary neutron star inspiral range has been commonly used as an index of the sensitivity of GWD. The binary neutronstar inspiral range is the merit of the GWD which denotes the detectable range of $1.4\,\mathrm{M}_\odot$ binary neutronstar merger with S/N = 8. The binary neutron star inspiral range can be calculated as [28]

$$\mathscr{R} = \frac{0.442}{\rho_{\mathrm{th}}} \left(\frac{5}{6}\right)^{1/2} \frac{c}{\pi^{2/3}} \left(\frac{G\mathcal{M}_{\mathrm{c}}}{c^3}\right)^{5/6} \left[\int_{f_{\mathrm{min}}}^{f_{\mathrm{max}}} \frac{f^{-7/3}}{S_{\mathrm{n}}(f)} \mathrm{d}f\right]^{1/2}, \tag{2.1}$$

where $\rho_{\mathrm{th}} = 8$ is the threshold, G the gravitational constant, and $\mathcal{M}_{\mathrm{c}}$ the chirp mass of the binary system. The factor 0.442 is the sky average constant [29]. The lower frequency limit f_{min} is set to be $f_{\mathrm{min}} = 10$. The upper end frequency is set to be the gravitational-wave frequency at the ISCO of the Schwarzshild

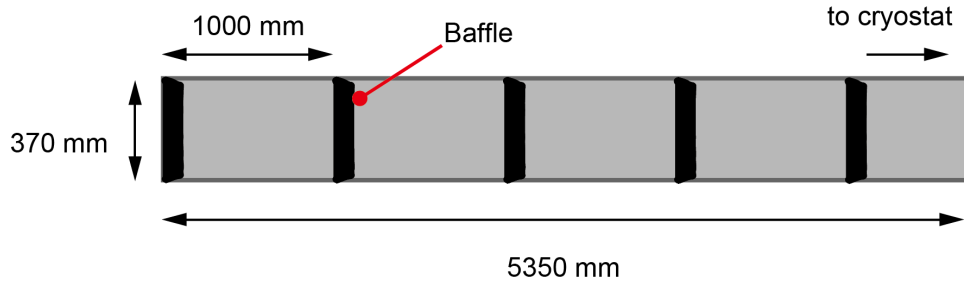

Figure 2.5: Schematic picture of cross section of the duct shield in KAGRA. The length of duct shield is 5350 mm and the diameter is 370 mm. The baffles are installed inside the duct at 1 m intervals to reduce the scattering noise.

metric which is described as

$$f_{\max} = \frac{c^3}{6^{3/2}\pi G M_{\rm tot}}, \tag{2.2}$$

where $M_{\rm tot} = m_1 + m_2$ is the total mass. The designed binary neutron star range of KAGRA is 153 Mpc with Detuned Resonant Sideband Extraction (DRSE) configuration.

2.3 Future Gravitational-wave Detectors

2.3.1 The Einstein Telescope

The Einstein Telescope (ET) is planned to be constructed in Europe with 10 km arm length xylophone. The ET will be constructed underground and consists of two part, the ET-LF and the ET-HF. The ET-HF will adopt room temperature test masses which explores high frequency GWs. On the other hand, the ET-LF, which is specialized for low frequency GWs, will employ cryogenically cooled test masses at 10 K with 1550 nm wavelength laser. In order to achieve 10 K test mass mirrors, conductive cooling systems are planed to be installed in the ET. As conductive cooling can induce vibration contamination via heat links, vibration isolation systems for heat links also will be employed [30]. In order to realize 10 K cryogenically cooled mirrors, a number of studies are on-going [31, 32].

As shown in Fig. 2.8, the ET-LF has remarkable sensitive below 10 Hz where one cannot access with current GWDs. The design sensitivity is approximately

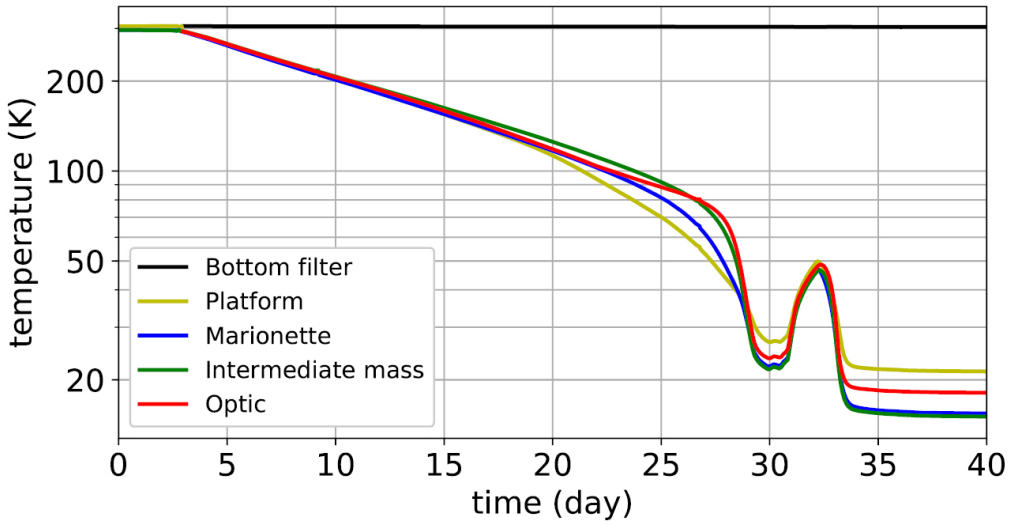

Figure 2.6: The cooling time of KAGRA test mass [21]. Due to the restart of cryocoolers, one can see the bump around day 30. It takes about one month to obtain cryogenically cooled sapphire test mass.

100 times better at 10 Hz than current GWDs such as KAGRA. Therefore, the realization of the ET should provide further discoveries which cannot been done by current GWDs. One example is a detection of GW from intermediate mass black holes with masses on the order of $10^2 - 10^3 M_\odot$. The existence of such intermediate mass black hole has been proved by direct detection [33]. In order to constrain formation scenarios such massive black holes, multiple detections are necessary [34]. ET-LF, which employs cryogenically cooled mirror, is suited for detections of massive black holes and should provide further insights into the Universe.

2.3.2 LIGO Voyager

LIGO Voyager is a substantial upgrade of aLIGO, and will employ cryogenically cooled mirrors with DRFPMI configuration [35]. The LIGO Voyager test mass temperature is planed to be 123 K where silicon has a zero cross of its thermal expansion coefficient [36]. Therefore, the substrate thermal noise can be minimized.

The cryogenic system in LIGO Voyager employs radiative cooling to maintain the test mass temperature at 123 K. This approach can avoid the complicating the suspensions with vibration contamination via conductive heat

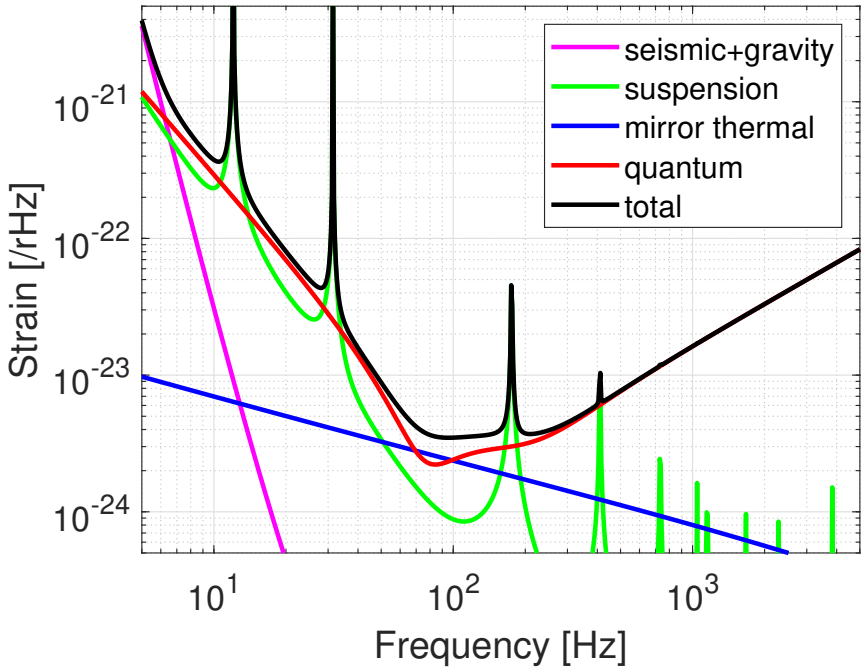

Figure 2.7: The design sensitivity and noise sources of KAGRA [27]. Black solid line represents the sensitivity of KAGRA. Other curves denote the noises which contribute to the sensitivity. The first order of violin mode can be seen around 180 Hz, and its higher-order also can be seen at higher frequency range. At most sensitive frequency range around 100 Hz, the mirror thermal noise, especially coating thermal noise, is still dominant though the cryogenically cooled mirrors are employed.

paths. In order to achieve 123 K temperature, cryogenic shields with about 10 m lengths are used which isolate the radiation from the room temperature environment.

LIGO Voyager requires approximately 150 W laser power at the input to the interferometer. As the arm cavity power in LIGO Voyager is designed as 3 MW, the absorption in the coatings is one of the problems which can prevent cryogenic operation. Choosing a longer wavelength, around 2000 nm, can mitigate the absorption in the coatings and realize the designed arm cavity power. However, the improvements in substrate material, coatings, and cryogenic systems are still needed to realize LIGO Voyager.

Fig. 2.9 shows the sensitivity and noise sources of LIGO Voyager. The inspiral range of LIGO Voyager for $1.4M_{\odot}$ neutronstar binary system is about

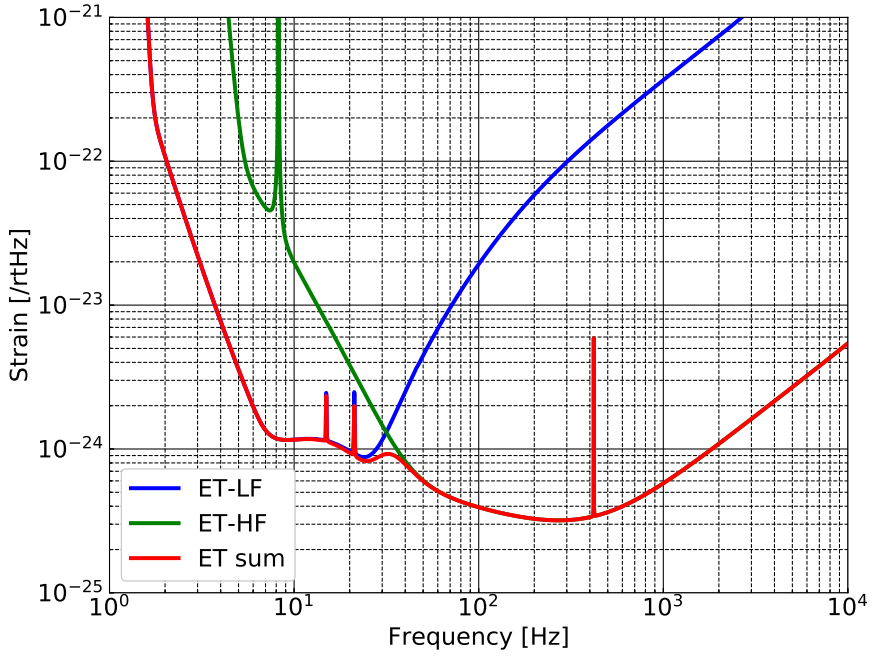

Figure 2.8: The design sensitivity of the Einstein Telescope [30]. The ET consists of two parts — specialized for low frequency or high frequency GWs. The blue and green solid line shows the sensitivity of the ET-LF and ET-HF, respectively. The red line represents the total sensitivity of the ET which is the summation of the ET-LF and ET-HF.

740 Mpc. This is about 4 times larger inspiral range, resulting $4^3 = 64$ times larger number of detection than aLIGO. Moreover, LIGO Voyager has a good sensitivity such that it can detect $30 - 30M_\odot$ binary black hole mergers even at $z \sim 10$ [35]. Therefore, the realization of LIGO Voyager will enrich the gravitational-wave astronomy.

2.4 Technologies for Future Gravitational-wave Detectors

In order to realize the future GWDs with improved sensitivity, a number of studies are being conducted intensively. In this section, we briefly introduce several technologies to be developed for future GWDs.

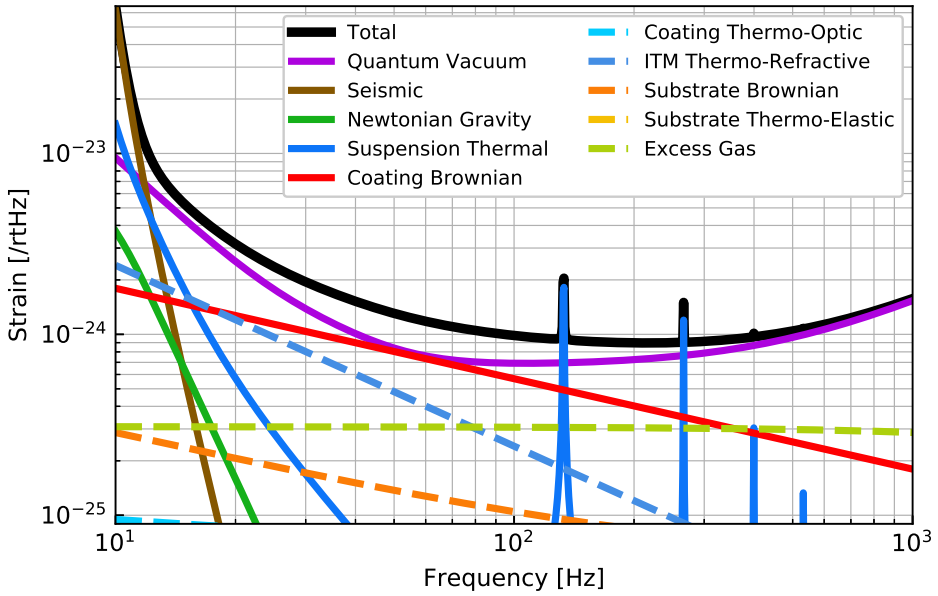

Figure 2.9: The design sensitivity and noise sources of LIGO Voyager [35]. Black solid line represents the sensitivity of LIGO Voyager. Other curves denote the noises which contribute to the sensitivity.

2.4.1 Filter Cavity

Quantum noise which limits the sensitivity at broad band frequency range is one of the important noise sources in GWDs. This noise originates from the quantum nature of light. The use of frequency-dependent squeezing technique is a possible solution to reduce the quantum noise in the broad band frequency. Filter cavity experiment in TAMA 300 interferometer demonstrated frequency-dependent squeezed vacuum which can reduce the quantum noise [11]. In future, the employment of filter cavity in GWDs will enable improvement in an overall sensitivity.

2.4.2 Substrate Material

The choice of a substrate material for a test mass mirror is one of the most important parts to construct a GWD. There has been a number of studies to achieve the high-end, low-loss mirror for GWDs [37, 38, 39]. There are some candidates as test mass mirror substrates for future GWDs — fused

silica, sapphire, and silicon. Fused silica, the material used in the current room temperature GWDs, has a large mechanical loss at cryogenic temperature which leads to large thermal noise and is not suitable for a cryogenic GWD [40].

Silicon is one of the most likely candidates for a cryogenically operated GWD. Silicon has a small mechanical loss and consequently low Brownian noise under cryogenic temperature [41]. In addition, silicon has the unique advantage that its substrate thermo-elastic noise vanishes at 18 K and 123 K where its coefficient of thermal expansion crosses zero [36]. However, as silicon is opaque for wavelengths shorter than 1100 nm and has small absorption only for wavelengths longer than 1400 nm, the wavelength of main laser should be within the range of 1400 nm to 2100 nm [42]. Therefore, the wavelength of main laser is chosen to be 1550 nm and 2000 nm for ET and LIGO Voyager, respectively [30, 35].

The size of test mass is important for radiation pressure noise and coating thermal noise. Heavier and larger diameter test masses are necessary to reduce the radiation pressure noise and coating thermal noise, respectively. Current magnetically stabilized Czochralski (MCZ) technique realized 45 cm diameter silicon crystal with high purity. Therefore, 200 kg silicon test mass without serious impurities is achievable in the future GWDs.

Sapphire, which is used in KAGRA, is also one of the candidates. However, the available size of high-quality sapphire mirror is not so large and a breakthrough in technology is indispensable to fabricate larger size of sapphire mirror. In addition, sapphire is a birefringent crystal, and has a potential to induce polarization conversion from S-pol. to P-pol., which can make harder to operate the interferometer stably. There are rooms to be improved to achieve higher sensitivity of GWDs with sapphire mirrors.

2.4.3 Coatings

Thermal noise arises from the coatings on the test mass becomes one of the noise sources which can limit the sensitivity. For the case of the ET, coatings which have 25 times smaller thermal noise than that of current ones with about 1 ppm absorption are required. Current typical $SiO_2/Ti : Ta_2O_5$ coating have large mechanical loss around 20 K, which leads to large thermal noise. Therefore, in order to achieve future cryogenic GWDs, the development of coating materials and methods such that thermal noise satisfies the requirement are indispensable.

Low Noise Coating

One of the most promised way to reduce the coating thermal noise (CTN) is to employ low noise coatings. New materials or methods have been studied in order to reduce the CTN [32, 43]. One notable method is to use crystalline coatings which have shown large reduction in Brownian thermal noise [44]. These coatings are deposited GaAs and AlGaAs multilayers on GaAs substrate and can be transferred onto other substrate material. With these coatings, notable optical properties have been demonstrated [44, 45]. However, the size of these coatings is limited by the GaAs substrates currently available. In addition, it requires further tests to evaluate the effect of coating-substrate bonding on any possible thermal noise. An alternative technique to utilize crystalline coatings is to grow a lattice-mathced coating directly onto a substrate. This method removes the need for a complex transfer process. In the case of silica substrate, a possible multilayer crystalline coatings is GaP/AlGaP [46]. Especially, GaP/AlGaP coatings have shown remarkable low mechanical loss at cryogenic temperature. Nevertheless, the GaP/AlGaP coatings need more studies as a mirror coating and further development, particularly of the optical properties.

Amorphous silicon is an interesting material which has large refractive index and shows low mechanical loss at cryogenic temperature [31]. Amorphous silicon, however, has large optical absorption and needs to be tackled with this problem [47]. One possible solution is to adopt multi-material coatings which can achieve the requirement on absorption while amorphous silicon is deposited on near surface of the substrate [31]. By using amorphous silicon with appropriate composition, one can significantly reduce the coating thermal noise combining with cryogenic test masses.

Post Deposition Treatment

One possible approach to reduce the CTN is a post deposition heat treatment i.e., annealing of coatings. Annealing at appropriate temperature improves the optical properties of coatings such as absorption and mechanical loss [48]. Therefore, the annealing has an important role to achieve state-of-the-art mirrors.

However, annealing causes the crystallization of amorphous coatings above a certain temperature and the crystallization temperature varies with coating materials. For the case of typical SiO_2/Ta_2O_5 coatings, tantala layers start to crystallize around 600 °C while the silica layers can be baked up to 950 °C. One possible solution to increase the annealing temperature is to employ some optimal alloy of the materials such as TiO_2 or ZrO_2 [49]. Doping tantala with tita-

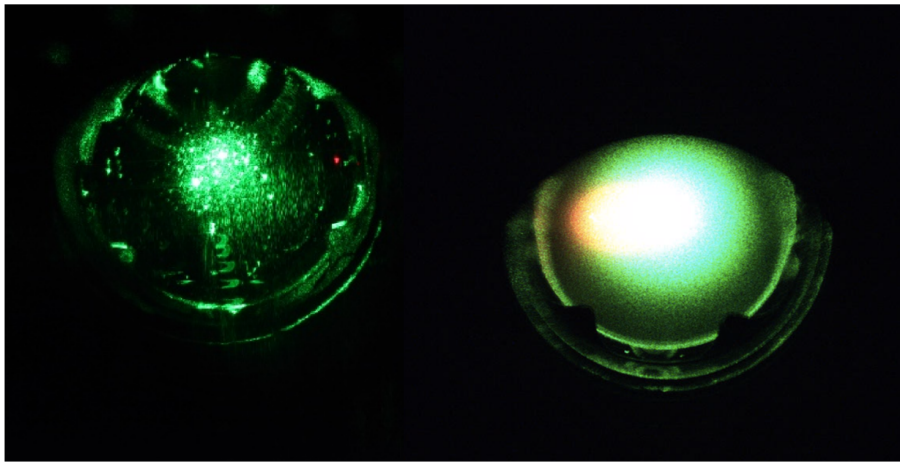

Figure 2.10: Left picture shows the sapphire mirror at room temperature [54]. Right picture shows the frosted sapphire mirror at cryogenic temperature [55].

nia is employed in aLIGO test mass so as to reduce the coating thermal noise. Optimally doped coating shows not only lower mechanical loss but also higher crystallization temperature and can lead to smaller thermal noise. Another is to use very thin nano-layers in which small thickness of the layer suppresses crystallization of coating materials [50]. In addition, nano-layer thickness thin film can reduce the mechanical loss at cryogenic temperature [51].

Coating-Free Mirrors

High reflective mirrors without deposited thin films can be a solution to reduce the coating thermal noise due to the lack of large mechanical loss thin films. Recent studies have reported some amount of achievement in developing high-finesse cavities [52, 53]. However, coating-free mirrors still require significant development in order to be employed in the precision measurements.

2.5 Technical Problem — Molecular Layer Formation

In this section, we describe a technical problem, which can happen in future cryogenic GWDs. One of the critical problems for cryogenic GWDs is the formation of molecular layer on cryogenic mirror surfaces. The molecular layer

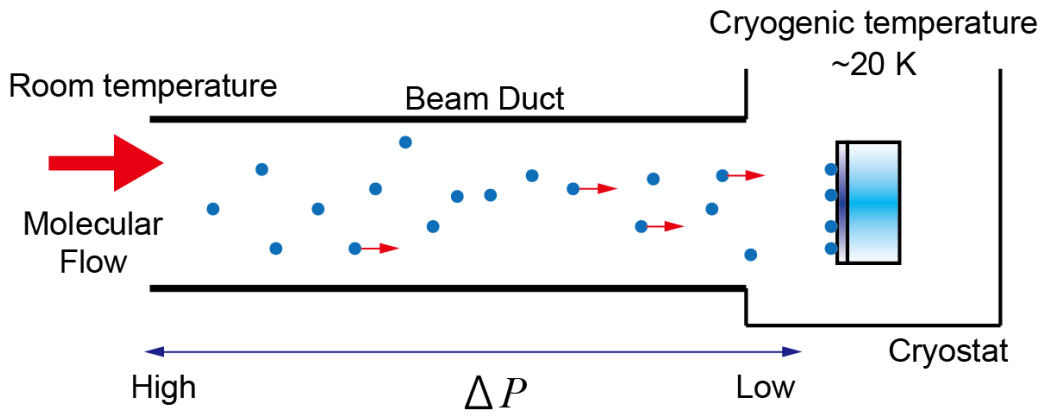

Figure 2.11: Schematic of how molecular layer formed on the cryogenic mirror surface by a molecular flow from beam duct. As the pressure inside the cryostat is quite low compared to that of beam duct because of the cryopumping. The residual gas molecules attached on the room temperature beam duct can easily desorbed, and transported to the cryostat. A part of transported gas molecules hits and be trapped on the test mass surface.

formation is induced by the so-called cryopumping effect, which is usually employed in a vacuum pump [56]. When the vacuum level inside the cryostat is insufficient, the residual molecules are adsorbed by the cryogenic mirror, resulting the frosting of the mirror. KAGRA experienced such phenomenon when the mirrors were cooled down to cryogenic temperature, i.e., $\sim 20\,\mathrm{K}$ as shown in Fig. 2.10 [55].

The molecular layer can be formed though the vacuum level inside the cryostat is enough high to avoid the adsorption of the residual molecules inside the chamber. As the cryostat works as a type of vacuum pump, the pressure inside the cryostat is smaller than that of the room-temperature beam duct. This pressure difference leads to continuous molecular transportation onto the cryogenic mirror surface from the room-temperature beam duct where water molecules can easily detached from the surface. When gas molecules hit a cryogenic mirror surface, they lose their kinetic energy and adhere onto the surface due to the cryopumping. Therefore, the collisions of gas molecules create a molecular layer which grows over time on top of the cryogenic mirror surface. We call such a molecular layer a cryogenic molecular layer (CML) in this thesis. Fig. 2.11 shows the schematic picture of how a molecular layer is formed on the cryogenic test mass.

Formation of the CML prevents the observation of cryogenic GWDs with their best performance due to its optical loss. The possible impacts of the CML

on the optical loss are calculated in the next chapter. The optical loss induced by the CML also degrades the quantum noise. The CML also can contribute to the thermal noise which can limit the sensitivity [57]. In order to remove the CML, one have to warm up the mirror, resulting in less observation time. As shown in Fig. 2.6, recooling of the test mass mirror in KAGRA requires about one month, and the observation will be suspended during this period. Hence, the CML formation is a critical problem in cryogenic GWDs as it decreases the number of detection and observation time.

2.5.1 Previous Studies

In order to achieve cryogenic operation of KAGRA, several studies were performed to investigate the impacts of CMLs. In 2001, the optical loss of CML was measured by a table top experiment [16]. In this table top experiment, the finesse degradation induced by a cryogenic contamination was monitored for about 50 days with 10 K cryogenic Fabry-Perot cavity. It revealed that the power recycling gain (PRG) of KAGRA, which is an important factor to maintain the performance of KAGRA, can be maintained within tolerable degradation for 130 days.

A further study in KAGRA was performed to estimate the CML formation speed by using a Fabry-Perot cavity [58]. The formation speed was obtained by oscillations in finesse of the cavity induced by the reflectivity change due to the CML formation. The estimated CML formation speed was 27 nm/day with 5×10^{-6} Pa vacuum level. This study also revealed that the inspiral range of KAGRA can decrease by about 30% after one year of operation. In addition, they mentioned that a CML can increase thermal noises through large heat input to test masses.

Both of these previous studies are performed with 1064 nm wavelength laser sources. Future cryogenic GWDs, however, will employ longer wavelength laser such as 1550 nm or 2000 nm [30, 35], and the optical impacts of CMLs at these longer wavelength had not been investigated. Therefore, optical loss study and characterization of CMLs at longer wavelength becomes very important to estimate the impacts on future cryogenic GWDs.

2.6 Target of this Study

A cryogenincally cooled mirror is a key technology to achieve the future GWDs. Such cryogenic mirrors can adsorb the residual gas molecules, and reduce the performance of GWD. Previous studies investigated possible impacts of adsorbed CML on KAGRA which employs 1064 nm laser. However, there is no

study which investigated the optical loss of CMLs for future GWDs, which will employ longer wavelength than 1064 nm, though CMLs can affect the performance even at very thin thickness. The goal of this thesis is to study the impact of the molecular formation on optical loss of future cryogenic GWDs by theoretical calculations, andestablish a method to characterize with a ppm level resolution in optical loss measurement and a nanometer level resolution in thickness determination.

2.7 Summary of this Chapter

- Operation with cryogenically cooled test mass mirrors is a promising approach to enhance the number of GW detection by improving the sensitivity.
- KAGRA operates with 22 K cooled sapphire test masses to reduce thermal noises.
- The future cryogenic GWDs have improved sensitivity and should provide new discoveries.
- However, cryogenically cooled mirrors can suffer from the formation of molecular layers on their surfaces.
- The molecular layer formed on the cryogenic mirror surface affects the GW observation, and can reduce the number of detection.
- Previous studies investigated the impacts of the molecular layer on the optical loss of KAGRA. However, the impacts on the optical loss of future GWDs have not been studied.
- The goal of this thesis is to study the impact of the molecular formation on optical loss of future cryogenic GWDs, and give a novel approach to characterize the optical loss of very thin molecular layer.

Table 2.2: The parameters of KAGRA [21].

Parameters	Symbol	Value
Arm length	L_{arm}	3000 m
Mirror mass	M	22 kg
Beam radius	w_0	3.5 cm
Temperature of the test mass	T	22 K
ITM transmittance	T_{ITM}	0.4%
ETM transmittance	T_{ETM}	7 ppm
PRM transmittance	T_{PRM}	10%
Loss inside the arm cavity	$T_{\mathrm{loss,arm}}$	93 ppm
Laser wavelength	λ	1064 nm
Laser power	P_{in}	67 W
Mirror thickness	d_{mir}	15 cm
Absorption in test mass	α_{mir}	50 ppm/cm
Density of sapphire	ρ_{sap}	3980 kg/m^3
Specific heat of sapphire	C_{sap}	0.69 J/K/kg
Thermal expansion rate of sapphire	α_{sap}	5×10^{-6} 1/K
Thermal conductivity of sapphire	κ_{sap}	1.57×10^4 W/m/K
Young's modulus of sapphire	Y_{sap}	73.2 GPa
Poisson ratio of sapphire	σ_{sap}	0.25
Loss angle of sapphire mirror	ϕ_{sap}	1×10^{-8} rad
Refractive index of sapphire ($\lambda = 1064$ nm)	n_{sap}	1.7545
Diameter of sapphire fiber	d_{f}	1.6 mm
Length of sapphire fiber	l_{f}	350 mm
Loss angle of sapphire fiber	ϕ_{f}	2×10^{-6} rad
Extractable heat	Q	0.72 W

Chapter 3

Theoretical Study of Cryogenic Molecular Layer

The use of cryogenic mirrors is a promising approach to improve the sensitivity of GWDs. The cryogenic mirrors in KAGRA, however, suffered from the CML on the mirror surfaces as shown in Fig. 2.10 [55]. The properties of the mirror, i.e., the reflectance and transmittance, change due to the growth of CML.

The impact of the CML on scattering has been experimentally estimated on a small-scale cryogenic system [16]. Recent study revealed that the CML is formed on the high-reflection (HR) side of the cryogenic mirror in KAGRA, and the formation rate and possible impacts on KAGRA were estimated [58, 59]. Both of these studies are conducted with the laser wavelength of 1064 nm. On the other hand, future GWDs will employ longer wavelength laser. The ET is planning to use 1550 nm wavelength laser for the law-frequency part (ET-LF), and LIGO Voyager will use 2 μm wavelength. At such a longer wavelength region, the water molecules, which is considered as one of the most dominant molecules of the CML, have much larger optical absorption compared to that at 1064 nm. Fig. 3.1 shows the absorption of ice around 1550 nm, and 2000 nm. The amorphous ice, which is considered as the main component of the CML, has large absorption within this range. Hence, the optical loss due to the CML can be more critical for future cryogenic GWDs.

In this chapter, first, we describe one of the possible impacts of the CML on cryogenic GWDs i.e., optical losses. Then, we derive a theoretical model of the optical loss induced by the CML in a cryogenic GWD. Finally, we show how the optical loss of the CML affects a cryogenic interferometric GWD. The contents described in this chapter is published as an article by the author [61].

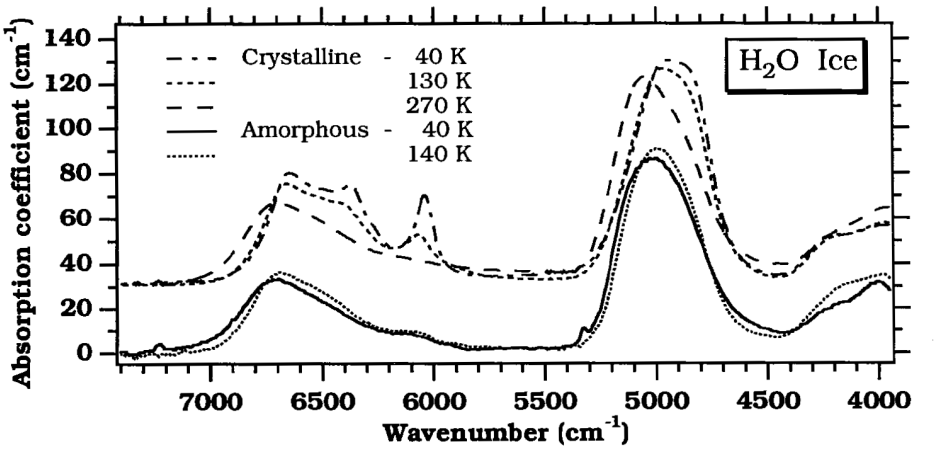

Figure 3.1: Absorption of ice. This figure is cited from the reference [60]. Horizontal axis is the wavenumber, which is the inverse of wavelength, $1/\lambda$.

3.1 Optical Loss

Low optical loss mirrors are vital for precision laser interferometry [38, 62]. As shown in Fig. 3.2, optical loss in the mirror is introduced mainly by two paths — optical scattering and absorption. The test mass mirrors used in GWDs are manufactured with state-of-the-art technologies to meet the requirements on optical losses [63]. A molecular layer, however, generates additional optical loss which can hinder us from operating the detector at a cryogenic temperature and achieving the design sensitivity. Especially, the optical absorption generates an additional heat load to a cryogenic mirror and its temperature can be increased by this effect. In this section, we review the derivation of the optical loss by CML on a test mass mirror. More details can be seen in the reference [59].

3.2 Scattering

A beam reflected by a mirror is scattered by imperfections of the mirror surface which causes an optical loss and decreases the arm cavity power in GWDs. Moreover, the scattered light can become a technical noise source in GWDs by recombining to the main beam [64, 65]. Therefore, the scattering by the CML can reduce the sensitivity of GWDs. In this section, we theoretically derive the amount of optical loss induced by scattering in the CML.

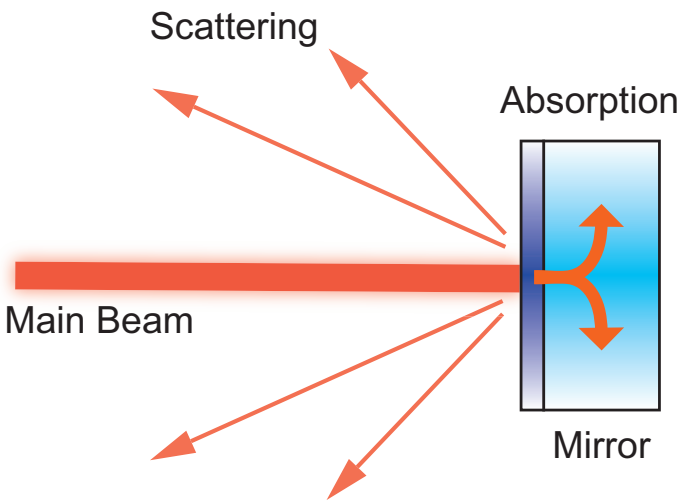

Figure 3.2: Schematic drawing of the optical loss in the test mass mirror. The scattering and absorption lead to less arm cavity power which decreases the sensitivity of GWDs. Furthermore, the optical absorption introduces an additional heat load to a cryogenic mirror.

The ratio between the total reflected beam power and that of scattered light, called total integrated scattering (TIS), is defined as [66]

$$\mathrm{TIS} \sim \frac{P_{\mathrm{sca}}}{P_0 R}, \tag{3.1}$$

where P_0 is the incident beam power, P_{sca} is the power of the scattered light and R is the reflectance of the CML surface. For the case of the angle of incidence equals to zero such as the arm cavities in GWDs, the TIS can be calculated as [67]

$$\mathrm{TIS} = 1 - \exp\left\{-\left(\frac{4\pi\sigma}{\lambda}\right)^2\right\}, \tag{3.2}$$

where

$$\sigma^2 = 2\pi \int_0^{\frac{1}{\lambda}} \mathrm{PSD}(f) f \mathrm{d}f. \tag{3.3}$$

Here λ is the laser wavelength. $\mathrm{PSD}(f)$ [m^4] represents the $2-D$ surface power spectral density and f [1/m] is the spatial frequency.

Assuming uniform molecular adsorption on a cryogenic mirror surface, the incident molecular flux to the unit area follows the Poisson distribution. Therefore, the standard deviation of the number of molecules is given by $\sqrt{\langle N \rangle}$ where

N is the average number of molecules. The relationship between the thickness of CML, t, and N can be expressed as

$$t = N\left(\frac{M}{\rho N_A}\right)^{1/3}, \tag{3.4}$$

where $\rho = 940\,[\mathrm{kg/m^3}]$ represents the density of the CML, $N_A\,[1/\mathrm{mol}]$ is the Avogadro number and $M = 18 \times 10^{-3}\,[\mathrm{kg/mol}]$ is the molecular mass. From Eq. (3.4), the relation between the mean thickness of the CML, $\langle t\rangle$ and its standard deviation, $\sigma_{\langle t\rangle}$, can be written as

$$\sigma_{\langle t\rangle} = \left(\frac{M}{\rho N_A}\right)^{1/3}\sqrt{\langle N\rangle} = \left(\frac{M}{\rho N_\mathrm{A}}\right)^{1/6}\sqrt{\langle t\rangle}. \tag{3.5}$$

PSD which follows this distribution can be calculated as [68]

$$\mathrm{PSD}(f) = \pi\sigma^2_{\langle t\rangle}\xi^2\exp[-(\pi f\xi)^2], \tag{3.6}$$

where ξ is the correlation length which characterizes the periodic length of the roughness along the surface. Thus, the scattered power by the CML can be expressed as

$$P_\mathrm{sca} \sim P_0 R\left[1 - \exp\left\{-\frac{32\pi^4\sigma^2_{\langle t\rangle}\xi^2}{\lambda^2}\int_0^{\frac{1}{\lambda}} e^{-(\pi f\xi)^2} f\,\mathrm{d}f\right\}\right]. \tag{3.7}$$

Assuming the correlation length of the CML, ξ, Eq. 3.7 allows us to estimate the optical loss generated by the scattering.

3.3 Optical Absorption

Another way leading to an optical loss is the optical absorption. Especially, the optical absorption in a cryogenic mirror plays a crucial role in selecting the parameters of GWD because of an additional heat load on the test mass mirror. For the case of a GWD, a Fabry-Pérot cavity is embedded in the arm to improve the sensitivity [20, 69, 35]. Hence, the laser power inside the arm cavity becomes extraordinarily large and the optical absorption introduced by the CML can become a critical heat source in the cryogenic test mass. Absorption in the anti-reflection (AR) surface can be negligible because of much lower laser power on the surface than the HR side.

The laser power density inside a medium $I(z)$ follows the Lambert-Beer law as

$$I(z) = I_\mathrm{s}\exp(-\alpha z), \tag{3.8}$$

where z represents the depth of the medium from its surface, I_s is the laser power density at the surface, $z = 0$, and α is the absorption coefficient. Assuming Gaussian beam with the beam radius of w_0, the profile of the laser power intensity can be written as

$$\begin{aligned} I_r &= I_0 \exp\left(-\frac{2r^2}{w_0^2}\right) \\ &= \frac{2P_0}{\pi w_0^2} \exp\left(-\frac{2r^2}{w_0^2}\right). \end{aligned} \tag{3.9}$$

where $r = \sqrt{x^2 + y^2}$ and P_0 represent the radius of the beam in cross section and the laser power, respectively. Therefore, the intensity in the medium can be expressed as

$$I(r, z) = \frac{2P_0}{\pi w_0^2} \exp\left(-\frac{2r^2}{w_0^2} - \alpha z\right). \tag{3.10}$$

The power absorbed by the volume element $r\mathrm{d}r\mathrm{d}\theta\mathrm{d}z$ of the medium can be computed as

$$\begin{aligned} A(r, z) &= \{I(r, z) - I(r, z + \mathrm{d}z)\}\, r\mathrm{d}r\mathrm{d}\theta \\ &= -\frac{\partial I(r, z)}{\partial z} r\mathrm{d}r\mathrm{d}\theta\mathrm{d}z \\ &= \frac{2P_0}{\pi w_0^2} \alpha \exp\left(-\frac{2r^2}{w_0^2} - \alpha z\right) r\mathrm{d}r\mathrm{d}\theta\mathrm{d}z. \end{aligned} \tag{3.11}$$

Thus, the total laser power absorbed by a CML of thickness d_{CML} becomes

$$\begin{aligned} A_{\mathrm{CML}} &= -\int_0^{\infty} \mathrm{d}r \int_0^{2\pi} \mathrm{d}\theta \int_0^{d_{\mathrm{CML}}} r \frac{\partial I(r, z)}{\partial z} \mathrm{d}z \\ &= P_0 \left\{1 - \exp(-\alpha d_{\mathrm{CML}})\right\}. \end{aligned} \tag{3.12}$$

Assuming the amplitude of the laser intensity inside the medium follows the Lambert-Beer law, the total amount of the absorption by the molecular layer, A_{CML}, with the thickness of d_{CML} is expressed as

$$A_{\mathrm{CML}} = P_{\mathrm{CML}}[1 - \exp(-\alpha_{\mathrm{CML}} d_{\mathrm{CML}})], \tag{3.13}$$

where P_{CML} is the laser power incoming to the molecular layer and $\alpha_{\mathrm{CML}} = 4\pi \mathrm{Im}(N_{\mathrm{CML}})/\lambda$ is the absorption coefficient of the molecular layer where N_{CML} is the complex refractive index of CML.

For the case of the GWDs, the laser power inside the arm cavity becomes extraordinary large. Therefore, the optical absorption introduced by the molecular layer can become a critical heat source in the cryogenic test mass. As

the laser power inside the arm cavity is much larger than that of the power recycling cavity (PRC), the absorption on the AR side of the test mass can be negligible.

A power recycling technique is applied to GWDs in order to reduce the shot noise by enhancing the laser power inside interferometers [70]. The intracavity power is determined by the finesse of the arm cavity and the power recycle gain. The laser power inside the PRC can be written as

$$P_{\mathrm{PRC}} = G(d_{\mathrm{CML}}^{\mathrm{ITM}}, d_{\mathrm{CML}}^{\mathrm{ETM}}) P_{\mathrm{in}}, \tag{3.14}$$

where $G(d_{\mathrm{CML}}^{\mathrm{ITM}}, d_{\mathrm{CML}}^{\mathrm{ETM}})$ is the power recycle gain, $d_{\mathrm{CML}}^{\mathrm{ITM,ETM}}$ the thickness of the molecular layer on the ITM or ETM, and P_{in} the incident laser power into the PRC. The power recycle gain $G(d_{\mathrm{CML}}^{\mathrm{ITM}}, d_{\mathrm{CML}}^{\mathrm{ETM}})$ can be expressed as [58]

$$G(d_{\mathrm{CML}}^{\mathrm{ITM}}, d_{\mathrm{CML}}^{\mathrm{ETM}}) = \left\{ \frac{t_{\mathrm{PRM}}}{1 - \frac{1}{2} r_{\mathrm{prm}} \sum_i r_i (d_{\mathrm{CML},i}^{\mathrm{ITM}}, d_{\mathrm{CML},i}^{\mathrm{ETM}})} \right\}^2 . \tag{3.15}$$

where $r_i(d_{\mathrm{CML},i}^{\mathrm{ITM}}, d_{\mathrm{CML},i}^{\mathrm{ETM}})\,(i = x, y)$ represent the reflectivity of the x or y arm cavity i.e., inline or perpendicular to the incoming beam to the BS, which is given by

$$\begin{aligned} r_i \left(d_{\mathrm{CML},i}^{\mathrm{ITM}}, d_{\mathrm{CML},i}^{\mathrm{ETM}} \right) &= -r_{\mathrm{ITM},i}(d_{\mathrm{CML}}^{\mathrm{ITM}}) \\ &\quad + \frac{t_{\mathrm{ITM}}^2(d_{\mathrm{CML}}^{\mathrm{ITM}}) r_{\mathrm{ETM}}(d_{\mathrm{CML}}^{\mathrm{ETM}}) r_{\mathrm{loss,arm}}}{1 - r_{\mathrm{ITM}}(d_{\mathrm{CML}}^{\mathrm{ITM}}) r_{\mathrm{ETM}}(d_{\mathrm{CML}}^{\mathrm{ETM}}) r_{\mathrm{loss,arm}}}, \end{aligned} \tag{3.16}$$

where $r_{\mathrm{loss,arm}}$ is the loss equivalent reflectivity in the arm cavity. The reflectivity of the mirror with the molecular layer can be calculated by using the characteristic matrix as shown in the reference [58]. Defining the amount of loss inside the arm cavity as $T_{\mathrm{loss,arm}}$, the loss equivalent reflectivity can be expressed as

$$r_{\mathrm{loss,arm}} = \sqrt{1 - T_{\mathrm{loss,arm}}}. \tag{3.17}$$

The laser power inside the arm cavity is enhanced by $2\mathcal{F}_{\mathrm{arm}}(d_{\mathrm{CML}}^{\mathrm{ITM}}, d_{\mathrm{CML}}^{\mathrm{ETM}})/\pi$ where $\mathcal{F}_{\mathrm{arm}}(d_{\mathrm{CML}}^{\mathrm{ITM}}, d_{\mathrm{CML}}^{\mathrm{ETM}})$ is the finesse of the arm cavity which can be written as

$$\begin{aligned} &\mathcal{F}_{\mathrm{arm}}(d_{\mathrm{CML}}^{\mathrm{ITM}}, d_{\mathrm{CML}}^{\mathrm{ETM}}) \\ &\qquad = \frac{\pi \sqrt{r_{\mathrm{ITM}}(d_{\mathrm{CML}}^{\mathrm{ITM}}) r_{\mathrm{ETM}}(d_{\mathrm{CML}}^{\mathrm{ETM}}) r_{\mathrm{loss,arm}}}}{1 - r_{\mathrm{ITM}}(d_{\mathrm{CML}}^{\mathrm{ITM}}) r_{\mathrm{ETM}}(d_{\mathrm{CML}}^{\mathrm{ETM}}) r_{\mathrm{loss,arm}}}. \end{aligned} \tag{3.18}$$

As the beam is split by a beam splitter, the intra-cavity power, $P_{\rm arm}$, is reduced by a factor of 2 and becomes

$$\begin{aligned} P_{\rm arm} &= \frac{1}{\pi}\mathcal{F}_{\rm arm}(d_{\rm CML}^{\rm ITM}, d_{\rm CML}^{\rm ETM})P_{\rm PRC} \\ &= \frac{1}{\pi}\mathcal{F}_{\rm arm}(d_{\rm CML}^{\rm ITM}, d_{\rm CML}^{\rm ETM})G(d_{\rm CML}^{\rm ITM}, d_{\rm CML}^{\rm ETM})P_{\rm in}. \end{aligned} \tag{3.19}$$

The part of the laser power is reflected at the interface of the vacuum and molecular layer surface and the incoming laser power is reduced. The power reflectance of molecular layer, $R_{\rm CML}$, is given by

$$R_{\rm CML} = \left|\frac{n_0 - n_{\rm CML}}{n_0 + n_{\rm CML}}\right|^2. \tag{3.20}$$

The incoming laser power into the molecular layer can be written as

$$P_{\rm CML} = P_{\rm arm}(1 - R_{\rm CML}). \tag{3.21}$$

Thus, assuming the Lambert-Beer law holds for the molecular layer, the amount of the optical absorption by the molecular layer can be estimated as

$$\begin{aligned} A_{\rm CML} = \frac{1 - R_{\rm CML}}{\pi}&\mathcal{F}_{\rm arm}(d_{\rm CML}^{\rm ITM}, d_{\rm CML}^{\rm ETM})G(d_{\rm CML}^{\rm ITM}, d_{\rm CML}^{\rm ETM}) \\ &\times P_{\rm in}[1 - \exp(-2\alpha_{\rm CML}d_{\rm CML})]. \end{aligned} \tag{3.22}$$

It should be noted that the index of the exponential is doubled by taking into account of the reflection of the coating.

3.4 Optical Loss Estimation

Table 3.1: The parameters to calculate the refractive indices. C_1 and C_2 are given by the previous report [71]. D_1 and D_2 are obtained by fitting using Eq. 3.23.

Symbol	$\sqrt{C_1}$	$\sqrt{C_2}$	D_1	D_2
Value	71	134	0.00996	0.0319

Some of future GWDs are planed to use cryogenic mirrors to achieve better sensitivity. Low optical absorption is critical for cryogenic GWDs both to

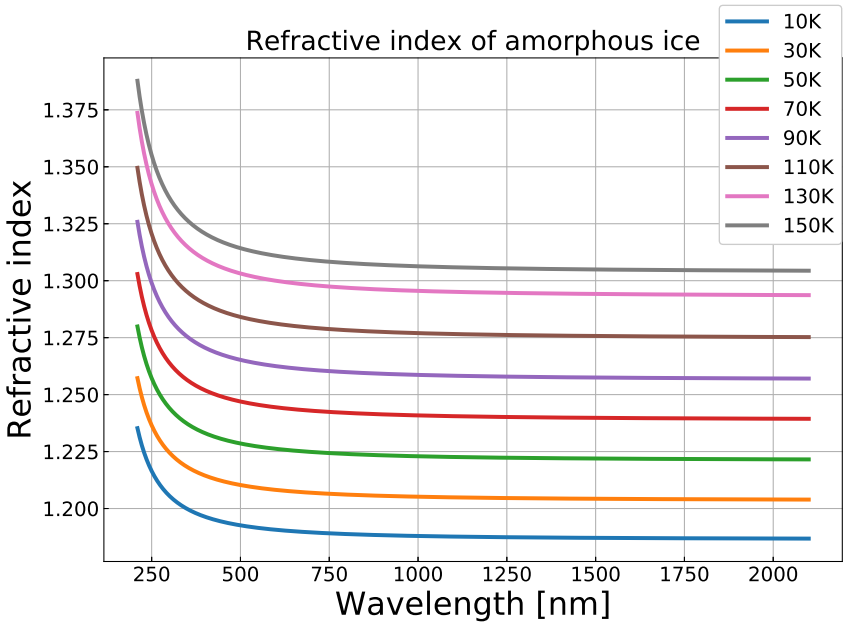

Figure 3.3: Refractive index of the amorphous ice for various temperatures derived by the Lorentz-Lorenz equation.

maintain the cryogenic temperature of the test mass and achieve the design sensitivity. As the arm cavity power is designed to be 18 kW and 3 MW for ET and LIGO Voyager, respectively, an additional heat absorption introduced by the CML can become a critical problem in maintaining cryogenic temperature of the test masses. We show the impacts of CML on the future GWDs which adopt cryogenic mirrors.

In order to evaluate the impact of the CML, we need several assumptions. First, we assume that the CML is composed of water as the previous works have done [58, 57]. In addition, the water molecular layer is formed as amorphous ice [72]. The refractive index of amorphous ice at the cryogenic temperature has been studied for the wavelength of $210 - 757$ nm [71]. We extrapolate the refractive index at 1064 nm, 1550 nm and 2000 nm by extrapolation using the Lorentz-Lorenz equation which gives the relation between the density ρ and the refractive index $n(\lambda)$ as

$$R(\lambda) = \frac{1}{\rho}\frac{n(\lambda)^2 - 1}{n(\lambda)^2 + 2}, \tag{3.23}$$

where $R(\lambda)$ is the specific refraction which can be expressed as

$$R(\lambda) = \sqrt{\frac{D_1\lambda^2}{\lambda^2 - C_1} + \frac{D_2\lambda^2}{\lambda^2 - C_2}}. \tag{3.24}$$

C_1, C_2, D_1 and D_2 are the parameters to explain the experimental result and C_1 and C_2 are given by the previous report [71]. D_1 and D_2 are obtained by fitting the data shown in the reference [71] using Eq. 3.23. The results are shown in Fig. 3.3 and the value of parameters are listed in Table 3.1. As there is no characteristic structure of H_2O molecule within the wavelength we discuss here, its refractive index monotonically decreases gently until 2 μm as shown in the reference [73]. Therefore, this extrapolation is a reasonable assumption to evaluate the effect of the CML. Furthermore, we use the literature value for the estimation of optical absorption. The absorption coefficient of amorphous ice has been reported at the temperature of 40 K and 140 K [60]. As the temperature dependence of the absorption coefficient is so weak between 40 K and 140 K, we adopt these literature values to calculate the absorption at 123 K. In addition, we assume that the absorption coefficient at 10 K is almost the same as the value at 40 K. The parameters which are used for the estimation are shown in Table 3.2.

3.4.1 KAGRA

First, let us revisit the case of KAGRA as the a reference for future GWDs. KAGRA is operated with cryogenically cooled sapphire mirrors at the temperature of 22 K with the wavelength of 1064 nm laser source [19, 20]. For the case of KAGRA, test masses are cooled by heat conduction through sapphire fibers which suspend them. The estimated heat extraction capacity is about 0.72 W [27], and the absorption in the coatings is less than 0.5 ppm [74, 39]. More details of the impacts of the CML formation on KAGRA are reported in the references [58, 59].

Fig. 3.4 shows estimated optical loss by scattering and absorption for KAGRA. Here we assumed the absorption coefficient as $\alpha = 2.2 \times 10^{-2}$ ppm/nm and other related parameters are listed in Tab. 2.2 [73]. Optical loss induced by scattering is less than 1 ppm as long as the thickness of the CML is below 1 μm even if the correlation length ξ equals to $\sigma_{\langle t \rangle}$. Assuming the uniform molecular injection onto the mirror surface, the correlation length, ξ, becomes small because it forms the tidy and smooth surface. Therefore, the impact of the scattering can be negligible when the thickness of the CML is below 1 μm.

Table 3.2: The assumed parameters of future cryogenic GWDs [30, 35]. Here we assume that the CML is composed by amorphous ice. The refractive indices of amorphous ice are derived by the fitting using Lorentz-Lorenz equation. It should be noted that the refractive indices at 22 K and 123 K are the averaged value of that at 10 K and 30 K, and 110 K and 130 K, respectively. The absorption coefficient of the CML is assumed the literature value [73, 60].

Parameters	Symbol	ET	Voyager
Temperature of the test mass	T	10 K	123 K
ITM transmittance	T_{ITM}	0.7%	0.2%
ETM transmittance	T_{ETM}	6 ppm	5 ppm
PRM transmittance	T_{PRM}	4.6%	4.92%
Loss inside the arm cavity	$T_{\mathrm{loss,arm}}$	75 ppm	10 ppm
Laser wavelength	λ	1550 nm	2000 nm
Laser power	P_{in}	3 W	152 W
Mirror thickness	d_{mir}	50 cm	55 cm
Refractive index of CML	n_{CML}	1.19	1.28
Absorption coefficient of CML	α_{CML}	2.0 ppm/nm	8.0 ppm/nm
Absorption in test mass	α_{mir}	3.2×10^{-2} ppm/cm	10 ppm/cm
Extractable heat	Q	100 mW	10 W

3.4.2 The Einstein Telescope

Einstein Telescope is a planned European GWD which will use cryogenic silicon mirrors at the temperature of 10 K with the wavelength of 1550 nm laser source for the low frequency part [69]. Extracting the heat generated by the absorption at the mirror surfaces has to be done by the thermal conduction of the suspension fibers because of the significantly low thermal radiation at cryogenic temperature of 10 K. The absorption in the coatings is designed to be 1 ppm, and the capacity of heat extraction by the suspension fibers is only 100 mW [30]. Therefore, the optical absorption should be kept as small as possible.

Fig. 3.5 shows the result of the optical loss by the scattering and absorption for ET. The impact of scattering can be negligible when the thickness of the CML is below 1 μm in the same manner as KAGRA. On the other hand, the absorption is remarkably large because of the use of a longer wavelength laser and has a potential to prevent a cryogenic operation due to the additional heat load to the test mass.

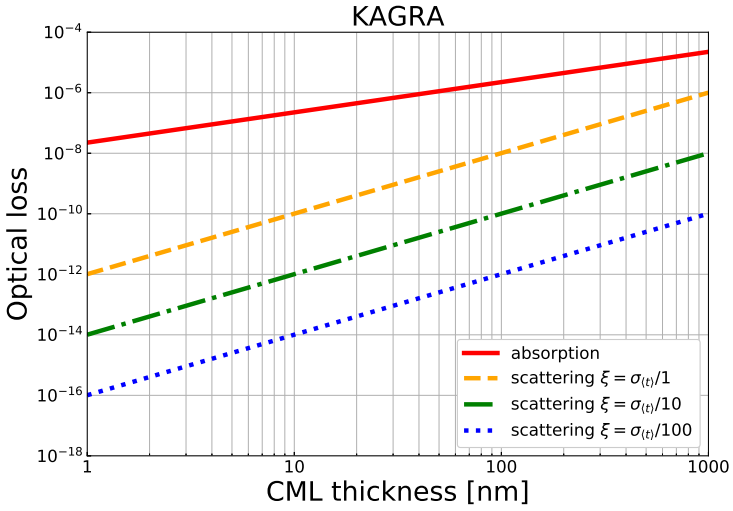

Figure 3.4: Scattering and absorption loss for the case of KAGRA. The assumed wavelength is $\lambda = 1064\,\mathrm{nm}$. Red solid line, yellow dashed line, green dashdot line and blue dotted line represent the absorption and scattering with the correlation length of $\xi = \sigma_{\langle t \rangle}, \sigma_{\langle t \rangle}/10$ and $\sigma_{\langle t \rangle}/100$, respectively.

3.4.3 LIGO Voyager

LIGO Voyager is a substantial upgrade of aLIGO, aiming to improve the inspiral range by a factor of 4 to 5 [35]. Silicon is also a candidate material for LIGO Voyager test masses and will be cooled down to 123 K. The laser wavelength is chosen to be $2\,\mu$m for LIGO Voyager in order to take advantage of lower absorption of amorphous silicon coating. The requirement on the absorption in the coatings is at most 1 ppm. The absorption coefficient of water molecule is, however, larger than that of at the wavelength of $1.5\,\mu$m. Furthermore, the arm cavity power is much larger than the case of ET, 3 MW. Therefore, the heat absorption when the CML is formed on the silicon mirror can become a serious heat source which prevents the operation at cryogenic temperature of 123 K.

Fig. 3.6 shows estimated optical loss by scattering and absorption for LIGO Voyager. Assuming the uniform molecular injection onto the mirror surface, the impact of scattering can be negligible as long as the thickness of the CML is below $1\,\mu$m in the same manner as the case of KAGRA and ET. On the other hand, the loss due to the absorption is much larger than the scattering and can be harmful for cryogenic operation.

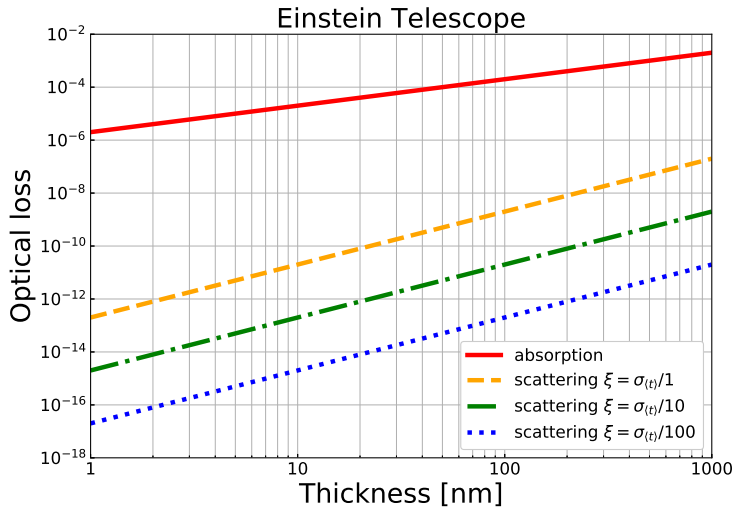

Figure 3.5: Scattering and absorption loss for the case of ET. The assumed wavelength is $\lambda = 1550\,\mathrm{nm}$. Red solid line, yellow dashed line, green dashdot line and blue dotted line represent the absorption and scattering with the correlation length of $\xi = \sigma_{\langle t \rangle}, \sigma_{\langle t \rangle}/10$ and $\sigma_{\langle t \rangle}/100$, respectively.

3.5 Performance of GWD

Optical loss induced by CMLs can reduce the optical performance of GWDs such as PRG. In the same manner as the previous study [16], here we estimate the impact on of CML PRG for future GWDs using Eq 3.15. More detailed calculations can be found in the references [58, 59]. We will derive the tolerable CML thickness to keep the degradation of PRG up less than 10%.

First, we revisit the PRG of KAGRA which is estimated in the previous study [58]. In the same manner as the previous study, we assume that the start time and the formation speed of CMLs are the same for both ITM and ETM. Also, we take changes in the refectivities of the test masses due to the CML formation into account as the previous study did [58]. Fig. 3.7 shows how the PRG of KAGRA changes with the CML thickness. Here we assumed that the refractive index of CML as $n_{\mathrm{CML}} = 1.26$ and the absorption coefficient as $\alpha_{\mathrm{CML}} = 2.2 \times 10^{-2}\,\mathrm{ppm/nm}$. The oscillation is induced by the change in reflectivities of test masses due to the CML formation. Especially, the reflctivities of arm cavities oscillate, which leads to the oscillation in the PRG of KAGRA. As the CML becomes thicker, the PRG decreases due to the optical loss of CML. The tolerable CML thickness can be as thick as 750 nm.

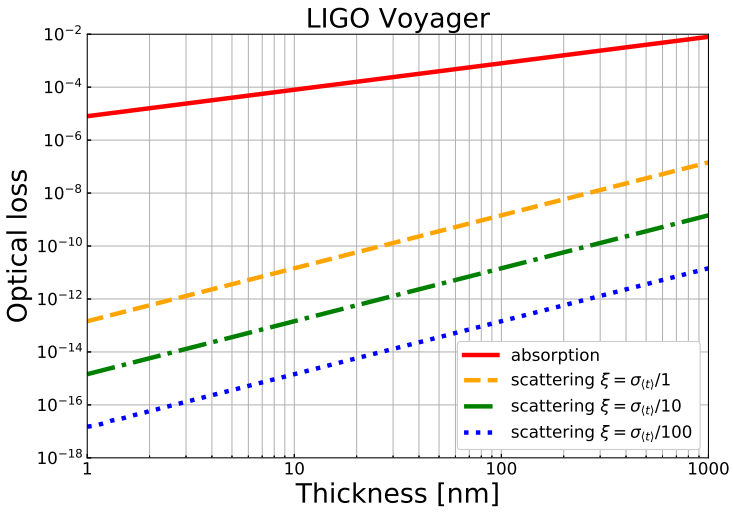

Figure 3.6: Scattering and absorption loss for the case of LIGO Voyager. The assumed wavelength is $\lambda = 2000\,\mathrm{nm}$. In the same manner as the case of ET, red solid line, yellow dashed line, green dashdot line and blue dotted line represent the absorption and scattering with the correlation length of $\xi = \sigma_{\langle t \rangle}, \sigma_{\langle t \rangle}/10$ and $\sigma_{\langle t \rangle}/100$, respectively.

Fig. 3.8 shows how the PRGs of the ET and LIGO Voyager change due to the CML formation, respectively. We assumed the refractive indices of CMLs of the ET and LIGO Voyager as $n_{\mathrm{CML,ET}} = 1.19$ and $n_{\mathrm{CML,Voyager}} = 1.28$, respectively. Also the assumed absorption coefficients are listed in Table 3.2. For the case of the ET and LIGO Voyager, PRGs decrease monotonically without oscillation. This is because the optical loss of CML is much larger than that of KAGRA and PRGs deteriorate before starting oscillation. The tolerable CML thickness is much smaller than that of KAGRA. For the case of the ET, the tolerable CML thickness is about 60 nm. Moreover, the tolerance of LIGO Voyager is thinner than the ET and it is about 25 nm. These values are about one order of magnitude smaller compared to 750 nm which is the tolerable CML thickness of KAGRA. Therefore, the performance of future cryogenic GWDs can be easily deteriorated due to the CML formation compared to KAGRA.

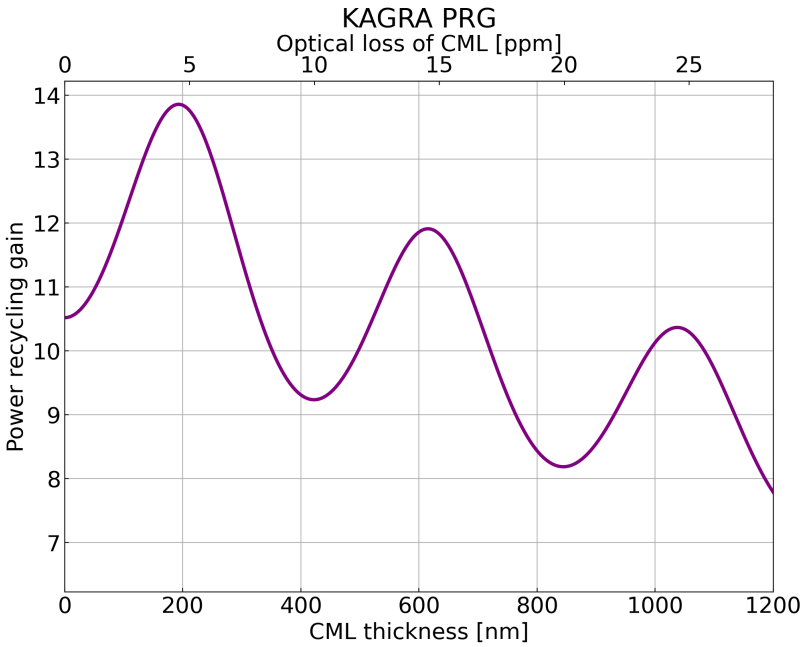

Figure 3.7: Power recycling gain of KAGRA against the thickness of CML.

3.6 Implications to Heat Input

Not only the degradation of PRG, but also the heat absorption by CMLs can prevent a cryogenic operation due to the additional heat load to test masses. For the case of KAGRA, as the intra-cavity power becomes about 370 kW, absorption at ppm level exceeds the capacity of heat extraction and leads to increase in the test mass temperature. In other words, a few tens of nm thickness CML can increase the temperature of test mass. Here we focus on a thin thickness range to estimate the heat absorption in which the power reflectance of the CML, finesse of arm cavity and power recycling gain can be considered to be constant. Therefore, the absorbed power by the CML is proportional to the thickness of CML, $A_{\mathrm{CML}} \propto \alpha_{\mathrm{CML}} d_{\mathrm{CML}}$.

Fig. 3.9 shows the heat absorption of the input test mass (ITM) and end test mass (ETM) of KAGRA. In this calculation, the absorption in the substrate and radiation from the beam ducts are taken into account. Once the thickness becomes larger than about 10 nm, the heat input to ITM exceeds the tolerable value, 0.72 W, and the temperature of test mass cannot reach the target value. Therefore, the thickness of CML should be kept less than about 10 nm in order to maintain the temperature of test mass. For ETM, the heat input is smaller as long as the thickness of CML is smaller than about 30 nm.

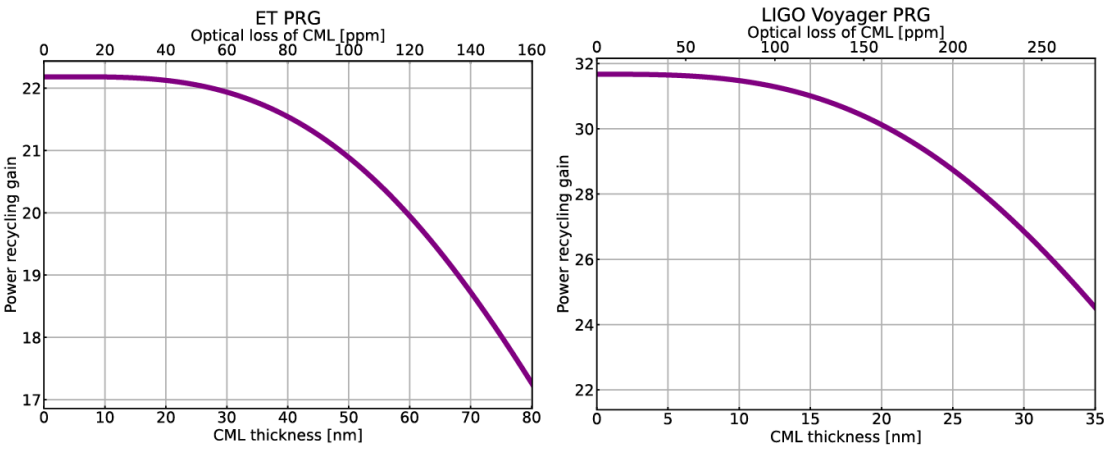

Figure 3.8: Power recycling gain of the ET against the thickness of CML.

Fig. 3.10 shows the heat absorption of the ITM and ETM of ET. Once the thickness becomes larger than a few nm, the heat input to the test masses exceeds the tolerable value, 100 mW, and the temperature of test mass cannot reach the target value. Therefore, the thickness of CML should be kept less than 1 nm in order to maintain the temperature of the test masses.

Fig. 3.11 shows the heat absorption of the ITM and ETM of LIGO Voyager. The heat load generated by the optical absorption is extremely large as the injected laser power is much larger than that of ET. Even if the thickness is less than 1 nm, the heat load is still more than 10 W for both the ITM and ETM cases. This indicates that the test mass cannot be cooled down to 123 K. Thus, not only the optical performance degradation, but also the heat absorption due to the CML may become a critical problem.

It should be noted that the heat input to a test mass becomes larger even at a thickness which can be tolerable from the view point of optical performance. For the case of the ET and LIGO Voyager, about 4 W and 1.7 kW heat should be extracted from test masses to keep the degradation of PRG less than 10%, respectively as shown in Fig. 3.12. However, it is practically almost impossible to achieve such large cooling capacity by each cooling method. In order to extract 4 W heat from the 10 K mirror by conductive cooling, the mirror needs to be connected close to cold head of cryocoolers with much thicker fibers, which can increase the suspension thermal noise and vibration contamination. Also, maximum extractable heat from the 123 K mirror by radiation is estimated as

$$P_{\mathrm{rad}} = \sigma T^4 S \approx 14\,\mathrm{W}, \tag{3.25}$$

where $\sigma = 5.67 \times 10^{-8}\,\mathrm{W/m^2/K^4}$ is the Stefan-Boltzmann constant, $T = 123\,\mathrm{K}$

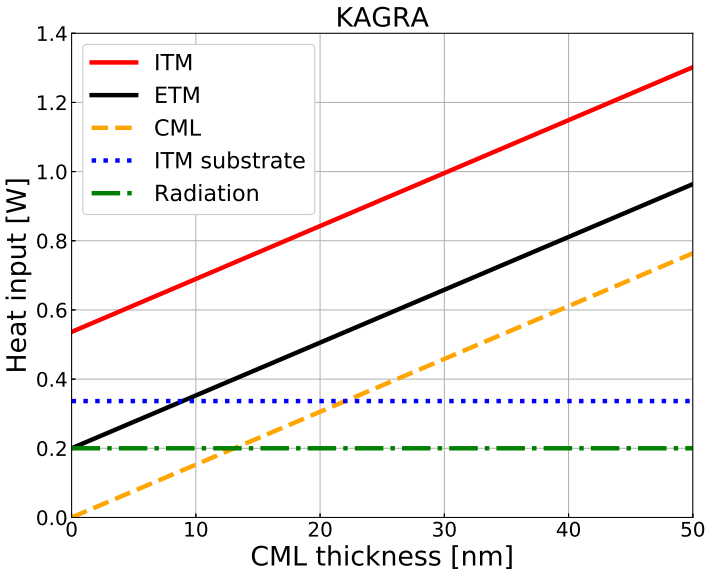

Figure 3.9: Heat input for the case of KAGRA. Red solid line and black solid line represent the heat input of the input test mass (ITM) and the end test mass (ETM), respectively. Yellow dashed line shows the contribution by the CML. Blue dotted line and green dashdot line are absorption by the ITM substrate and radiation from the beam duct, respectively.

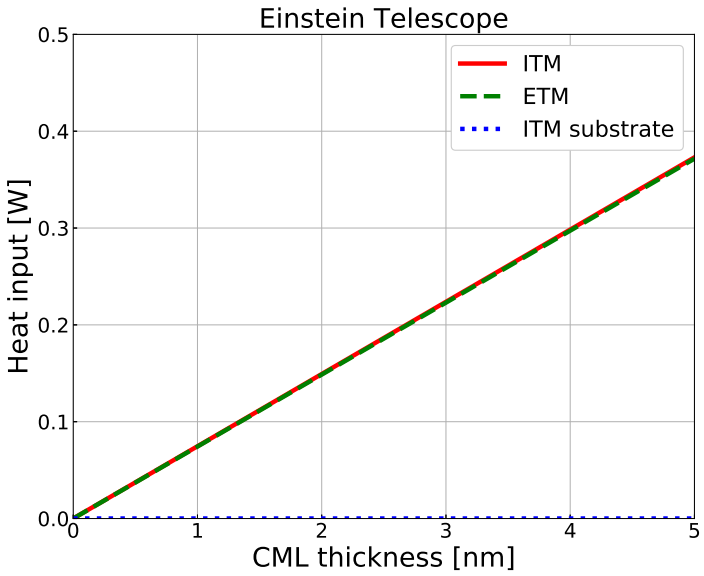

Figure 3.10: Heat input to each test mass mirror in the ET induced by the optical absorption of CML. As a result of strong absorption of amorphous ice, the heat load to test mass exceeds 100 mW even when the CML thickness is only a few nm. It should be noted that the radiation from the beam ducts is not taken into account for the case of ET.

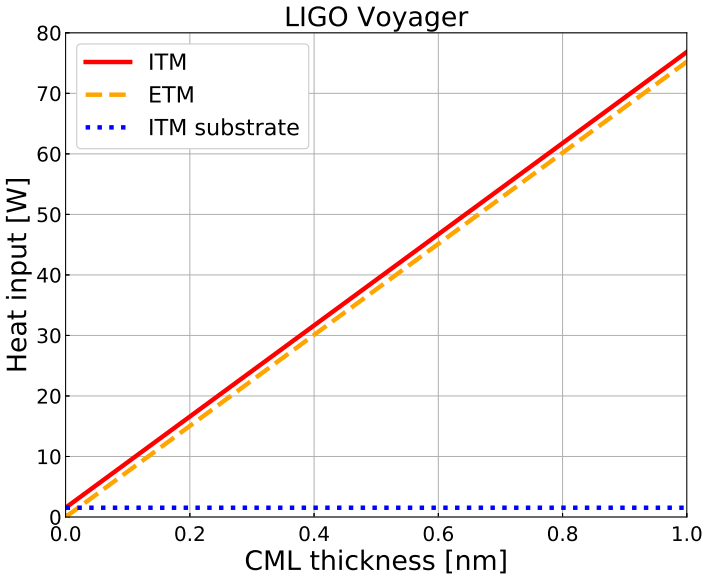

Figure 3.11: Heat input to each test mass mirror in LIGO Voyager induced by the optical absorption of CML. It should be noted that the radiation from the beam ducts is not taken into account for the case of LIGO Voyager.

is the temperature of the mirror, and S is the surface area of the mirror. Here we assumed the radius of the mirror to be 22.5 cm and the thickness of the mirror to be 55 cm [35].

3.7 Summary of this chapter

- Cryogenic mirrors in GWDs can introduce the CML on their surfaces due to the adsorption of residual gas molecules.
- The CML can become a problem not only for KAGRA, but also for the future GWDs such as the ET or LIGO Voyager. However, its impacts on the future GWDs have not been studied nor taken into account.
- The CML induces additional optical losses which can degrade the detector's performance and hence less number of detection of GW events.
- As the ET and LIGO Voyager are planning to employ longer wavelength lasers, the optical absorption by CML can become crucial due to the large absorption coefficient of amorphous ice.

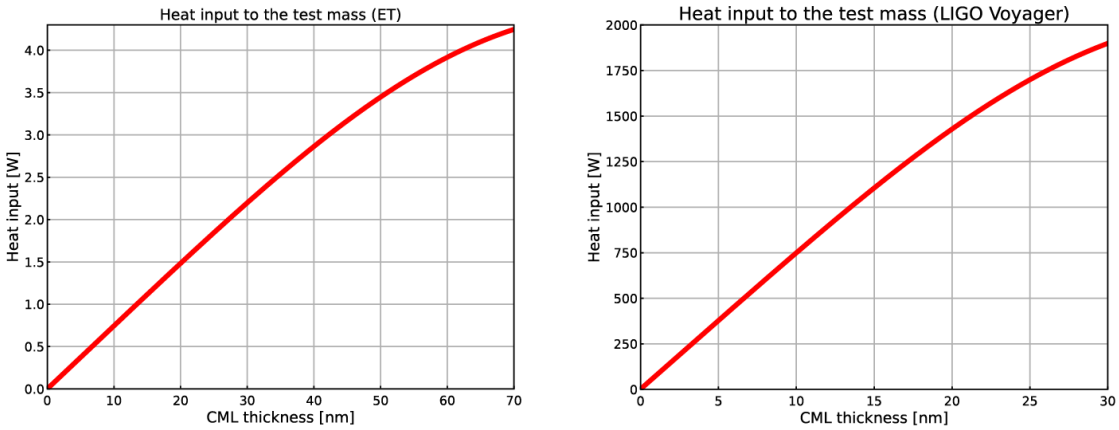

Figure 3.12: Heat input to test masses for the case of the ET and LIGO Voyager.

- We have estimated the tolerable CML thickness from the view point of optical performance of GWDs. The tolerable thickness of future GWD is 2 order of magnitudes smaller than that of KAGRA.
- The heat input induced by CMLs can exceed the cooling capacity of the ET and LIGO Voyager due to the large absorption coefficient of amorphous ice.

Chapter 4

Development of Cryogenic Folded Cavity

The optical loss induced by the CML can spoil the sensitivity or even operation of cryoegenic GWDs, hence, the detection of GWs can be hindered. In order to mitigate or solve this problem, study about the CML is necessary. So far, there has not been any studies about the impact of CML on GWDs at longer wavelength than 1064 nm though the future GWDs will presumably employ longer wavelength laser. For the case of the ET, 1550 nm wavelength laser will be used for lower-frequency part with 10 K test mass mirrors. In order to explore the feasibility of future GWDs, i.e., longer wavelength laser interferometric GWDs, the experiment conducted at the same wavelength is indispensable.

In this chapter, we explain about the setup of the measurement system which we have developed. First, we revisit the features of an optical cavity. Then, we describe the experimental setup including the folded cavity. In addition, the cryogenic system is a unique feature in this experiment and it takes important roles to develop future cryogenic gravitational-wave detectors. The cryogenic system is described briefly in the following subsection.

4.1 Optical Cavity

Optical cavities are widely used in precision measurements such as gravitational-wave detection or optical lattice clock [20, 75]. The optical cavity is a device formed by two or more partial reflectors to store or reject photons in the cavity. In particular, those formed by two mirrors facing each other is known as the Fabry-Perot (FP) cavity. In this section, we describe the fundamental properties of the optical cavity [76].

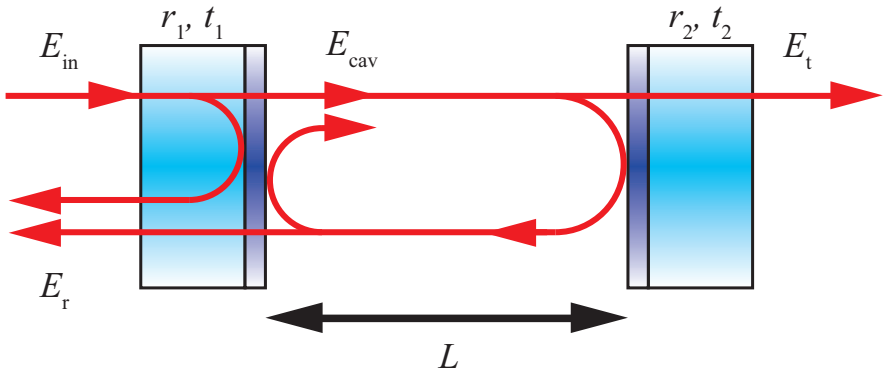

Figure 4.1: Schematic picture of FP cavity.

4.1.1 Static Response

Assuming that the cavity is under a static condition where there are no rapid variations neither in the fields nor the cavity length, a set of the fields associated with the cavity can be written as

$$E_{\mathrm{cav}} = t_1 E_{\mathrm{in}} + r_1 r_2 E_{\mathrm{cav}} e^{-2ikL}, \tag{4.1}$$

$$E_{\mathrm{r}} = -r_1 E_{\mathrm{in}} + \frac{t_1}{r_1}\left(E_{\mathrm{cav}} - t_1 E_{\mathrm{in}}\right), \tag{4.2}$$

$$E_{\mathrm{t}} = t_2 E_{\mathrm{cav}}, \tag{4.3}$$

where E_{in}, E_{cav}, E_{r}, and E_{t} are incident, intra-cavity, reflected, and transmitted fields, respectively. r_j and t_j are the amplitude refrectivity and transmissivity of j-th mirrors where $j = 1, 2$, and k and L are the wave number and cavity length, respectively. From Eq. 4.1, the intra-cavity field can be expressed as

$$E_{\mathrm{cav}} = \frac{t_1}{1 - r_1 r_2 e^{-2ikL}} E_{\mathrm{in}}. \tag{4.4}$$

Thus the intra-cavity power P_{cav} can be expressed as

$$P_{\mathrm{cav}} \equiv |E_{\mathrm{cav}}|^2 = \frac{t_1^2}{|1 - r_1 r_2 e^{-2ikL}|^2} |E_{\mathrm{in}}|^2 . \tag{4.5}$$

This represents the amount of the laser power stored inside the cavity. Fig. 4.2 shows the intra-cavity power as a function of the round trip phase which is defined as

$$\phi_{\mathrm{rtp}} \equiv 2kL = \frac{4\pi L}{\lambda}, \tag{4.6}$$

where λ is the laser wavelength. The FP cavity is on resonance when the round trip phase satisfies the following condition,

$$\phi_{\mathrm{rtp}} = 2\pi n, \tag{4.7}$$

where n is an arbitrary integer. When the cavity is on resonance, the intra-cavity power becomes the maximum. The resonant condition can also be expressed as,

$$2\pi n = \frac{4\pi \nu L}{c}, \tag{4.8}$$

where n is an arbitrary integer, and ν, L and c are the laser frequency, the cavity length and the speed of light, respectively. Taking the derivation of both sides in the equation above, one can find

$$\frac{\Delta\nu}{\nu} = -\frac{\Delta L}{L}. \tag{4.9}$$

Thus, the length variations, ΔL, are linearly imprinted onto the laser frequency fluctuations, $\Delta\nu$, as long as the cavity is on resonance through the frequency locked loop.

4.1.2 Characteristic Quantities

In this subsection, we briefly introduce a number of important quantities which characterize an optical cavity.

Free Spectral Range

Free Spectral Range (FSR) is a measure of the separation between the neighboring resonances in terms of the laser frequency which is defined by

$$f_{\mathrm{FSR}} = \frac{c}{2L}. \tag{4.10}$$

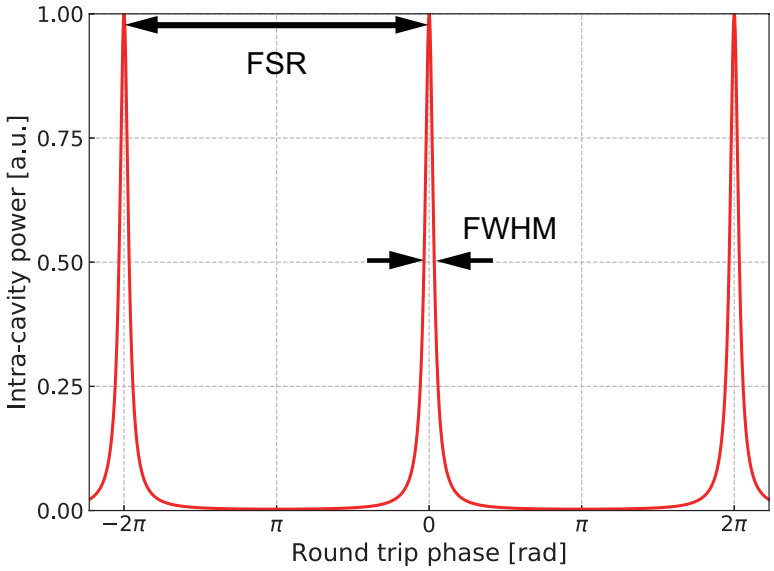

Figure 4.2: The intra-cavity power.

Finesse and Linewidth

The finesse $\mathscr{F}$ denotes the sharpness of the resonances which can be a merit of optical cavities. It can be approximated as

$$\mathscr{F} \equiv \frac{f_{\mathrm{FSR}}}{f_{\mathrm{FWHM}}} = \frac{\pi\sqrt{r_1 r_2}}{1 - r_1 r_2}. \tag{4.11}$$

Once the fincesse is determined, one can compute the corresponding linewidth in terms of the full width at half maximum (FWHM) by

$$f_{\mathrm{FWHM}} = \frac{f_{\mathrm{FSR}}}{\mathscr{F}}. \tag{4.12}$$

Here f_{FWHM} represents the linewidth with respect to the laser frequency.

Storage Time and Cavity Pole

The storage time τ_{s} denotes the mean duration for a photon to stay in the cavity. It is expressed as

$$\tau_{\mathrm{s}} = \frac{2L}{c}\frac{1}{\ln(r_1 r_2)} \approx \frac{2L}{\pi c}\mathscr{F}. \tag{4.13}$$

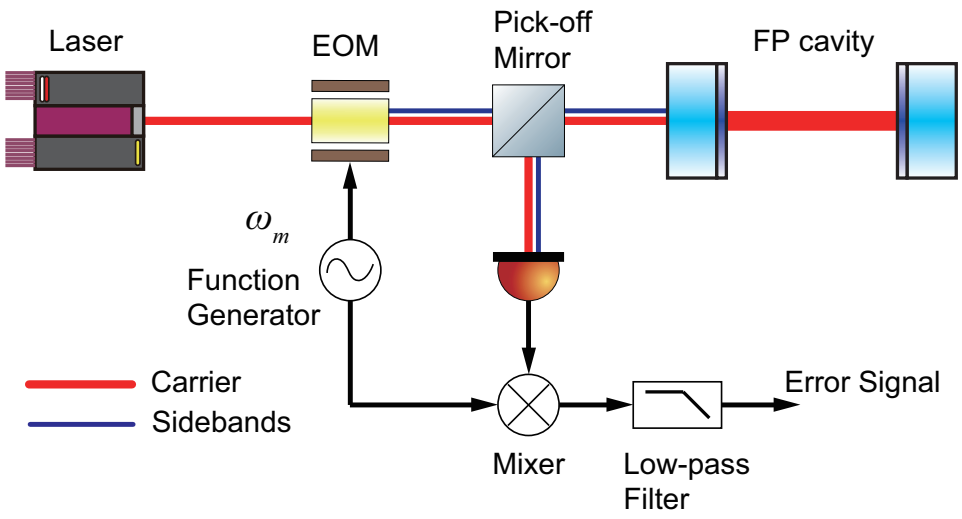

Figure 4.3: Schematic picture of the PDH locking. The beat note between the promptly reflected sidebands and the leakage of carrier is detected by RFPD. The obtained signal is demodulated by using a mixer and then the error signal can be extracted by the low-pass filter.

The last approximation is valid as long as $r_1 r_2 \sim 1$.

The cavity pole f_c represents the frequency above of which an induced variation in the intra-cavity field cancels. The cavity pole essentially originates from the fact that a cavity has a finite storage time. It is related with the storage time as the following form,

$$f_c = \frac{1}{2\pi\tau_s}. \tag{4.14}$$

4.2 Locking Scheme

In order to maintain the resonant condition, the active feedback control is indispensable to stabilize the lase frequency of cavity length. Here we stabilize the laser frequency to keep resonant condition by using the Pound-Drever-Hall (PDH) locking scheme [77]. In this subsection, the principle of the (PDH) scheme is described.

For the PDH locking, an electro-optic modulator (EOM) is usually employed to modulate the phase. The phase modulated input laser field can be expressed as,

$$E_{\rm in} = E_0 \exp\left[i(\omega_0 t + \Gamma \sin\omega_{\rm m} t)\right], \tag{4.15}$$

where Γ is the modulation depth which represents the amount of the phase modulation. By using the Jacobi-Angar expansion, one can obtain

$$E_{\mathrm{in}} = E_0 e^{i\omega_0 t} \sum_{k=-\infty}^{\infty} J_k(\Gamma) e^{ik\omega_{\mathrm{m}} t}, \tag{4.16}$$

where $J_k(\Gamma)$ is the Bessel function of the first kind. One can see that a monochromatic phase modulation split the injected field into multiple components. The field with $k = 0$ is called a carrier, and the other fields $k \neq 0$ are called sidebands.

Assuming the modulation depth is small such that one can ignore the higher order of sidebands, the incident field is expressed as a sum of three fields,

$$E_{\mathrm{in}} = E_0 \left[J_0(\Gamma) e^{i\omega_0 t} + J_1(\Gamma) e^{i(\omega_0+\omega_{\mathrm{m}})t} - J_1(\Gamma) e^{i(\omega_0-\omega_{\mathrm{m}})t} \right]. \tag{4.17}$$

Here we use the fact that $-J_1 = J_{-1}$. When the incident field is coupled to the optical cavity, the reflected field can be expressed as

$$E_{\mathrm{r}} = E_0 e^{i\omega_0 t} \left[J_0((\Gamma) r(0) + J_1(\Gamma) r(\omega_{\mathrm{m}}) e^{i\omega_{\mathrm{m}} t} - J_1(\Gamma) r(-\omega_{\mathrm{m}}) e^{-i\omega_{\mathrm{m}} t} \right], \tag{4.18}$$

where $r(\omega_{\mathrm{m}})$ represents the amplitude reflectivity of the cavity at angular frequency of $\omega_0 + \omega$. Then the reflected beam power is calculated as

$$P_{\mathrm{r}}(t) = \left| r(\delta\omega) J_0(\Gamma) + J_1(\Gamma) \left[r_+(\delta\omega) \mathrm{e}^{i\omega_m t} - r_-(\delta\omega) \mathrm{e}^{-i\omega_m t} \right] \right|^2 P_{\mathrm{in}}, \tag{4.19}$$

where P_{in} is the input beam power. Here we define a reflectivity $r_\pm(\delta\omega)$ as

$$r_\pm(\delta\omega) \equiv r(\delta\omega \pm \omega_{\mathrm{m}}), \tag{4.20}$$

where $\delta\omega$ is an angular frequency difference between the carrier and the resonant frequency. An error signal can be extracted by demodulating the obtained signal as

$$\frac{\epsilon}{P_{\mathrm{in}}} = \frac{4 J_0(\Gamma) J_1(\Gamma) \mathcal{F}}{\pi \nu_{\mathrm{FWHM}}} \delta\omega. \tag{4.21}$$

Thus one can derive the error signal which is proportional to $\delta\omega$ by using the PDH scheme. Fig. 4.3 shows the schematic picture of the PDH locking.

Fig. 4.4 shows the PDH signal. The linear range of a typical PDH signal is narrow as indicated in the figure. In order to keep the resonance condition, the feedback control is necessary.

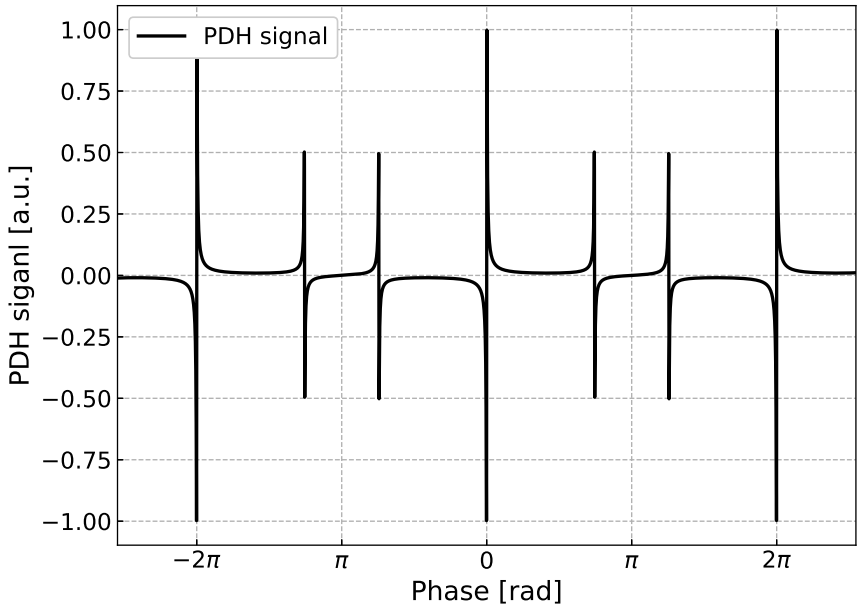

Figure 4.4: The typical PDH signal.

4.3 Folded Cavity

A folded cavity, consisting of input and output mirrors and one folding mirror, is employed in this experiment. Fig. 4.5 shows the schematic of the folding cavity. Though a typical FP cavity involved measurement sets the upper limit on the reflectivity of mirror, a folded setup enables us to measure the performance of high reflective coatings, resulting in tiny transmitted beam. Furthermore, one can conduct measurement to various coating materials just by changing only one folding mirror, which reduces the cost for the development of coatings. Therefore, the folded cavity is a notable method to measure and compare coating performance, and develop high-end coatings.

In our measurement system, the folded cavity is installed inside a cryostat chamber in order to cool down the cavity. Details of the set up is describe in the following sections.

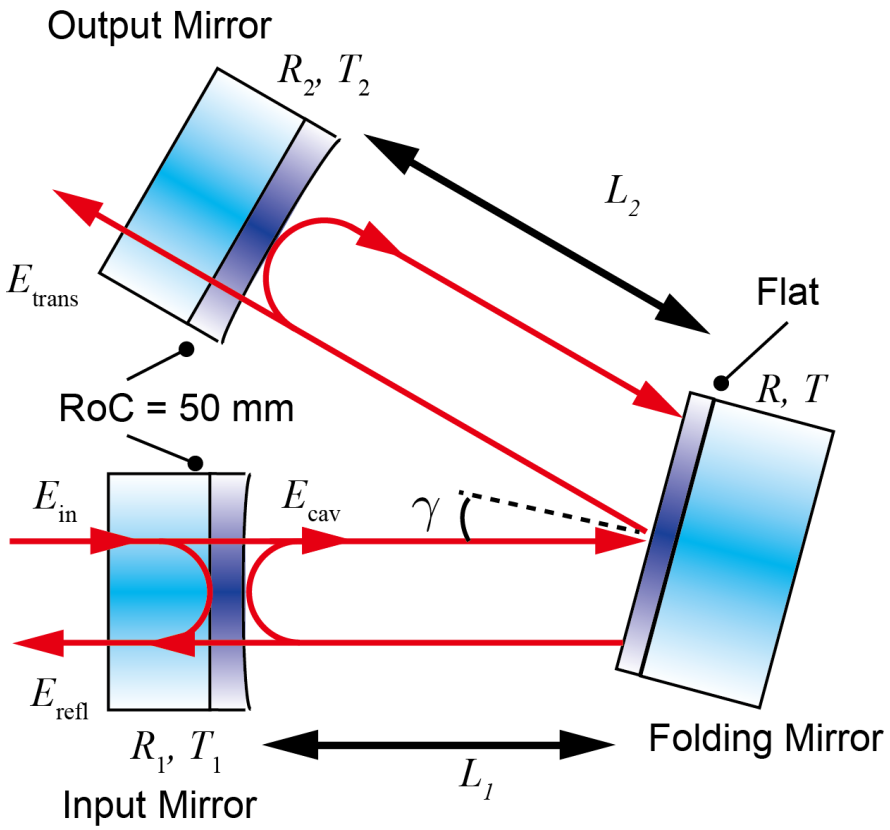

Figure 4.5: Schematic picture of the folded cavity. The folded cavity consists of three mirrors — input and output mirrors, and one apex mirror which fold the beam axis.

4.3.1 Static Response

First, we describe the static response of the folded cavity.

$$E_{\mathrm{cav}} = t_1 E_{\mathrm{in}} + r_1 r_2 r^2 E_{\mathrm{cav}} e^{-2ik(L_1+L_2)}, \tag{4.22}$$

$$E_r = -r_1 E_{\mathrm{in}} + \frac{t_1}{r_1}\left(E_{\mathrm{cav}} - t_1 E_{\mathrm{in}}\right), \tag{4.23}$$

$$E_t = t_2 E_{\mathrm{cav}}, \tag{4.24}$$

where $r_i^2 = R_i\,(t_i^2 = T_i)\quad (i = 1, 2)$ are the reflectivity (or transmittivity) of the input and output mirrors, respectively, and $r^2 = R$ and $t^2 = T$ are the reflectivity and transmittivity of the folding mirror. From Eq. 4.22, the

intra-cavity field can be expressed as

$$E_{\mathrm{cav}} = \frac{t_1}{1 - r_1 r_2 e^{-2ikL}} E_{\mathrm{in}}. \tag{4.25}$$

Hence, the intra-cavity power of the folded cavity is expressed as

$$P_{\mathrm{cav}} = \frac{t_1^2}{\left|1 - r_1 r_2 r^2 e^{-2ik(L_1+L_2)}\right|^2} P_{\mathrm{in}}. \tag{4.26}$$

Then, transmitted power can be written as

$$P_{\mathrm{trans}} = \frac{t_1^2}{\left|1 - r_1 r_2 r^2 e^{-2ik(L_1+L_2)}\right|^2} P_{\mathrm{in}} \tag{4.27}$$

With the active control loops, they satisfy the resonance condition,

$$2\pi n = \frac{4\pi\nu(L_1 + L_2)}{c}, \tag{4.28}$$

where n is an arbitrary integer, and ν, L and c are the laser frequency, the cavity length and the speed of light, respectively.

In the same manner as the FP cavity, one can define the free spectral range (FSR) and finesse as

$$f_{\mathrm{FSR}} = \frac{c}{2(L_1 + L_2)}, \tag{4.29}$$

$$\mathscr{F} = \frac{\pi\sqrt{r_1 r_2}}{1 - r_1 r_2 r^2}. \tag{4.30}$$

4.3.2 Input and Output Mirrors

Fused silica mirrors are used for the input and output mirrors. Both of them are half inch diameter size, and the radius of curvature is 50 mm. The reflectance of these fused silica mirrors was chosen to $R = 0.9998$ in order to set the cavity finesse as $\mathscr{F} \approx 15000$. These mirrors are attached to the mirror holders by gluing.

Initially, we planned to install silicon mirrors for both the input and output mirrors. However, the silicon mirrors we planned to use turned out not to satisfy the requirement, and was almost impossible to compose an optical cavity due to the large optical loss. This drove us to make new mirrors, but due to the limited budget we decided to use fused silica.

Figure 4.6: Picture of fused silica and silicon mirrors.

4.3.3 Folding Mirror

The geometry of the cavity is folded by a mirror, which is located at the apex of the cavity spacer. The size of the folding mirror is also half inch in diameter and its substrate is made of silicon which is the candidate material for future GWDs. The temperature sensor, DT-670, manufactured by Lake Shore Cryotronics Inc. is attached on the mirror holder of the folding mirror by using the indium sheet. We regard this measured temperature as the temperature of the folding mirror. The sensor has high stability for cryogenic operation [78]. Typical SiO_2/Ta_2O_5 coating, which are also employed in KAGRA test masses, is applied on the surface. The total pairs of coating layers are $N = 20$ in order to achieve the high reflectivity at 1550 nm.

4.3.4 Geometrical Parameters

Here we introduce geometrical parameters of the folded cavity. Fused silica mirrors with the radius of curvature of $R = 50$ mm are employed as the input and output mirrors. The cavity length $L = L_1 + L_2$ is chosen as $L_1 = L_2 = 41$ mm, hence 82 mm. Some parameters which characterize the folded cavity

Table 4.1: The parameters of the folded cavity. The reflectivities of mirrors are the value from their spec sheets.

Parameters	Value
Designed finesse	$\sim 1.5 \times 10^4$
Cavity length	$L_1 = 41\,\mathrm{mm}$
	$L_2 = 41\,\mathrm{mm}$
	$L = L_1 + L_2 = 82\,\mathrm{mm}$
Free spectral range	1.83 GHz
Beam size on the input/output mirror	$230\,\mu\mathrm{m}$
Beam size on the folding mirror	$97\,\mu\mathrm{m}$
Radius of curvature	50 mm
$R_1 = r_1^2, r_2^2$	0.9998 ± 0.0001
$T_1 = t_1^2, t_2^2$	~ 0.00017
$R = r^2$	0.999998
Folding angle	15 deg

can be calculated as bellow[76].

$$w_0 = \sqrt{\frac{L\lambda}{\pi}\sqrt{\frac{1+g}{4(1-g)}}}, \tag{4.31}$$

$$f_{\mathrm{FSR}} = \frac{c}{2L}, \tag{4.32}$$

$$f_{\mathrm{TMS}} = \frac{c}{\pi L}\frac{\arccos(g^2)}{\pi}, \tag{4.33}$$

where $g = 1 - L/R$ is a g-factor of the cavity and $\lambda = 1550\,\mathrm{nm}$ is wavelength of the laser beam. When the cavity length $L = 82\mathrm{mm}$, the optical parameters are calculated as below.

$$w_0 = 97\,\mu\mathrm{m}, \tag{4.34}$$

$$f_{\mathrm{FSR}} = 1.83\,\mathrm{GHz}, \tag{4.35}$$

$$f_{\mathrm{TMS}} = 1.34\,\mathrm{GHz}. \tag{4.36}$$

Here f_{TMS} denotes the frequency separation between two neighbouring spatial modes. The beam spot size on the mirror becomes $w_{\mathrm{m}} = 230\,\mu\mathrm{m}$. Related parameters are listed in Tab. 4.1.

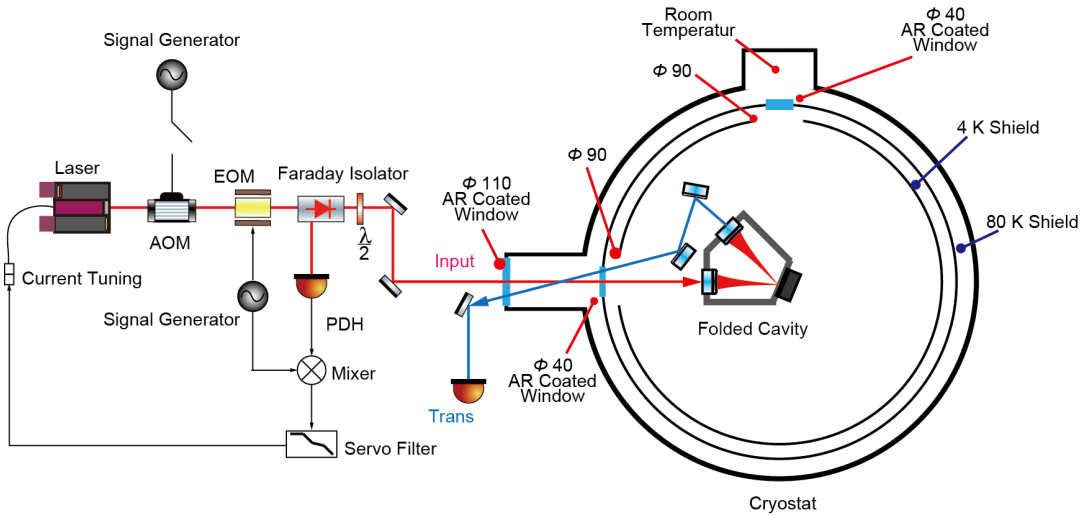

Figure 4.7: The overview of the experimental setup. The AOM is used for interrupting the laser injection to the cavity, and 1st diffracted beam is used for injection. The reflected beam for PDH locking is extracted by the Faraday isolator. The laser is locked to the cavity by feeding back the error signal to the laser through its current tuning. The output from the folded cavity is picked off by the mirror and detected by a PD.

4.4 Optical Layout

Fig. 4.7 shows the optical layout. The laser is phase-modulated by an EOM and the reflcted beam is picked-off by a Faraday-isolator which is used for PDH locking. The obtained error signal is filtered by a servo, and then fed back to the laser frequency through current tuning.

An AOM is used as a switch to turn off the injection of the laser beam into the cavity. Here, the first-order diffracted beam is injected to the cavity. By interrupting the AOM drive, the cavity input light could be extinguished on a timescale of $\sim 10\,\mathrm{ns}$ which is much smaller than the timescale of the cavity response. The PD also has enough fast response to detect the transition of the transmitted beam. Therefore, their influences are enough small for the ringdown measurement.

4.5 Spacer

Three mirrors which form the folded cavity are attached to the spacer made of an invar. The invar IC-DX employed here can be used even at 4 K cryo-

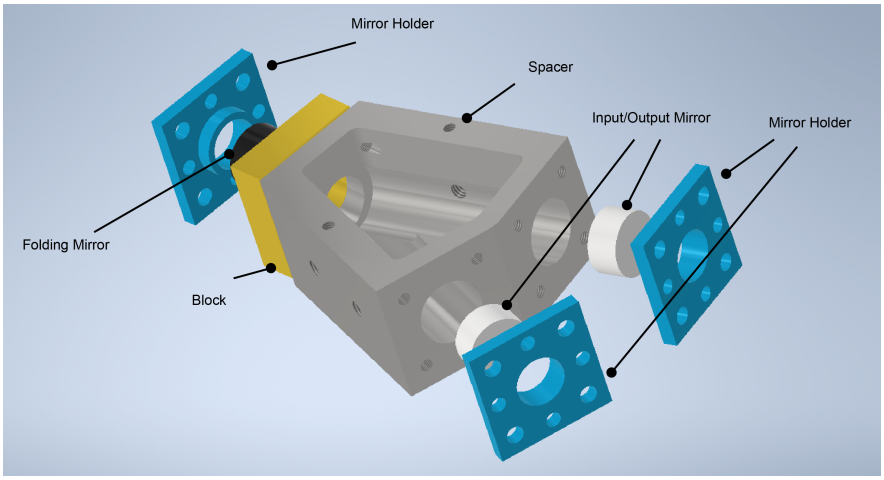

Figure 4.8: 3D CAD of exploded view of the folded cavity. The color of each component is displayed just for distinguishing the parts. The input and output mirror is glued on the mirror holders

genic temperature where typical invars show martensitic transformation, and is suited to this application.

The main purpose to use the spacer is to mitigate the misalignment caused by cooling process. Usual mirror holders show temperature drift in their alignment which can ruin the axis of optical cavity. Especially, the folded cavity used in this measurement is near concentric, and require strict alignment. Therefore, one have to reduce the thermal drift of three mirrors as much as possible. The invar used here has small enough thermal expansion coefficient down to 4 K to maintain the initial alignment, and this is why we employed the invar-made spacer. Also the use of the invar has additional advantages that one can save the cost to develop the optical cavity compared to the silicon or fused silica substrate spacer, and that one can replace the folding mirror much easier compared to the optical contact. These features drive the development of the coatings efficiently.

Fig. 4.8 shows the assembled folded cavity.

4.6 Vacuum and Cryogenic System

A cryostat is used for housing the cavity. As shown in Fig. 4.9, the cryostat chamber has three shields — 300 K shield, 80 K shield, and 4 K shield. Two of them except for the outermost shield (300 K shield) are covered by super insulator (SI) for efficient shielding of thermal radiations.

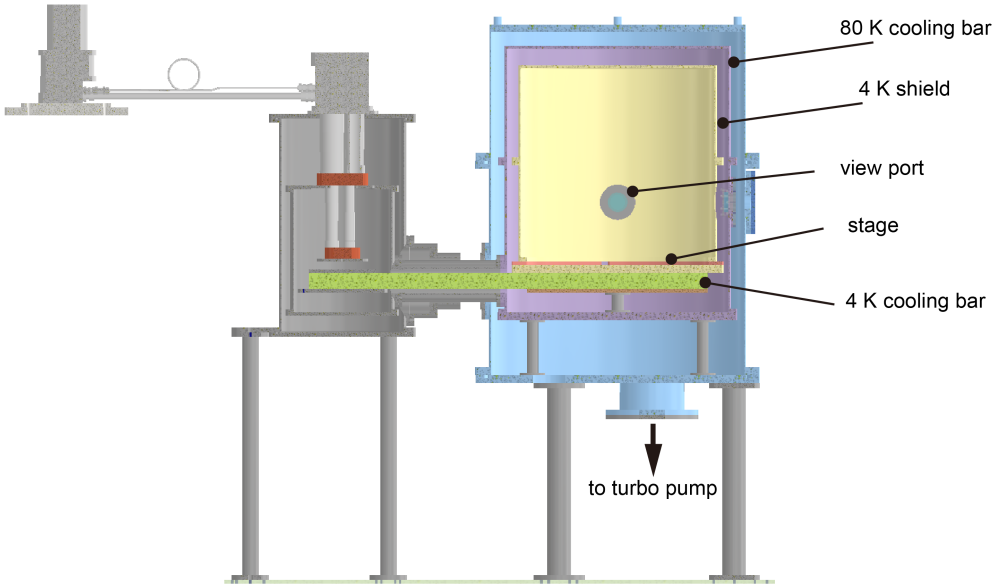

Figure 4.9: Schematic of cross section of cryostat. Two shields are installed inside the cryostat chamber at temperature of 80 K and 4 K, respectively. The chamber is pumped down by using a scroll pump and turbo pump. The beam is injected through the view port where AR windows are attached.

The cryostat has two types of pumps for vacuum. One is a scroll pump which is used for initial pumping down to about 10 Pa. The other is a turbo pump which achieves high vacuum environment. The vacuum pressure in the chamber can reach 6×10^{-4} Pa by using the turbo pump at room temperature.

The viewport window has AR coating at the wavelength of 1550 nm in order to reduce the power loss. The power loss at this viewport is measured to be $\sim 0.1\%$.

A pulse tube cryo-cooler is used for cooling down the cavity. A cooling bar is connected to the table in the chamber, and it cool down the system. The folded cavity is installed on the table in the cryostat chamber with aluminum pedestal which extracts heat from the cavity.

The pressure inside the chamber decreases due to the cryopumping effect. After reaching about 8 K, the pressure of room temperature part, i.e., between the room temperature and the 80 K shields, becomes $\sim 2 \times 10^{-5}$ Pa.

Table 4.2: The parameters of the laser source.

Parameters	Value
Wavelength	1550 nm
Power	20 mW
linewidth	$\leq$ 5 kHz

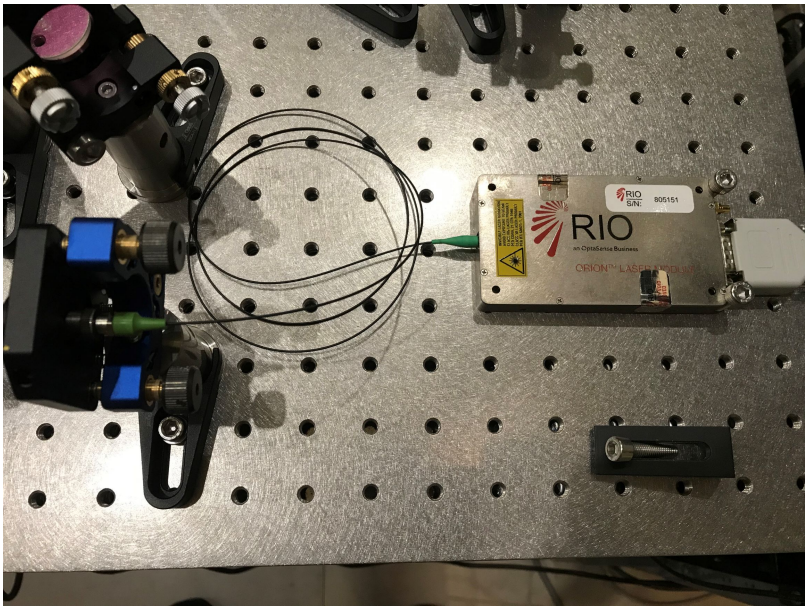

Figure 4.10: Picture of the laser source. A butterfly-packaged PW-ECL, current drivers, a frequency tuning terminal and a digital control interface are housed in the module.

4.7 Laser Source

We employed here a commercial laser module (named ORION), built by RIO. The module houses a butterfly-packaged PW-ECL, current drivers, a frequency tuning terminal and a digital control interface. This laser has low frequency noise, intensity noise and high stability for precision measurements with low cost [79]. Basic specifications of the laser are listed in Table 4.2, and Fig. 4.10 shows the appearance of the laser source.

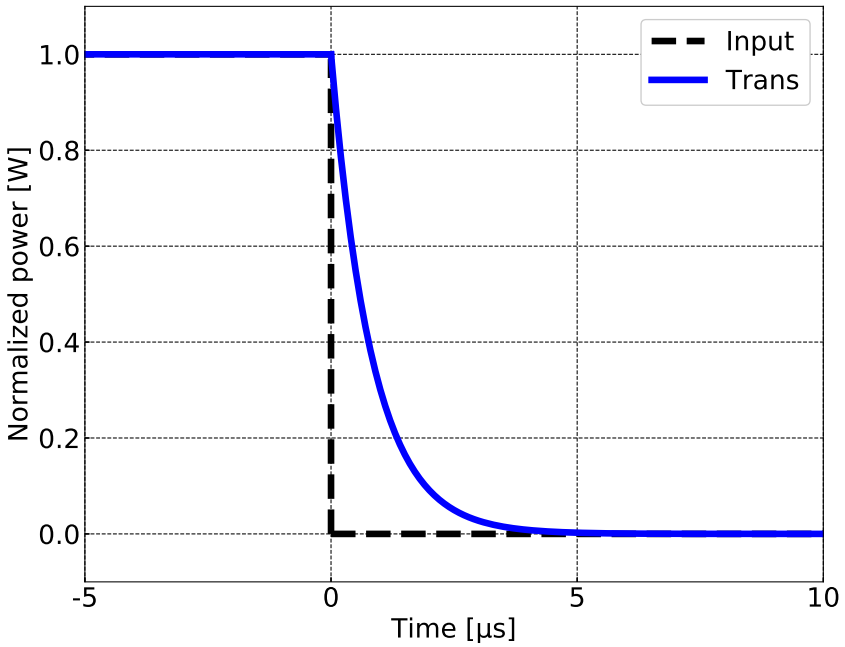

Figure 4.11: A transient response of an optical cavity. We assumed $\mathscr{F} \approx 1.5\times10^4$ with cavity length of $L = 10\,\mathrm{cm}$. Black dotted line represents the input beam power which is interrupted at $t = 0$. The blue line is the transmitted beam power which decays exponentially.

4.8 Finesse Measurement Methods

In this section, we describe the ringdown method to measure the finesse of the cavity. In this method, we employ the AOM to turn off the input laser. By interrupting the driver to the AOM, one can cut the input beam and cause the power stored in the cavity to decay, resulting in transient of the transmitted beam as shown in Fig. 4.11. By measuring the decay time of transmitted beam, one can calculate the finesse of the cavity.

The incident field with intensity modulation is expressed as

$$E_{\mathrm{in}} = E_0 e^{i\omega_0 t}(1 + \xi e^{i\omega_{\mathrm{m}} t} + \xi e^{-i\omega_{\mathrm{m}} t}), \tag{4.37}$$

where ξ and ω_{m} are the modulation depth and modulation angular frequency, respectively.

We consider the response of the folded optical cavity, assuming that the laser with $\omega_0 + \omega_\mathrm{m}$ angular frequency is injected to the cavity. One can define the transfer function of the cavity as

$$C \equiv \frac{E_\mathrm{t}}{E_\mathrm{in}}. \tag{4.38}$$

This can be expressed as

$$C = \frac{t_1^2 e^{-iL\omega_\mathrm{m}/c}}{1 - r_1^2 r^2 e^{-2iL\omega_\mathrm{m}/c}}. \tag{4.39}$$

Here we assumed that the cavity is kept on resonance to the carrier, which has the angular frequency of ω_0. Then the gain of the transfer function becomes

$$|C| = \frac{g}{\sqrt{1 + (\tau_\mathrm{s}\omega_\mathrm{m})^2}}, \tag{4.40}$$

where $g = t_1^2/(1 - r_1^2 r^2)$ is the gain factor of the cavity. Eq. 4.40 represents the response of the optical cavity to the intensity modulation, and it works as the 1st order low-pass filter with time constant of τ_s. From Eq. 4.40, one can derive the step response of the optical cavity as

$$\mathcal{L}^{-1}\left[\frac{1}{s}\frac{a_0}{1 + \tau_\mathrm{s} s}\right] = a_0[1 - \exp(-2t/\tau_\mathrm{s})]. \tag{4.41}$$

We consider the transient response of the transmitted beam to the modulated input beam, especially for the case of a step function. The input field is expressed as

$$E_\mathrm{in}(t) = \begin{cases} E_0 e^{i\omega_0 t} & t < 0, \\ (E_0 - \xi) e^{i\omega_0 t} & 0 \leq t. \end{cases} \tag{4.42}$$

The transmitted field becomes

$$E_\mathrm{t}(t) = \begin{cases} g E_0 e^{i\omega_0 t} & t < 0, \\ g\left\{E_0 - \xi[1 - \exp(-t/\tau_\mathrm{s})]\right\} e^{i\omega_0 t} & 0 \leq t, \end{cases} \tag{4.43}$$

Thus the transient of transmitted laser power can be expressed as

$$P_\mathrm{t} = G P_\mathrm{in} \exp(-2t/\tau_\mathrm{s}). \tag{4.44}$$

Therefore, the transmitted beam decays with time as expressed as Eq. 4.44 when the input beam is interrupted by the AOM.

4.9 Cavity Enhanced Ellipsometry (P-S Splitting)

As the impinging beam on the folding mirror has a given incident angle, there is a difference in resonance frequency between the P-polarization and S-polarization. We call such a frequency difference a P-S splitting in this thesis. This frequency shift carries information of coatings on the folding mirror and can characterize the coating properties.

In this section, we describe the principle of the P-S splitting measurement. This measurement can be regarded as a type of cavity enhanced ellipsometry.

4.9.1 Characteristic Matrix

A characteristic matrix is a useful tool to calculate the reflectance or transmittance of a multilayer coating thin films [80]. Here we consider the case such that the total number of layer is N. For the case of i-th layer's material with a complex refractive index N_i and mechanical thickness d_i, the characteristic matrix is expressed as

$$M_i = \begin{pmatrix} \cos\delta_i & i\sin\delta_i/\eta_i \\ i\eta_i \sin\delta_i & \cos\delta_i \end{pmatrix}, \tag{4.45}$$

where $\delta_i = 2\pi N_i d_i/\lambda$ is an optical phase shift induced in i-th layer, and η_i is the effective refractive index of i-th layer which has polarization dependence described as

$$\eta_{i,\mathrm{S}} = N_i \cos\theta_i, \tag{4.46}$$

$$\eta_{i,\mathrm{P}} = \frac{N_i}{\cos\theta_i}. \tag{4.47}$$

Here $\cos\theta_i$ is expressed as

$$\cos\theta_i = \left\{1 - (n_0/n_i)^2 \sin^2\theta_0\right\}^{1/2}, \tag{4.48}$$

where θ_0 is the angle of incidence. The total matrix M_{tot} and its elements m_{ij} are defined as

$$\begin{aligned} M_{\mathrm{coating}} &= M_1 M_2 \cdots M_N \\ &= \prod_{i=1}^{N} M_i = \begin{pmatrix} m_{11} & im_{12} \\ im_{21} & m_{22} \end{pmatrix}, \end{aligned} \tag{4.49}$$

where m_{ij} are the elements of the matrix. Two coefficients B and C are calculated as

$$\begin{pmatrix} B \\ C \end{pmatrix} = \begin{pmatrix} m_{11} & im_{12} \\ im_{21} & m_{22} \end{pmatrix} \begin{pmatrix} 1 \\ \eta_m \end{pmatrix}, \tag{4.50}$$

where η_{m} is the effective refractive index of the substrate material written as

$$\eta_{m,\mathrm{S}} = N_{\mathrm{m}} \cos\theta_i, \tag{4.51}$$

$$\eta_{m,\mathrm{P}} = \frac{N_{\mathrm{m}}}{\cos\theta_i}, \tag{4.52}$$

where N_{m} is the refractive index of the substrate material. Eq. 4.50 gives the Fresnel coefficient of the coatings as

$$\rho = \frac{n_0 B - C}{n_0 B + C}, \tag{4.53}$$

where n_0 is the refractive index of vacuum. Thus, one can calculate the reflectance of the coatings by using $R = |\rho|^2$.

Not only the reflectance, but also the phase shift induced by the coatings can be calculated from the characteristic matrix. The phase of the reflected light can be computed by

$$\Delta\phi_{\mathrm{S,P}} = \arctan\left(\frac{2\eta_0(\eta_{\mathrm{m}}^2 m_{12}m_{22} - m_{11}m_{21})}{\eta_0^2 m_{11}^2 - \eta_{\mathrm{m}}^2 m_{22}^2 + \eta_0^2\eta_{\mathrm{m}}^2 m_{12}^2 - m_{21}^2}\right)_{\mathrm{S,P}}, \tag{4.54}$$

where subscript S and P represent the polarization. As the phase is slightly different between the two polarization, we can define the phase difference as

$$\Delta\phi \equiv \Delta\phi_{\mathrm{S}} - \Delta\phi_{\mathrm{P}}. \tag{4.55}$$

When the angle of incidence is 0 deg, η is same for both polarization. Therefore, the phase difference does not exist as long as the beam is injected vertically.

When a CML is formed on a mirror surface, the characteristic matrix of the mirror is modified as

$$M_{\mathrm{mod}} = M_{\mathrm{CML}} M_{\mathrm{coating}}, \tag{4.56}$$

where M_{CML} is the characteristic matrix of CML. The elements of M_{CML} are defined in the same manner as Eq. 4.45. CML formation on a mirror surface changes the characteristic matrix, hence the phase difference $\Delta\phi$.

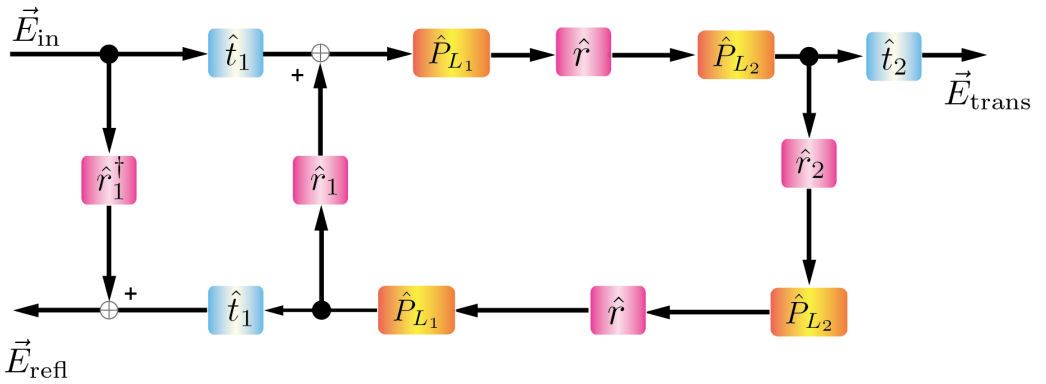

Figure 4.12: Equivalent block diagram of folded cavity to explain the phase shift between P- and S-polarization. Each plant represents the propagator, transmission or reflection matrix.

4.9.2 Frequency Shift

We derive the frequency shift induced by the phase shift in the folding mirror. Here, we calculate the field using an equivalent block diagram shown in Fig. 4.12 [81, 82].

First, we define the vector which denotes the field as

$$\vec{E}_j = \begin{pmatrix} E_{j,\mathrm{S}} \\ E_{j,\mathrm{P}} \end{pmatrix}, \tag{4.57}$$

where j represents the location of the fields, in, cav, or trans. Propagator, transmission, and reflection matrices are defined as

$$\hat{P}_{L_i} = \begin{pmatrix} e^{-ikL_i} & 0 \\ 0 & e^{-ikL_i} \end{pmatrix}, \tag{4.58}$$

$$\hat{t}_i = \begin{pmatrix} t_i & 0 \\ 0 & t_i \end{pmatrix}, \tag{4.59}$$

$$\hat{r}_i = \begin{pmatrix} r_i & 0 \\ 0 & r_i \end{pmatrix}, \tag{4.60}$$

$$\hat{r} = \begin{pmatrix} r & 0 \\ 0 & re^{-i\Delta\phi} \end{pmatrix}, \tag{4.61}$$

where $i = 1, 2$. It should be noted that the phase shift is introduced in the reflection matrix of folding mirror as $e^{-i\Delta\phi}$.

From Fig. 4.12, the intra-cavity field is written as

$$\vec{E}_{\rm cav} = t_1 \left(I - r_1^2 r^2 \hat{P}_{\rm rtp} \right)^{-1} \vec{E}_{\rm in}, \tag{4.62}$$

where I is the identity matrix and $\hat{P}_{\mathrm{rtp}}$ represents the round trip propagator. Solving Eq. 4.62, one can obtain

$$\vec{E}_{\mathrm{cav}} = t_1 \mathrm{diag}\left(1 - r_1^2 r^2 e^{-i\Phi_{\mathrm{rtp}}}, 1 - r_1^2 r^2 e^{-i(\Phi_{\mathrm{rtp}}+2\Delta\phi)}\right) \vec{E}_{\mathrm{in}}, \tag{4.63}$$

where Φ_{rtp} is the round trip phase shift. Using $\vec{E}_{\mathrm{cav}}$, the transmitted field can be expressed as

$$\vec{E}_{\mathrm{trans}} = \hat{t}_2 \hat{P}_{L_2} \hat{r} \hat{P}_{L_1} \vec{E}_{\mathrm{cav}}, \tag{4.64}$$

$$= t_2 r \mathrm{diag}\left(e^{-i\Phi_{\mathrm{rtp}}/2}, e^{-i(\Phi_{\mathrm{rtp}}/2+\Delta\phi)}\right) \vec{E}_{\mathrm{cav}}. \tag{4.65}$$

The matrices introduced here are diagonalized, and one can obtain the field by simple math. Computing each element, the transmitted field can be written as

$$E_{\mathrm{trans,S}} = \frac{t_1^2 r e^{-i\Phi_{\mathrm{rtp}}/2}}{1 - r_1^2 r^2 e^{-i\Phi_{\mathrm{rtp}}}} E_{\mathrm{in,S}}, \tag{4.66}$$

$$E_{\mathrm{trans,S}} = \frac{t_1^2 r e^{-i(\Phi_{\mathrm{rtp}}/2+\Delta\phi)}}{1 - r_1^2 r^2 e^{-i(\Phi_{\mathrm{rtp}}+2\Delta\phi)}} E_{\mathrm{in,P}}. \tag{4.67}$$

Therefore, each transmitted power normalized by the incident power is expressed as

$$\frac{P_{\mathrm{trans,S}}}{P_{\mathrm{in,S}}} = \frac{T_1^2 R}{(1 - R_1 R)^2 + 4 R_1 R \sin^2\left(\frac{\Phi_{\mathrm{rtp}}}{2}\right)}, \tag{4.68}$$

$$\frac{P_{\mathrm{trans,P}}}{P_{\mathrm{in,P}}} = \frac{T_1^2 R}{(1 - R_1 R)^2 + 4 R_1 R \sin^2\left(\frac{\Phi_{\mathrm{rtp}}+2\Delta\phi}{2}\right)}, \tag{4.69}$$

These equations show that there exists a difference in resonance frequency between S- and P-polarization.

We derive the amount of resonant frequency shift induced by $\Delta\phi$ phase shift in folding mirror. The round trip phase shift of S-polarized beam becomes

$$\phi_{\mathrm{rtp}} = \frac{4\pi\nu L}{c}. \tag{4.70}$$

As shown in above, the resonant peak of P-polarization beam is shifted by $-2\Delta\phi$ compared to that of S-polarization. We define the resonant frequency split between P- and S-polarization as $\Delta\nu$. Then the relation between the round trip phase shift and the resonant frequency split can be written as

$$\phi_{\mathrm{rtp}} - 2\Delta\phi = \frac{4\pi(\nu + \Delta\nu)L}{c}. \tag{4.71}$$

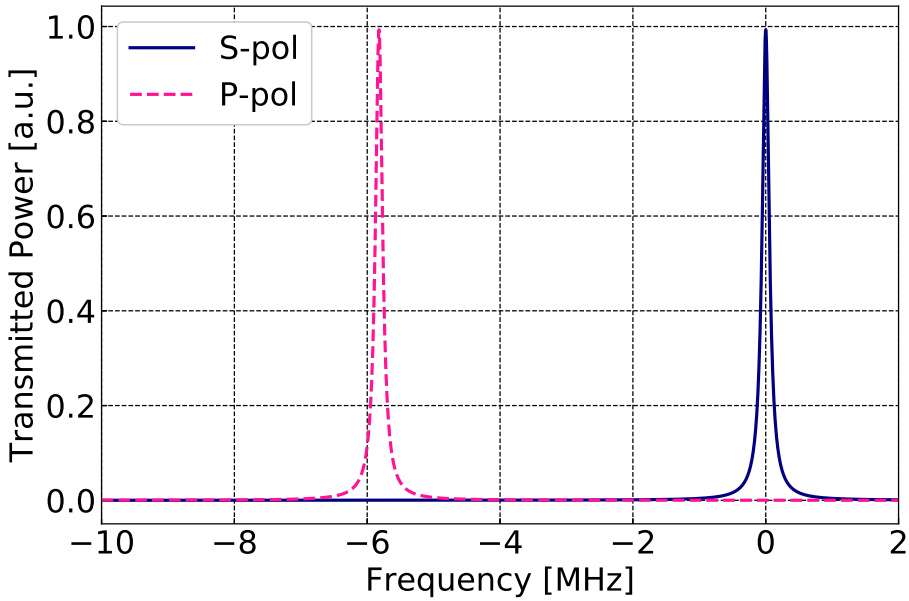

Figure 4.13: Example of the resonant frequency spit between S-polarization (solid line) and P-polarization (dashed line) . Here we assumed $\Delta\phi = 10\,\mathrm{mrad}$ phase shift, $\mathscr{F} \sim 1.5 \times 10^4$, and $L = 82\,\mathrm{mm}$ case.

From Eq. (4.70), one can arrive at

$$\Delta\nu = -\frac{c}{4\pi L} 2\Delta\phi = -\frac{f_{\mathrm{FSR}}}{\pi}\Delta\phi. \tag{4.72}$$

Thus, the resonant frequency shift is induced by the folding mirror. The example is shown in Fig. 4.13.

As the CML formation changes the elements of characteristic matrix of the mirror, it also changes $\Delta\phi$. Therefore, the resonant frequency split $\Delta\nu$ also changes as the CML is formed on the mirror surface. By measuring the change the in resonant frequency split, one can compute the CML thickness.

The amount of resonant frequency split $\Delta\nu$ is determined by the FSR f_{FSR} and the phase shift $\Delta\phi$. The phase shift $\Delta\phi$ depends on the refractive index N_{CML} and the angle of incidence to the folding mirror θ_0. In our setup, the folding angle γ corresponds to the angle of incidence. Thus, the resonant frequency split depends on the FSR, folding angle of the cavity and the refractive index of CML. It should be noted that the contribution of imaginary part of N_{CML} to the phase shift is extremely small. Assuming that the folding angle

$\gamma = 22.5\,\mathrm{deg}$ and $N_{\mathrm{CML}} = 1.2 - 10^4 i$ with 1 nm CML thickness, the imaginary part of N_{CML} generates only $10^{-8}\%$ difference in the frequency split $\Delta\nu$ from the case of $N_{\mathrm{CML}} = 1.2$. Therefore, we ignore the contribution from the imaginary part of CML refractive index in the following discussion.

4.9.3 Errors in CML Thickness Measurement

In this subsection, we introduce the errors which involves in CML thickness estimation. Firstly, resonant width of the folded cavity affects measurement accuracy of the frequency difference between the two-peaks. Here we define the resonant width as the FWHM of the cavity

$$f_{\mathrm{FWHM}} = \frac{f_{\mathrm{FSR}}}{\mathscr{F}}. \tag{4.73}$$

In our setup, the FWHM is calculated as

$$f_{\mathrm{FWHM}} = \frac{1.84\,\mathrm{GHz}}{2.0 \times 10^4} = 0.09\,\mathrm{MHz}. \tag{4.74}$$

In reality, the accuracy of determining the peak frequency can be smaller than the FWHM. However, as an upper bound, we assume that the error introduced by the resonant width to be $\pm 0.09\,\mathrm{MHz}$ in $\Delta\nu$.

Secondly, a systematic error is induced by the CML refractive index value. In the following chapter, we assume the refractive index of CML as $n_{\mathrm{CML}} = 1.19$ which is estimated by the Lorentz-Lorenz equation 3.23. As we employ the estimated value, there is an uncertainty in the CML refractive index, and it introduces a systematic error. The refractive index measured in KAGRA is 1.26 at 1064 nm wavelength [58]. By taking this value into account, we set the uncertainty in the CML refractive index to be ± 0.1.

In addition, statistical error is involved in the measurement. We use a current tuning of the laser to scan the laser frequency. For each scan, we include not only the P- and S-resonant peaks, but also the peaks from the RF sidebands at frequency $\pm 29.1\,\mathrm{MHz}$ used to control the length of the cavity. Because the frequency of the RF sidebands is precisely known, the frequency scanning speed is calibrated on each scan.

However, there may be a fluctuation of the scanning speed within a single scan. This fluctuation of the scanning speed is assumed to be random, thus treated as a statistical error.

4.10 Summary of this chapter

- We developed a cryogenic optical cavity setup with folded configuration. The folded cavity can be cooled down to approximately 10 K.

- A folded cavity enables efficient measurements for characterization of coating performance.
- Ringdown measurement provides an optical attenuation of mirrors.
- A resonant frequency shift is introduced by a folding mirror. Folded configuration enables one to measure such frequency shift.
- By measuring a drift in resonant frequency split, one can measure the CML thickness, which changes the frequency split depending on its thickness.

Chapter 5

Experimental Characterization of Cryogenic Molecular Layers Using a Folded Cavity

In this chapter, we describe the results of experimental characterization of the CML using a cryogenic folded cavity. First, we derive the optical loss in the input and output mirrors using the FP cavity. Then, we install the folded cavity and measure the optical loss in the cavity. By subtracting the optical loss of the input and output mirrors, we estimate the optical loss in the folding mirror at room temperature. At the same time, we measure the P-S resonant frequency split, and confirm the validity of the cavity enhanced ellipsometry.

After that, we cool down the folded cavity, and monitor how the finesse and the resonant frequency split change induced by the CML during the cryogenic operation. Through these measurements at cryogenic temperature, we estimate the optical loss generated by the CML and its thickness.

These measurements at cryogenic temperature are conducted with two different spacers. First measurement involves the folded cavity described in the previous chapter. This measurement is to investigate the validity of the cavity enhanced ellipsometry to characterize the CML. An additional measurement is done with the modified spacer which has a slit to expose the folding mirror to the room-temperature vacuum.

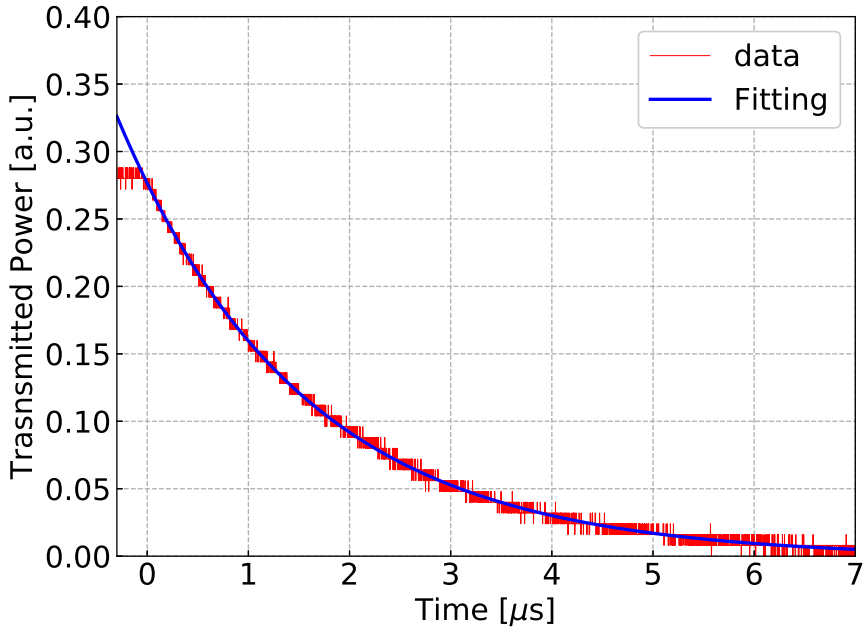

Figure 5.1: Obtained transient response of FP cavity and fitted result. Red and blue lines represent the measured data and fitted curve, respectively.

5.1 Optical Loss Characterization

The optical properties of a mirror satisfy the conservation of energy expressed as

$$R + T + L = R + A = 1, \tag{5.1}$$

where L is the optical loss, and $A \equiv T + L$ is the attenuation which describes the total power lost upon a single reflection. From ringdown measurements, one can evaluate the reflectivity, hence the attenuation.

5.1.1 Finesse of Fused Silica Fabry-Perot Cavity

First, we measure the finesse of the Fabry-Perot cavity with fuese silica mirrors which are used for the input and output mirror in the folded cavity. The mirrors are held with vaccum compatible mirror holders and installed inside the chamber. The cavity length is set as $L = 74\,\mathrm{mm}$ whichis determined by the restriction of the space.

Table 5.1: The parameters of the folded cavity.

Parameters	Value
Cavity length	$L_1 = 41\,\mathrm{mm}$
	$L_2 = 41\,\mathrm{mm}$
	$L = L_1 + L_2 = 82\,\mathrm{mm}$
Free spectral range	1.84 GHz
Beam size on the input/output mirror	280 μm
Beam size on the folding mirror	97 μm
Radius of curvature	50 mm
Folding angle	15 deg

Fig. 5.1 shows the measured ringdown of the FP cavity. Blue line represents the fitted curve. Here we assumed the fitting function as

$$f(t) = a\exp(-t/\tau) + b, \tag{5.2}$$

where τ is the decay time of the cavity, and a and b are the parameters which compensate the gain and dark offset of the PD. The finesse can be calculated using Eq. 4.13. The obtained finesse is 23153 ± 49, which is higher than the designed value of $\sim 1.5 \times 10^4$. The error corresponds to the statistical error. Assuming the same reflectance R_{silica} in each mirror, the attenuation of fused silica mirrors, $A_{\mathrm{silica}} = 1 - R_{\mathrm{silica}}$, can be calculated as

$$A_{\mathrm{silica}} = 135.7 \pm 0.3\,\mathrm{ppm}, \tag{5.3}$$

where

$$R_{\mathrm{silica}} = 0.999864.3 \pm 0.0000003. \tag{5.4}$$

The obtained reflectance is slightly higher than the designed value, resulting in a larger finesse.

5.1.2 Optical Loss in the Folding Mirror

The optical loss in the folding mirror can be measured from the difference in the finesse between the FP and the folded cavities. The measured finesse of the folded cavity at room temperature is about 1.7×10^4. Therefore, the reflectance of the folding mirror can be calculated by

$$\mathscr{F}_{\mathrm{fold}} = \frac{\pi\sqrt{R_1}}{1 - R_1 R}, \tag{5.5}$$

where $R_1 (= R_{\text{silica}})$ is the reflectance of the input and output silica mirrors. Thus the reflectance of the folding mirror can be computed using Eq. 5.5 as

$$R = 0.9999504 \pm 0.0000008. \tag{5.6}$$

Thus, the attenuation of the folding mirror can be estimated as $A_{\text{fold}} = 49.6 \pm 0.8\,\text{ppm}$. As the designed reflectivity was larger than 0.99998, hence less than 20 ppm attenuation, the coatings on the folding mirror has larger optical loss than the designed value.

One possible source of this optical loss is a defect in the coating. When such a defect exists around the center of the mirror where the beam impinges, it introduces optical losses via scattering or absorption [83]. Insufficient polishing of mirror surface also generates optical loss. In order to identify the origin of this optical loss, further investigations are needed.

5.1.3 P-S Splitting

We confirm the validity of the cavity enhanced ellipsometry (CEE) from the measurement at room temperature by comparing the results with the theoretical expectation.

First, we theoretically derive the P-S splitting frequency based on the characteristic matrix. The deposited coating is SiO_2/Ta_2O_5 multilayer coating, and the number doublet is $N = 20$. Optical thickness of each layer is $\lambda/4$ except for the top layer which has $\lambda/2$ thickness, called a $\lambda/2$ cap as shown in Fig. 5.2. The refractive indices are $n_{SiO_2} = 1.44$ and $n_{Ta_2O_5} = 2.2$ at 1550 nm [31]. Assuming these values, the phase shift between P- and S-polarization beams $\Delta\phi$ can be computed as

$$\Delta\phi = -0.0068\,\text{rad}. \tag{5.7}$$

This value is obtained by numerical calculations using characteristic matrices as shown in the previous chapter. Therefore, from Eq. 4.72 the frequency split becomes as

$$\Delta\nu_{\text{P,S}} = 3.95\,\text{MHz}. \tag{5.8}$$

Then, we derive the experimental result of the P-S resonant frequency split. First, we calculate the laser frequency scan efficiency through the current tuning. We inject phase modulated beam into the cavity at 29.1 MHz where laser frequency is scanned with $3\,V_{\text{pp}}$ at 300 Hz triangle wave. As the frequencies of sidebands are shifted by 29.1 MHz, one can derive the scanning efficiency by measuring the shift between the carrier and sidebands. The split time of

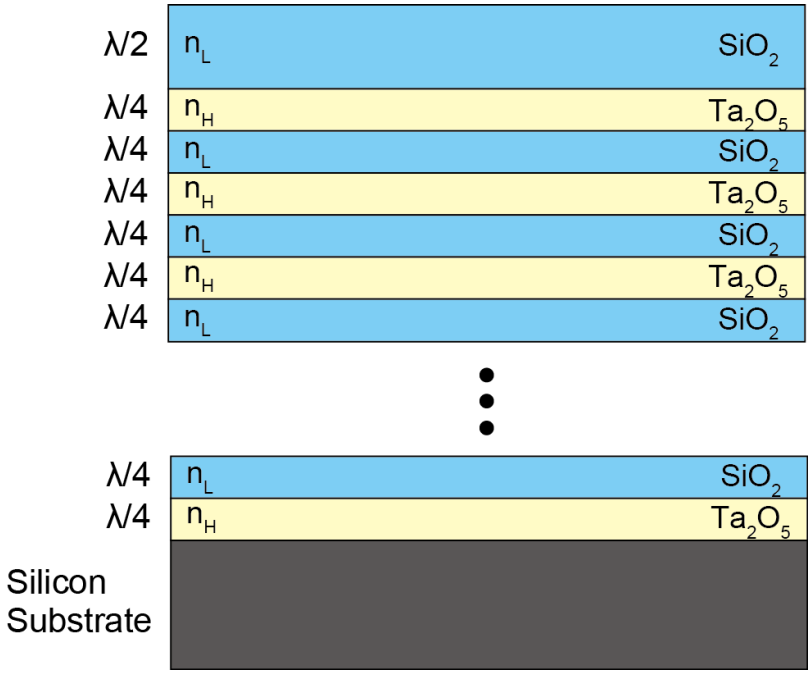

Figure 5.2: An example of dielectric multilayer coatings deposited on a silicon substrate. SiO_2 and Ta_2O_5 layers are deposited alternately with optical thickness of $\lambda/4$ except for the top layer. The top layer has $\lambda/2$ optical thickness which is called $\lambda/2$ cap.

the carrier and the sideband is measured as $450 \pm 2\,\mu$s. Thus, the scanning efficiency is calculated as $35.9 \pm 0.2\,$MHz.

Then, we measure the P-S splitting in the same manner. The measured time difference between P- and S-polarizations are $\Delta = 61.2 \pm 0.4\,\mu$s with $3\,V_{pp}$ at $300\,$Hz triangle wave scan. As the laser frequency scanning efficiency is $35.9 \pm 0.2\,$MHz, the split frequency can be calculated as

$$\Delta\nu = (35.9 \pm 0.2)\,\text{MHz/V} \times 3\,\text{V} \times 300\,\text{Hz} \times 2 \times (61.2 \pm 0.4)\,\mu\text{s}, \tag{5.9}$$

$$= 3.96 \pm 0.03\,\text{MHz}. \tag{5.10}$$

This value is consistent with the theoretical value, $3.95\,$MHz. Therefore, the P-S splitting measurement using the folded cavity can be considered to be valid for characterization of coatings. Combining the ringdown measurement, this device can facilitate the development of low absorption and high reflective coatings for the future GWDs.

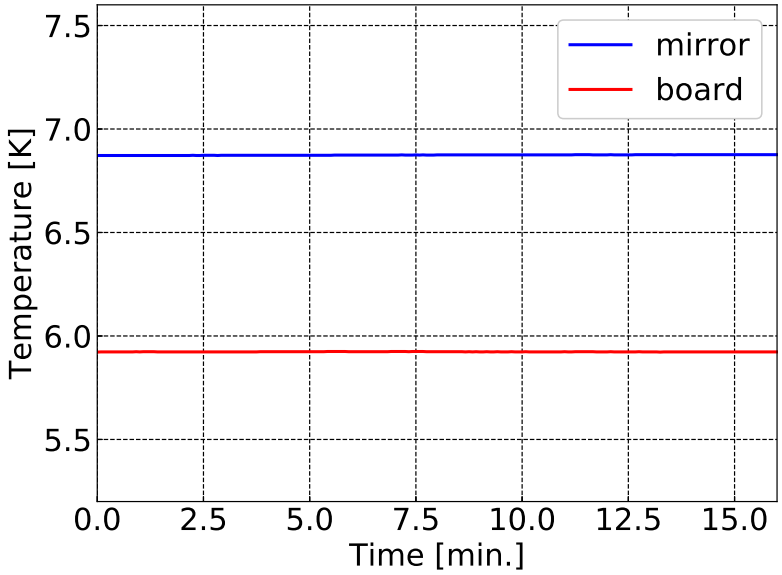

Figure 5.3: The temperature stability during the ringdown measurement. Blue, and red lines represent the temperature of the mirror, and bread board, respectively.

5.2 Optical Loss at Cryogenic Temperature

In order to estimate the impacts of the CML, the finesse at cryogenic temperature was measured followed by the room temperature measurement. First, we conducted the measurements with closed environment, i.e., there were no apertures to room temperature environment except for small through holes for the cables. In this scheme, each mirror was exposed not to room temperature, but to cryogenic environment. Through these measurements at cryogenic temperature, we investigated the validity of the cavity enhanced ellipsometry to estimate the thickness of the CML.

Then, we replace the spacer to the modified one, and perform another set of measurements to characterize the CML. In this additional measurements, the folding mirror is exposed to the room-temperature vacuum to ensure the CML formation on its surface. The details are written in the following section.

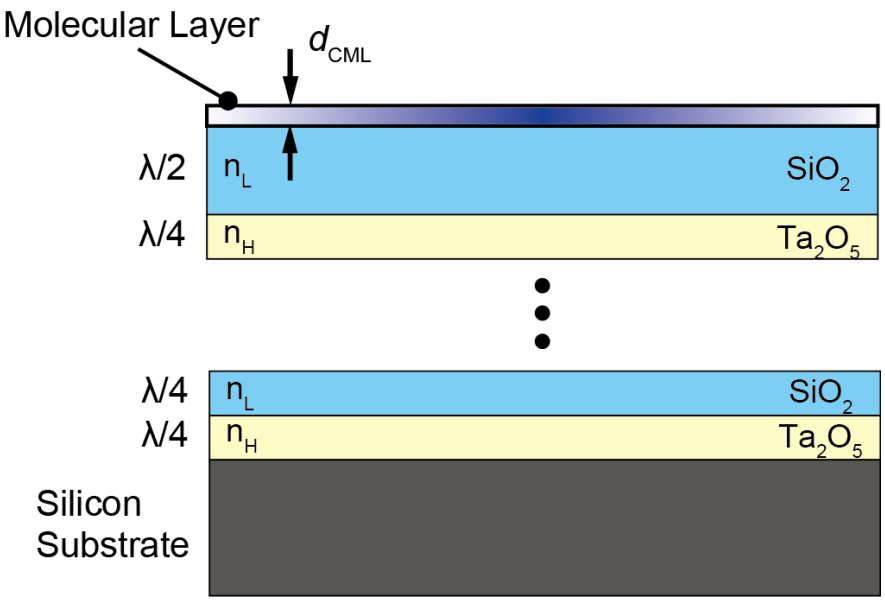

Figure 5.4: Schematic of formed CML on the mirror. The CML can be regarded as a kind of coating layer.

5.2.1 Cavity Length Change

Here we discuss the cavity length change due to the cooling down. The system is cooled down to approximately 7 K. Generally, cooling down the material involves shrinking, which can introduce cavity length change. Here we employ an invar as the spacer which has low thermal expansion coefficient, and the cavity length change is assumed to be less than 100 μm.

In addition, temperature fluctuation at cryogenic temperature is within ± 0.002 K as shown in Fig. 5.3. Therefore, the cavity length change is also negligible during the measurements. Hence the impacts on the finesse measurement due to the cavity length change can be negligible.

5.2.2 Reflectance of the Mirror

Here we discuss how the reflectance of mirror changes due to the molecular layer formation on the top of the coating as shown in Fig. 5.4. Formed CML can be regarded as a coating layer which changes the reflectance of the mirror. The CML, which grows over time, changes the reflectance of the mirror, and the reflectance is calculated using a characteristic matrix [58]. Fig. 5.5 shows the calculated result of the reflectance. When the thickness is comparable to the wavelength, the reflectance oscillates due to the interference of the

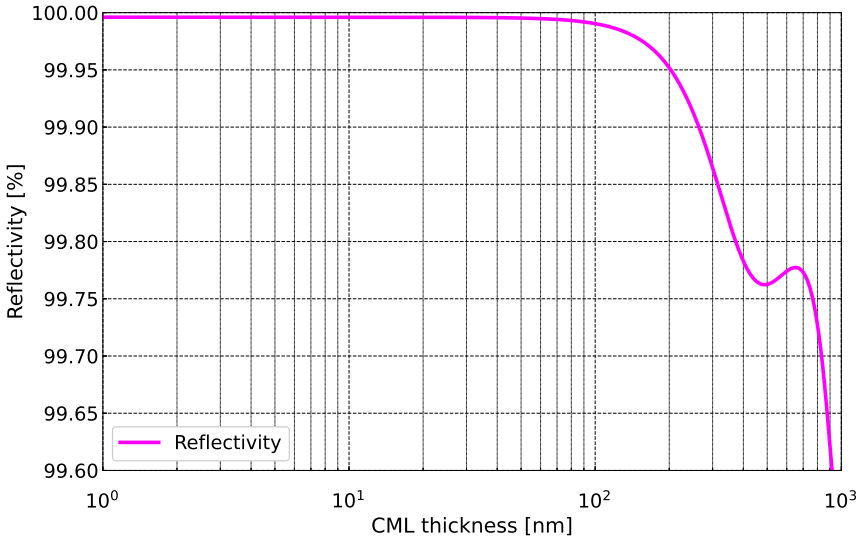

Figure 5.5: How the reflectivity of the mirror changes due to the CML growth. The reflectance can be considered as constant where the thickness of the CML is much thinner than the wavelength. When the thickness of CML becomes comparable to $\lambda/4$, it starts oscillation due to the interference.

reflected field. As long as the thickness is much thinner than the wavelength, the interference can be negligible. Therefore, we assume that the change in reflectance is caused by the optical loss of CML.

5.2.3 Optical Loss Measurements

We monitored the finesse trend for 15 days in order to investigate the optical loss growth rate induced by the CML. To obtain the statistical errors, we performed the ringdown measurements 5 times and calculated the standard deviation. Fig. 5.6 shows the obtained data. Finesse of the cavity monotonically decreased during the cryogenic condition, and recovered after temperature rising. Therefore, it is natural to consider that the optical loss inside the cavity grew with time due to the continuous CML formation.

As discussed in the previous subsection, we assume that the reflectance change is caused by the CML formation as

$$R' = 1 - T - L = R - L, \tag{5.11}$$

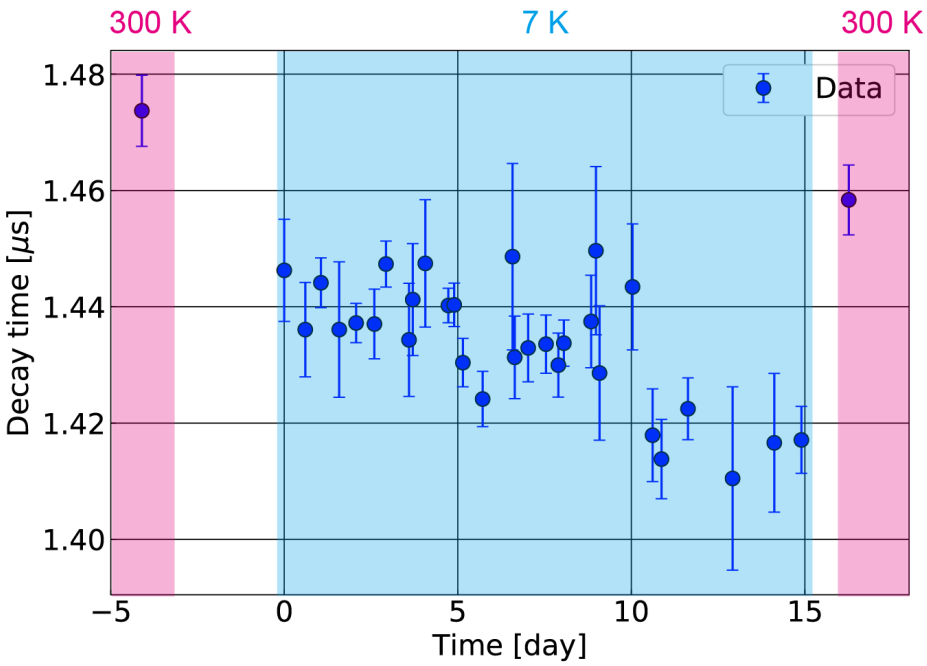

Figure 5.6: The obtained decay time by the ringdown measurement. The finesse was monitored for 15 days at temperature of 7 K. The finesse decreased with time, and recovered after increasing the temperature.

where T is the transmittance and L denotes the optical loss induced by the CML. Therefore, the contaminated amplitude reflectivity is written as

$$r' = \sqrt{R - L}. \tag{5.12}$$

Consequently, the finesse of the folded cavity with additional optical loss can be expressed as

$$\mathscr{F} = \frac{\pi\sqrt{r'^2_1}}{1 - r'^2_1 r'^2} = \frac{\pi\sqrt{R_1 - L}}{1 - (R_1 - L)(R - L)}. \tag{5.13}$$

By monitoring the finesse, one can estimate how the optical loss grows.

In order to estimate the optical loss growth rate, we use the fitting function expressed as

$$\mathscr{F}(t) = \frac{\pi\sqrt{(R_1 - \tilde{L}t - A_0)}}{1 - (R_1 - \tilde{L}t - A_0)(R - \tilde{L}t - A_0)}, \tag{5.14}$$

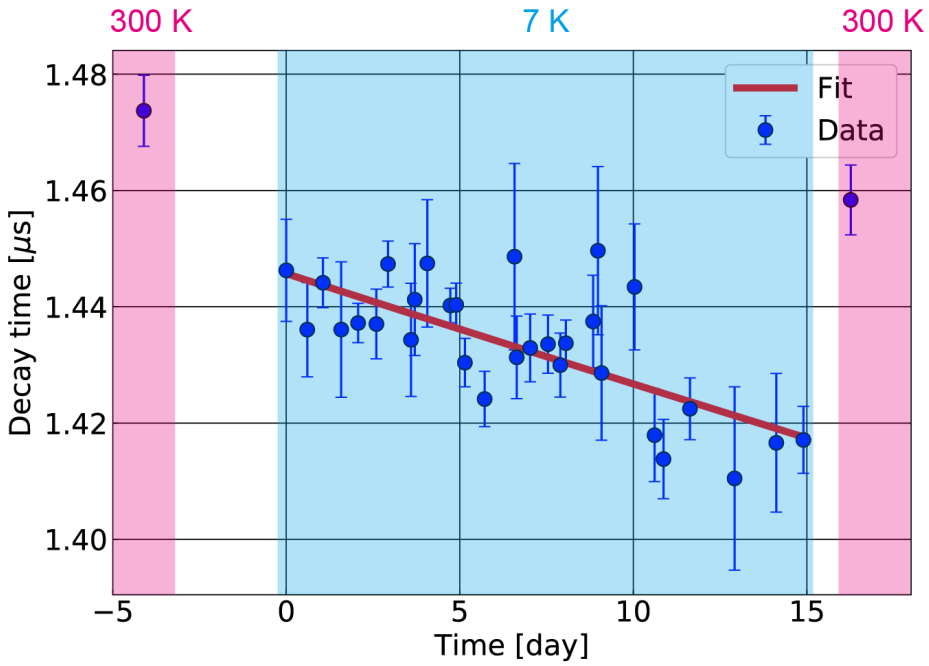

Figure 5.7: The obtained decay time by the ringdown measurement and fitted curve, blue dots and red line, respectively.

where $\tilde{L}$ is the optical loss growth rate and A_0 is the initial optical attenuation which contributes to the slight finesse drop at the beginning of the measurement at cryogenic temperature, and t is the time from the cavity reached 7 K. Here we assume that the reflectivity of each mirror is constant because the formed CML considered to be very thin. We fitted with Eq. 5.14 using the least squares method. Here we used the relation between the finesse and the decay time τ expressed as

$$\tau = \frac{L}{\pi c}\mathscr{F}. \tag{5.15}$$

Fig. 5.7 shows the obtained results and fitted curve. From the fitting, the optical loss growth rate can be estimated as

$$\tilde{L} = 0.13 \pm 0.02\,\mathrm{ppm/day}, \tag{5.16}$$

and the initial optical attenuation is estimated as

$$A_0 = 1.4 \pm 0.1\,\mathrm{ppm}. \tag{5.17}$$

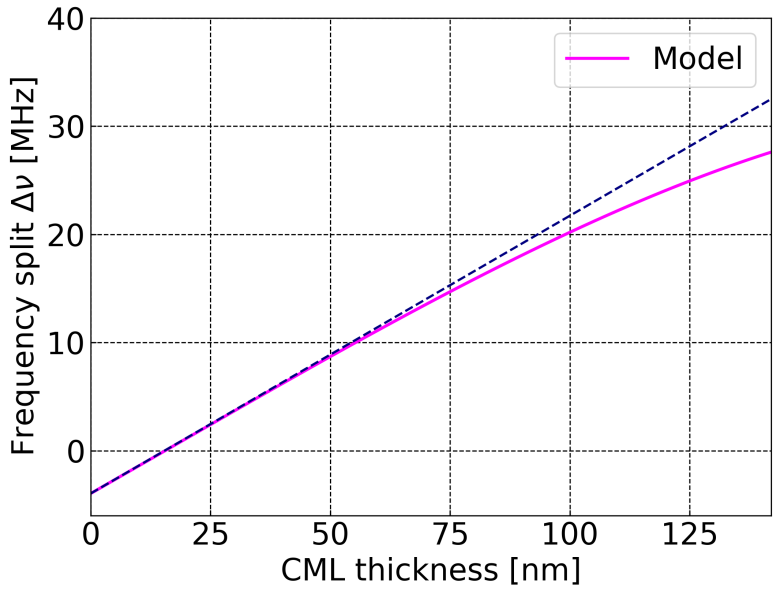

Figure 5.8: How the resonant frequency split changes over the thickness of the CML (solid line), and linearly approximated line (dashed line) when the folding angle is $\gamma = 15\,\mathrm{deg}$.

Besides the optical loss growth rate, we estimated the thickness of the formed CML by cavity enhanced ellipsometry. The initial P-S split is measured as $\Delta = 57.1 \pm 0.7\,\mu\mathrm{s}$. Corresponding frequency split is calculated as

$$\Delta\nu_{\mathrm{int}} = -3.69 \pm 0.05\,\mathrm{MHz}. \tag{5.18}$$

We measured the frequency split after 15 days cryogenic operation. The frequency split at the end of cryogenic operation is measured as $\Delta = 55.6 \pm 0.5$, which corresponds to

$$\Delta\nu_{\mathrm{fin}} = -3.58 \pm 0.04\,\mathrm{MHz}. \tag{5.19}$$

Here we assume that the CML is formed uniformly on each mirror with thickness of d_{CML}. The frequency split changes linearly where the thickness of CML is much thinner than the wavelength as shown in Fig. 5.8. This frequency shift can be approximated as

$$\Delta\nu\,[\mathrm{MHz}] = 0.26\,[\mathrm{MHz/nm}] \times d_{\mathrm{CML}}\,[\mathrm{nm}] - 3.95\,[\mathrm{MHz}]. \tag{5.20}$$

Here we assumed that the refractive index of the CML is $n_{\mathrm{CML}} = 1.19$ which is theoretically derived by the Lorentz-Lorenz equation expressed as Eq. 3.23. From Eqs. 5.18 to 5.20, the optical thickness of CML can be estimated as

$$d_{\mathrm{CML,int}} = 1.0 \pm 0.2\,\mathrm{nm}, \tag{5.21}$$

and

$$d_{\mathrm{CML,fin}} = 1.4 \pm 0.2\,\mathrm{nm}. \tag{5.22}$$

Therefore, the CEE has a possibility to probe very thin CML with a nanometer level. In order to confirm the validity of this method, we performed further measurements with a modified spacer and further considerations of uncertainties.

5.3 Measurements with a Modified Spacer

In order to ensure the CML formation on the mirror, we conducted additional measurements with a modified spacer. The modified spacer has a slit on its side in order to expose the folding mirror to molecular flow from room temperature environment as shown in Fig. 5.9. In this configuration, the molecular flow from room temperature environment hits the folding mirror through the slit, resulting in the CML formation on the folding mirror surface. In other words, the folding mirror corresponds to the cryogenic mirror in a GWD, which is also exposed to the room-temperature vacuum. The input and output mirrors are surrounded by the cryogenic spacer and cover, and conductance to these mirrors are much smaller than that of the folding mirror. Therefore, we assume that the CML is formed only on the folding mirror in this experiment. With this configuration, we did ringdown and P-S splitting measurements to confirm the validity of the methods to characterize the CML.

5.3.1 Geometrical Parameters

Geometric parameters are same as the previous measurement except for the folding angle as shown in Tab. 5.2. The modified spacer has larger folding angle, 22.5 deg in order to expose the folding mirror to the room temperature shield. This angle is determined by the restriction of available size of the material and space of the slit. The setup of input and output optics is same as the previous one. Mirrors for the folded cavity are also same — fused silica mirrors for input and output, and a silicon mirror for the folding mirror.

Fig. 5.10 shows how the frequency split changes with the thickness of the CML. Here, we used the refractive indices of SiO_2 and Ta_2O_5 as $n_{\mathrm{SiO_2}} = 1.44$

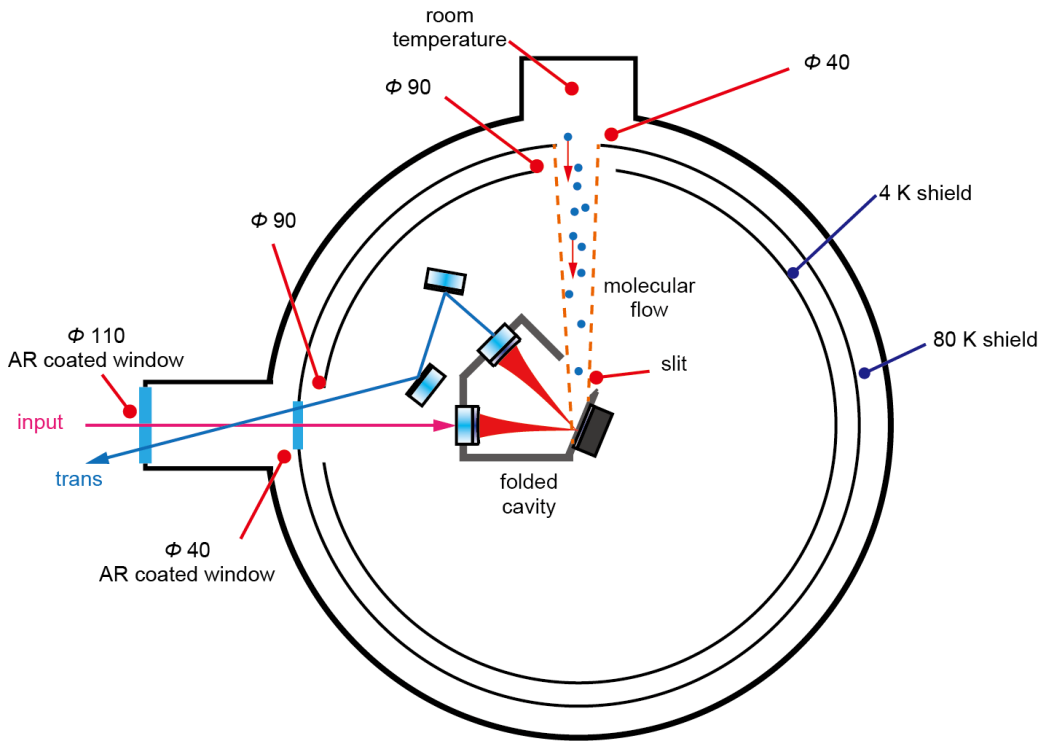

Figure 5.9: Overview of the setup of the additional measurement. The spacer has a slit on its side in order to expose the folding mirror to the room temperature environment, hence the molecular flow. Other two mirrors are not exposed to the room temperature. This configuration enables to form the CML only on the folding mirror as it is exposed to the molecular flow from the room temperature vacuum.

and $n_{\mathrm{Ta_2O_5}} = 2.2$, respectively [31], and the number of $\mathrm{SiO_2/Ta_2O_5}$ pairs are $N = 20$. When the thickness of the CML is much thinner than $\lambda/4$, the frequency split changes linearly with respect to the thickness, and the relation between the frequency split and the thickness of the CML is expressed as

$$\Delta\nu\,[\mathrm{MHz}] = 0.56\,[\mathrm{MHz/nm}] \times d_{\mathrm{CML}}\,[\mathrm{nm}] - 20.28\,[\mathrm{MHz}], \tag{5.23}$$

which is shown in Fig. 5.10 as dashed line. The offset, $-20.28\,\mathrm{MHz}$, is induced by the $\mathrm{SiO_2/Ta_2O_5}$ layers. The measurements at room temperature, i.e., $d_{\mathrm{CML}} = 0$, are consistent with this model. The refractive index of the CML is assumed as $n_{\mathrm{CML}} = 1.19$ in the same manner as the previous measurement.

Table 5.2: The parameters of the modified folded cavity.

Parameters	Value
Cavity length	$L_1 = 41\,\mathrm{mm}$
	$L_2 = 41\,\mathrm{mm}$
	$L = L_1 + L_2 = 82\,\mathrm{mm}$
Free spectral range	1.84 GHz
Beam size on the input/output mirror	280 μm
Beam size on the folding mirror	97 μm
Radius of curvature	50 mm
$R_1 = r_1^2, r_2^2$	0.999864
Folding angle	22.5 deg

5.3.2 Cooling of the Cavity

Fig. 5.11 shows the cooling curve of the folding mirror. It takes about 3 days to reach to 10 K. As the folding mirror is exposed to the room temperature vacuum, the cooling time becomes longer than the closed case. After reaching 10 K, the temperature becomes stable, and the temperature fluctuation during each measurement is less than 0.01 K. Though the temperature fluctuation becomes larger than that of closed case, it is still stable enough so that one can ignore the impacts of cavity length fluctuation on the measurements.

5.3.3 Finesse and P-S Splitting Measurements

We monitored the finesse degradation and the drift of the resonant frequency split for $\sim$ 10 days by the ringdown and the CEE measurements. The cavity ringdown was measured with S-polarization beam. Fig. 5.12 shows the results of these measurements. The decay time monotonically decreases during the cryogenic operation period, and recovers after raising the temperature. The drift in the resonant frequency split also changes over time at cryogenic temperature, and recovers after raising temperature. Therefore, these changes in the finesse and the resonant frequency split are considered to be induced by the formation of the CML. The error bars represent the statistical errors and measurement errors induced by the resonant width. To obtain the statistical errors, we performed the CEE measurements 10 times and calculated the standard deviation. The uncertainty caused by the resonant width is assumed to be ± 0.09 MHz. This causes the error in the CML refractive index as $(\pm 0.09\,\mathrm{MHz})/(0.56\,\mathrm{MHz/nm}) = \pm 0.16\,\mathrm{nm}$.

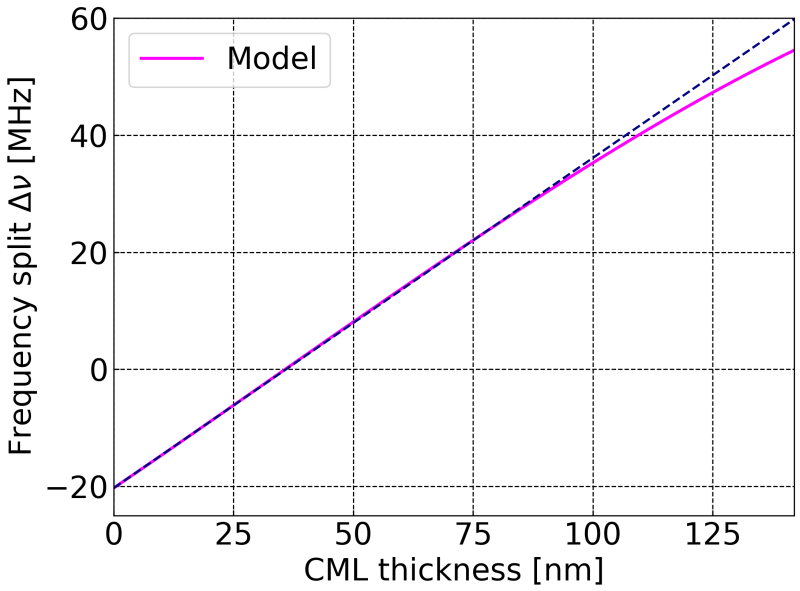

Figure 5.10: How the resonant frequency split changes over the thickness of the CML (solid line), and linearly approximated line (dashed line) when the folding angle is $\gamma = 22.5\,\mathrm{deg}$.

5.3.4 Optical Loss and Thickness

As the only folding mirror is exposed to the room temperature vacuum, the finesse of the modified cavity is written as

$$\mathscr{F}(t) = \frac{\pi\sqrt{R_1}}{1 - R_1(R - L_{\mathrm{CML}})}, \tag{5.24}$$

where L_{CML} is the optical loss on the folding mirror by the CML. At room temperature, the optical loss of the CML is equal to zero, and one can estimate R. From the obtained results at cryogenic temperature, the optical loss of the CML can be estimated.

In order to obtain L_{CML}, we calculated the attenuation A of the folding mirror from the result taken at room temperature in advance of the cryogenic measurement. The attenuation, A, was calculated as $A = 4.7 \pm 0.7\,\mathrm{ppm}$, hence $R = 0.999995.3 \pm 0.7$. The optical attenuation is much smaller than the previous measurement.

The uncertainty in the refractive index of the CML introduces an error in the calculated CML thickness. We assume the CML refractive index to be

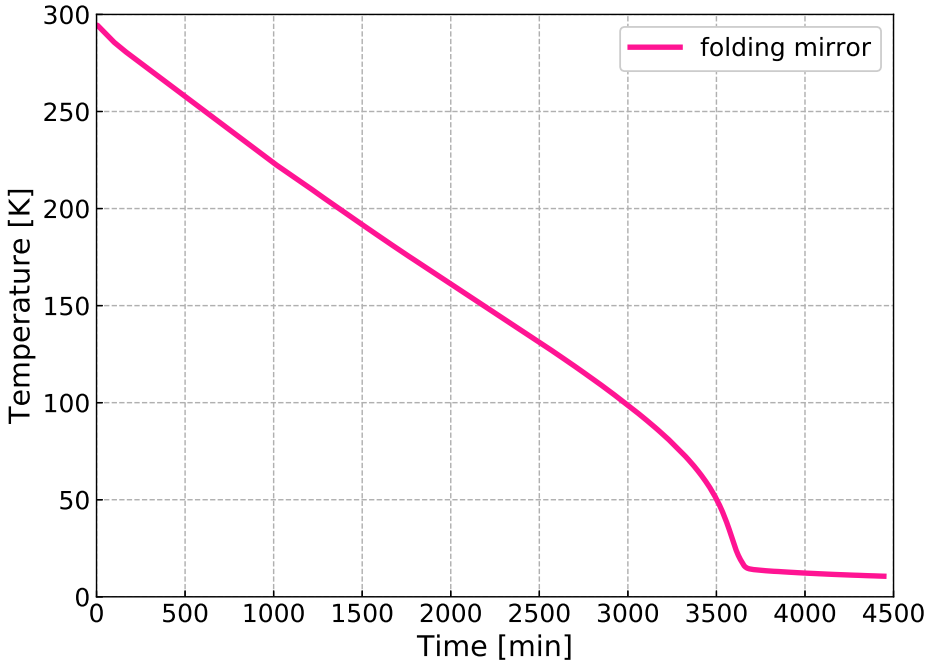

Figure 5.11: Cooling curve of the folding mirror.

$n_{\mathrm{CML}} = 1.19 \pm 0.1$. When the refractive index of the CML is $n_{\mathrm{CML}} = 1.29$, the relation between the frequency split and the thickness of the CML is expressed as

$$\Delta\nu\,[\mathrm{MHz}] = 0.57\,[\mathrm{MHz/nm}] \times d_{\mathrm{CML}}\,[\mathrm{nm}] - 20.28\,[\mathrm{MHz}]. \tag{5.25}$$

Also, the relation becomes

$$\Delta\nu\,[\mathrm{MHz}] = 0.55\,[\mathrm{MHz/nm}] \times d_{\mathrm{CML}}\,[\mathrm{nm}] - 20.28\,[\mathrm{MHz}], \tag{5.26}$$

for $n_{\mathrm{CML}} = 1.09$. Therefore, we consider that the uncertainty in the CML refractive index induces the error in the sensitivity as $(0.56 \pm 0.01)\,\mathrm{MHz/nm}$. The uncertainty in the CML thickness due to this error depends on the amount of PS split frequency. In this measurement, it becomes maximum when $\Delta\nu$ is minimum, and can be calculated as

$$\frac{(20.28 - 17.95)\,\mathrm{MHz}}{(0.56 \pm 0.01)\,\mathrm{MHz/nm}} = (4.13 \pm 0.08)\,\mathrm{nm}. \tag{5.27}$$

Therefore, the errors induced by the CML refractive index is $\pm 0.08\,\mathrm{nm}$ at most, which is smaller than the errors due to the resonant width. We calculated this error for each measurement.

From the measurements, we estimated the optical loss by the CML, L_{CML} by using Eq. 5.24, and thickness of the CML, d_{CML}, by using Eq. 5.23. Fig. 5.13 shows the growing optical loss L_{CML}, and thickness of the CML d_{CML}. The error bars in CML thickness include the statistical errors, measurement errors induced by the resonant width and systematic errors due to the CML refractive index.

The loss, $7.3 \pm 1.1\,\mathrm{ppm}$, and thickness $2.38 \pm 0.27\,\mathrm{nm}$, measured at the first day are generated by the adsorption during the initial cooling down. In the following 10 days, the optical loss and the thickness of the CML grow over time, and become $L_{\mathrm{CML}} = 17.4 \pm 1.3\,\mathrm{ppm}$ and $d_{\mathrm{CML}} = 4.13 \pm 0.36\,\mathrm{nm}$. After raising the temperature, the optical loss and the thickness of the CML became zero. Therefore, a thin CML is formed on the folding mirror, and it can be probed by not only the ringdown, but also the CEE measurement.

The uncertainty in the estimation of the CML thickness is introduced by the statistical error, measurement error related to the resonant width and systematic error due to the CML refractive index. Taking these into consideration, the uncertainty of the CML thickness is $(\pm 0.38 \pm 0.16 \pm 0.07)\,\mathrm{nm} = \pm 0.42\,\mathrm{nm}$ at most and less than 0.5 nm. Therefore, our setup enables us to measure the CML thickness at a nanometer level. Further considerations on a design of the setup will enable more precise characterization of the CML.

It should be noted that the folding angle of the cavity is considered to be constant through these measurements. Due to the cooling, the folded cavity shrinks, which can lead to the deformation. Here, we ignore the impacts of the deformation due to the cooling by assuming that the spacer shrinks uniformly, and the change in the folding angle is negligible. Especially, during 10 days cryogenic operation at 10 K, the deformation of the spacer is much small as the thermal expansion coefficient is less than approximately $10^{-6}\,1/\mathrm{K}$, and the temperature drift is less than 1 K. Therefore, the relative change in the resonant frequency split is not induced by the deformation of the cavity during the measurements at cryogenic temperature.

5.4 Summary of This Chapter

- We have developed the cryogenic folded cavity, which is the first time ever.

- The optical attenuation of silicon mirror was measured by using the

folded cavity.

- The frequency shift between P- and S-polarization reflects the information of the coatings. By measuring the frequency shift, one can estimate the status of mirror surface.
- We monitored the finesse during the cryogenic environment and it showed finesse degradation due to the CML growth, and drift in the resonant frequency shift.
- In order to confirm the validity of the CEE, the additional measurement was conducted with modified spacer. The results indicate the CML formation on the folding mirror surface, and the CEE can probe the CML at a nanometer level.

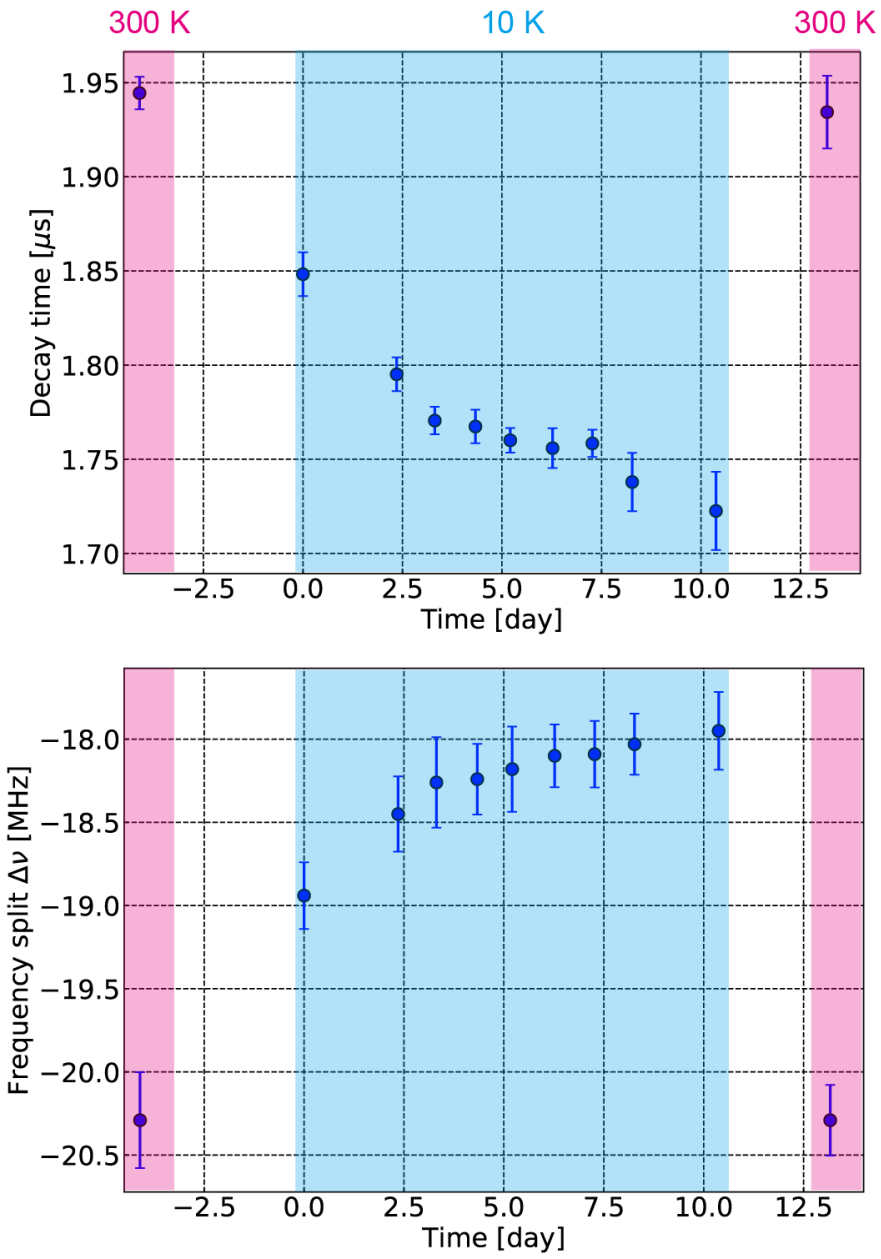

Figure 5.12: Trend of measured decay time (upper) and the resonant frequency split (lower).

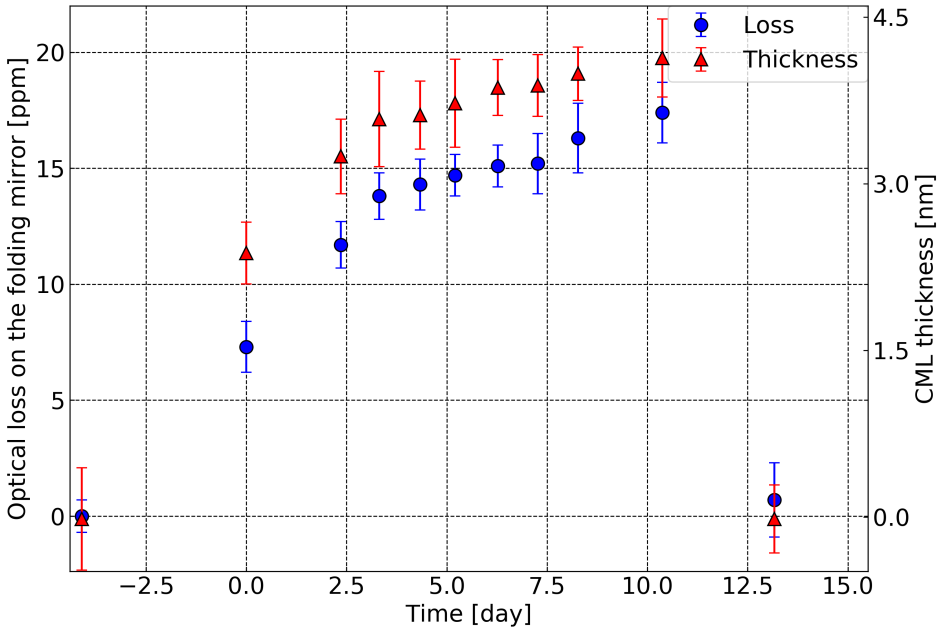

Figure 5.13: Trend of accumulated optical loss on the folding mirror, L_{CML} (blue circle), and CML thickness, d_{CML} (red triangle).

Chapter 6

Discussions and Implications

Cryogenic operation of a GWD is a promising way to improve the sensitivity of a detector by reducing the thermal noise. A cryogenic mirror, however, has a technical problem caused by the adsorption of residual gas molecules. We have presented the possible impacts of the CML on the optical losses introduced for the case of cryogenic GWDs in chapter 3. The effect of scattering loss can be negligible as long as the thickness of the CML is less than 1 μm. On the other hand, the optical absorption becomes a critical problem for cryogenic operation because of an additional heat load to the cryogenic system. Even though the thickness of CML is about 1 nm, the absorbed heat exceeds the cooling capacity for both ET and LIGO Voyager.

In order to investigate the properties of very thin CML, we have developed a cryogenic folded cavity and ellipsometric measurement. The obtained results indicate that the ellipsometric measurement can probe the thickness of the CML with a certain accuracy.

In this chapter, we estimate the heat input to the test mass based on the experimental results. Also, we compute the CML formation rate by using a Monte Carlo (MC) simulation. Finally, we discuss the possible countermeasures for the CML.

6.1 Heat Input due to the CML

In this section, we discuss the heat input induced by the CML based on the experimental results. As the laser wavelength of the experiment is 1550 nm, we focus on the case of the ET.

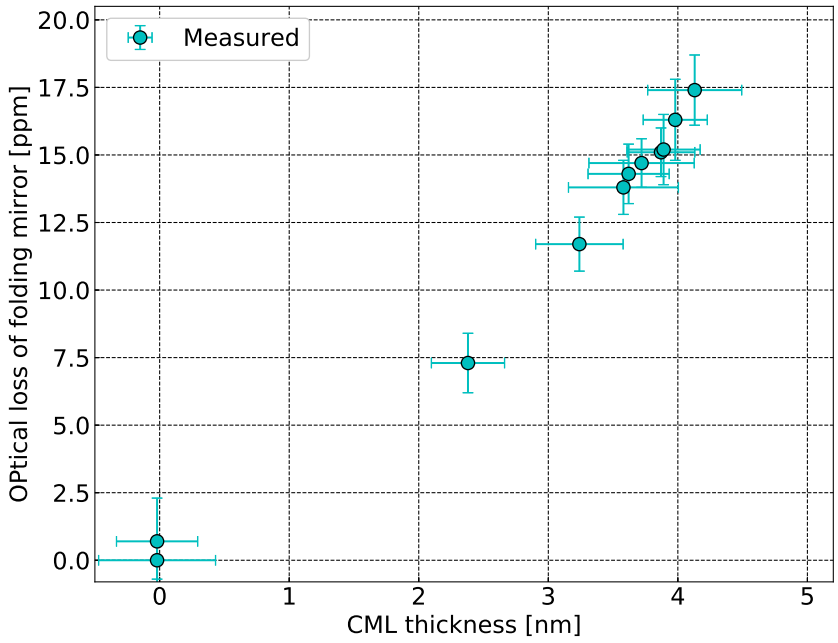

Figure 6.1: The CML thickness and the optical loss of the folding mirror.

6.1.1 Optical Loss and Thickness of the CML

Fig. 6.1 shows the optical loss and thickness of the CML. The optical loss of the CML increases as it becomes thicker. In this subsection, we investigate the validity of the Lambert-Beer law at very thin region from the obtained results. As shown in Chapter 3, the optical loss generated by the scattering can be negligible as long as the thickness of the CML is very thin. We assume that the obtained results of the optical loss is induced by the optical absorption of the CML.

Assuming the Lambert-Beer law, the heat input to the test mass induced by the CML, Q_{CML}, is expressed as

$$Q_{\mathrm{CML}} = P_{\mathrm{CML}}\{1 - \exp(-2\alpha_{\mathrm{CML}} d_{\mathrm{CML}})\}, \tag{6.1}$$

where P_{CML} is the laser power incoming to the CML, α_{CML} is the absorption coefficient, and d_{CML} is the thickness of the CML. Therefore, the optical loss due to the absorption of the CML, L_{CML}, is written as

$$L_{\mathrm{CML}} = Q_{\mathrm{CML}}/P_{\mathrm{CML}} = 1 - \exp(-2\alpha_{\mathrm{CML}} d_{\mathrm{CML}}). \tag{6.2}$$

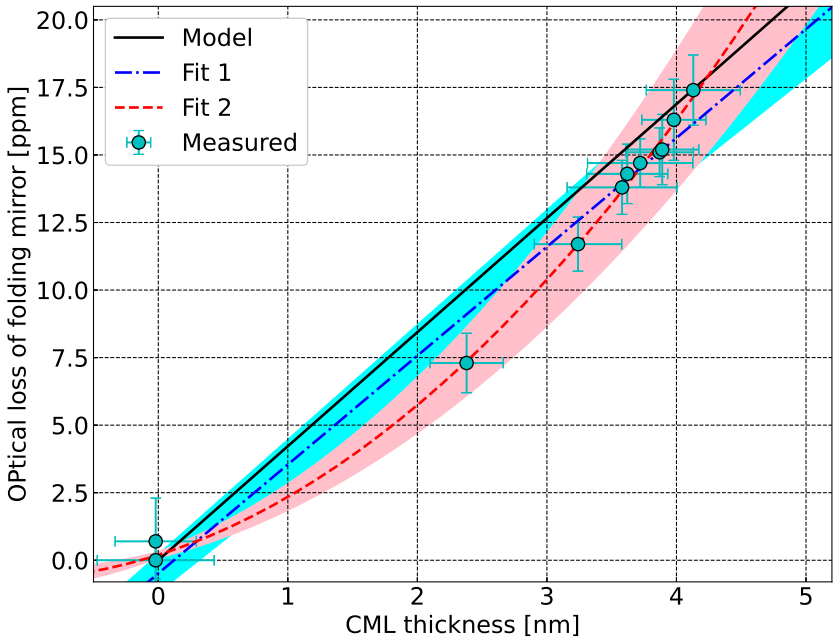

Figure 6.2: The thickness and the optical loss of the CML. Red dashed line and blue dashdot line represent the fitted curves. The shaded bands indicate the 1σ uncertainty. Black solid line is the amorphous ice model.

Assuming that the CML is very thin, Eq. (6.2) is approximated as

$$L_{\mathrm{CML}} \approx 2\alpha_{\mathrm{CML}} d_{\mathrm{CML}}. \tag{6.3}$$

Therefore, the optical absorption scales linearly to the absorption coefficient at very thin region.

Fig. 6.2 shows the obtained results, amorphous ice model, and the fitted curves. We assume the following function as a fitting curve labeled Fit1 to estimate the absorption coefficient,

$$L_{\mathrm{CML}} = \frac{2\alpha_{\mathrm{CML}} d_{\mathrm{CML}}}{\cos\gamma'} + \alpha_0. \tag{6.4}$$

Here, $d_{\mathrm{CML}}/\cos\gamma'$ is the effective path length because of the folding angle γ.

Table 6.1: Results of fitting.

	Fit 1	Fit 2
α_0	$-0.49 \pm 0.74\,\mathrm{ppm}$	$0.20 \pm 0.14\,\mathrm{ppm}$
α_1	$1.91 \pm 0.10\,\mathrm{ppm/nm}$	$0.72 \pm 0.14\,\mathrm{ppm/nm}$
α_2		$0.14 \pm 0.02\,\mathrm{ppm/nm^2}$

The angle of incidence, γ', is calculated by Snell's law as

$$\cos\gamma' = \sqrt{1 - \left(\frac{n_0}{n_{\mathrm{CML}}}\right)^2 \sin^2\gamma}, \tag{6.5}$$

where $n_0 = 1.0$, and $n_{\mathrm{CML}} = 1.19$ are the refractive indices of the vacuum and the CML, respectively. The red dashed line labeled Fit1 shown in Fig. 6.2 represents the results of the fitting assuming Eq. 6.5, and shaded band represents the 1σ uncertainty. The obtained parameters from the fitting are $\alpha_{\mathrm{CML}} = 1.91 \pm 0.10\,\mathrm{ppm/nm}$ and $\alpha_0 = -0.49 \pm 0.74\,\mathrm{ppm}$. A discrepancy from the fitted line can be seen at both thin and thick ends of the measurements, i.e., a discrepancy from the Lambert-Beer linear model.

Here, we fitted the data by another model, which is expressed as

$$L_{\mathrm{CML}} = \alpha_2 \left(\frac{2d_{\mathrm{CML}}}{\cos\gamma'}\right)^2 + \alpha_1 \frac{2d_{\mathrm{CML}}}{\cos\gamma'} + \alpha_0, \tag{6.6}$$

where $\alpha_i\,(i = 0, 1, 2)$ are fitting parameters. Red dashed line labeled Fit2 is the fitting curve by assuming Eq. 6.6. The obtained parameters are $\alpha_2 = 0.14 \pm 0.02\,\mathrm{ppm/nm^2}$, $\alpha_1 = 0.72 \pm 0.14\,\mathrm{ppm/nm}$ and $\alpha_0 = 0.20 \pm 0.14\,\mathrm{ppm}$. By assuming the non-Lambert-Beer model Eq. 6.6, the fitted curve well matches with the measured data.

A possible explanation is that the Lambert-Beer law does not hold in very thin region and the optical loss at very thin region may be proportional to the second order of d_{CML}. Recent simulation study by LIGO Voyager group indicates that the optical absorption by a CML can deviate from the Lambert-Beer law and becomes two orders of magnitude smaller than the Lambert-Beer law below 10 nm, i.e., the order of sub-ppm [84]. Further investigations are needed to know the behavior of the optical loss for very thin layers, and will be of importance for the future GWDs, in which the heat input due to the CML to the test mass becomes the problem even at a few nanometer thickness.

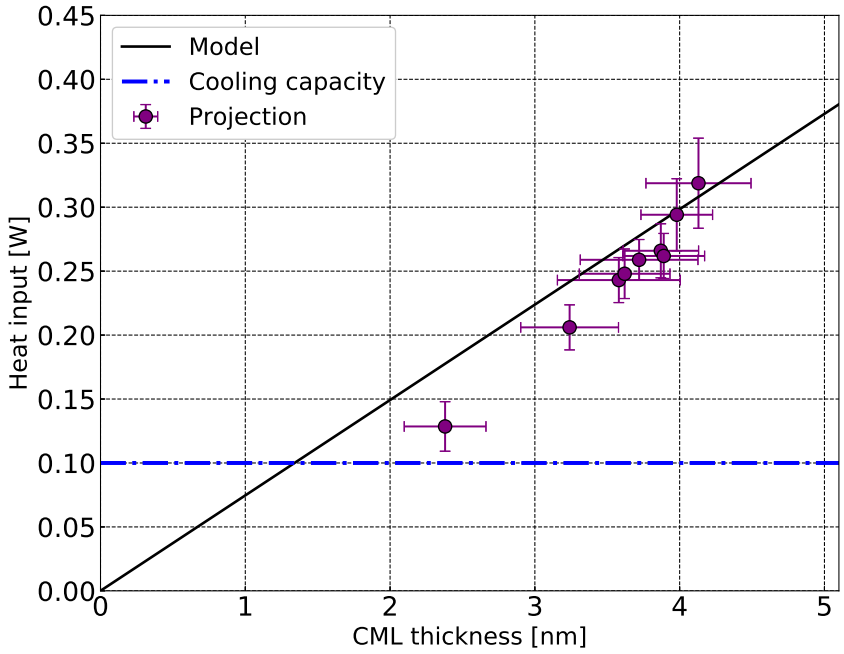

Figure 6.3: Heat input to the test mass induced by the CML for the case of the ET. Solid line shows the theoretical expectation, and blue dashed-dotted line represents the cooling capacity of the test mass mirror in the ET. Purple circles are projections of the measured data.

6.1.2 Heat Input to the Test Mass by the CML

Fig. 6.3 shows the heat input to the test mass for the case of the ET. We project the obtained results shown as purple circles by assuming that the measured optical loss is induced by absorption. The intra-arm-cavity power of the ET is calculated based on the parameters shown in Table 3.2, and constant as long as the thickness of the CML is very thin ($< 10\,\mathrm{nm}$). Black solid line represents the theoretical prediction calculated in chapter 3, and blue dash-dotted line represents the cooling capacity of the ET. The heat input of expected from the measurement shows smaller value than that of the theoretical expectation. This might be because that the Lambert-Beer law does not hold at such small thickness. However, the experimental results indicate that the heat absorption can still be large, and the heat input exceeds the cooling capacity of the mirror, $\sim 100\,\mathrm{mW}$, even if the thickness is approximately 2 nm. Thus, this experiment

indicates that the CML on the test mass mirror can prevent the cryogenic operation of future cryogenic GWDs due to its large heat absorption.

Here, we assumed that the optical loss is induced by the optical absorption. In order to confirm the validity of this assumption, further studies are needed such as the photothermal self-phase modulation technique [47]. Also, further investigations on both thinner and thicker regions are required to fully understand the properties of the CML including the refractive index.

6.1.3 Other Heat Loads

Not only the absorption of the laser power by the CML, but also the radiation from the room temperature environment and the absorption by the coatings contribute to the heat input.

For the case of the ET, heat load induced by the radiation from the room temperature environment is estimated to be approximately 70 mW. In addition, the absorption by the coatings generates approximately 20 mW heat load. On the other hand, the cooling capacity is 100 mW. Therefore, the tolerable heat input by the CML is only 10 mW. Assuming the Lambert-Beer law, the tolerable CML thickness becomes approximately 0.2 nm.

In LIGO Voyager, whose cooling capacity is 10 W, the heat load induced by the absorption in coatings is estimated as 3 W [35]. The heat load due to the radiation is reduced to only 6 mW thanks to the presence of the cryotrap. Thus, the tolerable heat load by the CML is less than 7 W. As the intra-cavity power becomes 3 MW, a few ppm absorption causes larger heat input than the tolerable value. In the same manner as the case of the ET, the tolerable CML thickness become less than 0.1 nm by assuming the Lambert-Beer law.

6.2 Sensitivity of CEE

In this section, we discuss the sensitivity of CEE to CML thickness. Here we define the sensitivity of CEE as

$$\zeta\,[\mathrm{MHz/nm}] = \frac{\Delta\nu\,[\mathrm{MHz}]}{d_{\mathrm{CML}}\,[\mathrm{nm}]}. \tag{6.7}$$

Assuming that the refractivie index of CML is constant, the sensitivity ζ is determined by the geometrical parameters — folding angle γ and FSR f_{FSR} of the folded cavity. Red curves in Figs. 6.4 and 6.5 show how the sensitivity changes over the folding angle and FSR, respectively. Blue curves in Figs. 6.4 and 6.5 represent the amount of P-S split frequency $\Delta\nu$ without CML. In

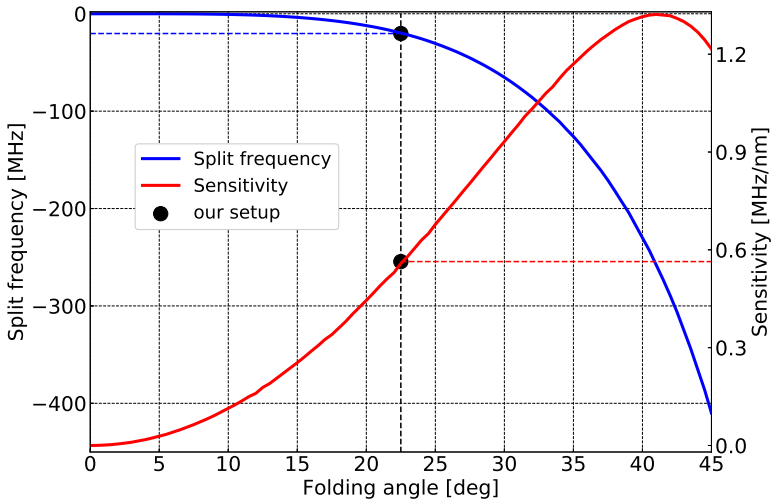

Figure 6.4: How splitting frequency and sensitivity of CEE change over the folding angle. $f_{\mathrm{FSR}} = 1.84\,\mathrm{GHz}$ is assumed. Black dots correspond to our setup.

our setup, the folding angle and FSR are set to $\gamma = 22.5\,\mathrm{deg}$ and $1.84\,\mathrm{GHz}$, respectively, and the sensitivity becomes $\zeta = 0.56\,\mathrm{MHz/nm}$.

From Figs. 6.4 and 6.5, larger folding angle and larger FSR enhance the sensitivity to the CML thickness. Therefore, the sensitivity of the CEE can be improved by optimizing the geometrical parameters of the folded cavity. On the other hand, the amount of resonant frequency split also becomes larger as the sensitivity increases. For example, when the folding angle becomes $\gamma \approx 40\,\mathrm{deg}$ with $f_{\mathrm{FSR}} = 1.84\,\mathrm{GHz}$, the sensitivity is about $1.3\,\mathrm{MHz/nm}$ and the resonant frequency split is enhanced to be $-230\,\mathrm{MHz}$. Such a large frequency split makes it difficult to scan the laser frequency by a current tuning because the scan range is about $200\,\mathrm{MHz}$ for our setup. Therefore, the improvement of the sensitivity accompanies difficulties.

One possible approach to measure the CML thickness with improved sensitivity is to add another P-polarization beam path with double-pass AOM configuration [85]. Fig. 6.6 shows the overview of possible upgrade configuration. Here, we set the folding angle and FSR to be $\gamma = 33\,\mathrm{deg}$ and $f_{\mathrm{FSR}} = 3.00\,\mathrm{GHz}$. With these parameters, the sensitivity and resonant frequency split become $\zeta = 1.83\,\mathrm{MHz/nm}$ and $\Delta\nu \approx 160\,\mathrm{MHz}$, respectively. By using an AOM which has $80\,\mathrm{MHz}$ central frequency, double-pass AOM configuration enables us to

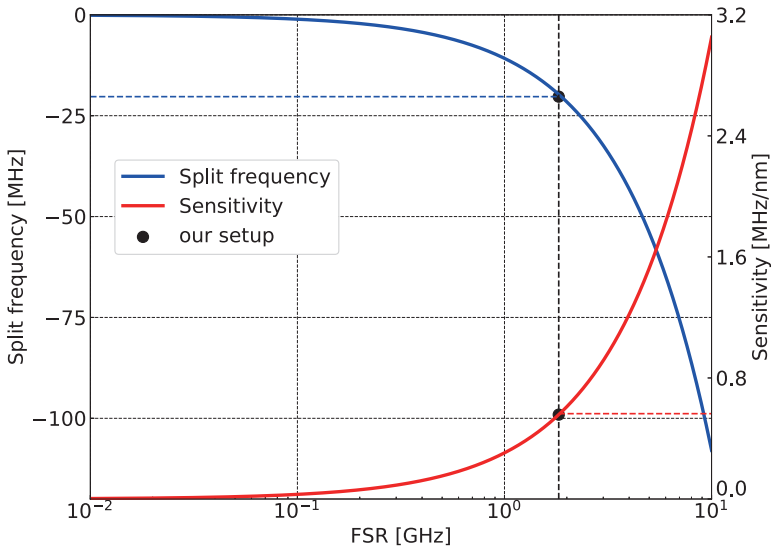

Figure 6.5: How the sensitivity of CEE change over the FSR. Folding angle 22.5 deg is assumed. Black dots correspond to our setup.

shift the laser frequency about 160 MHz without beam jitters. By tuning the laser frequency shift introduced by a double-pass AOM, one can determine the frequency split between P- and S-polarization beams. Thus, the CML thickness can be probed with improved sensitivity. It should be noted that the resonant width, which introduces an error, becomes large depending on the FSR. In order to maintain the resonant width less than 0.1 MHz, the finesse of the folded cavity should be increased to approximately 3×10^4. However, with a large folding angle, realizing a coating with very high reflectivities for both S- and P-polarizations at the same time becomes increasingly difficult. Therefore, it may be difficult to increase the finesse so much.

6.3 Formation Speed

6.3.1 Formation Speed Degradation

As shown in Fig. 5.13, the CML growing rate decreases with time, i.e., the CML formation rate is not constant. This can be caused by the molecular flow onto the mirror gradually reduced as a consequence of improvement in

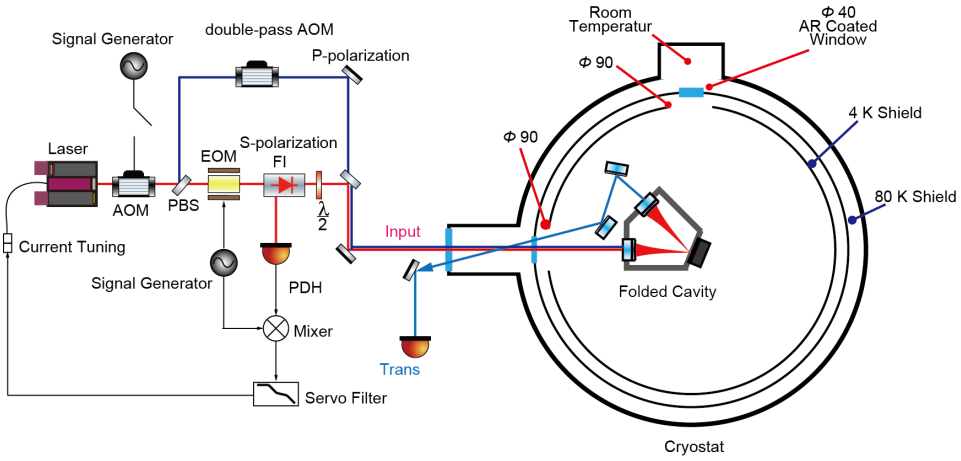

Figure 6.6: A possible upgrade configuration. Additional beam path is introduced with double-pass AOM to shift the laser frequency about 160 MHz.

the vacuum level. Fig. 6.7 shows the pressure between the room temperature and the 80 K shields and the CML formation speed. Here the CML formation speed is obtained by taking the derivative of CML thickness shown in Fig. 5.13. During the cryogenic operation, the pressure and the CML formation speed decreases as shown in Fig. 6.7. The CML formation speed, η, scales with the pressure difference, ΔP, between the room temperature and cryogenic vacuum as [58]

$$\eta \propto \Delta P. \tag{6.8}$$

Here, we assume that the pressure difference is the same as the pressure at the room temperature vacuum because the cryogenic vacuum level is expected to be much lower than the room temperature part.

The improvement in the room temperature vacuum, hence the reduction in ΔP leads to a smaller formation speed. Thus, the decreasing pressure could cause the thickness trend as shown in Fig. 5.13. However, the CML formation speed decreased about one order of magnitude though the improvement in vacuum level is about a factor of 2. Therefore, the CML formation speed may not be simply proportional to ΔP. Further investigations are needed to reveal the relation between the CML formation speed and the vacuum level.

6.3.2 Comparison with the Measurement in KAGRA

Tab. 6.2 shows the comparison of our results with the previous measurement in KAGRA. The CML formation speed in KAGRA was 27 nm/day, which

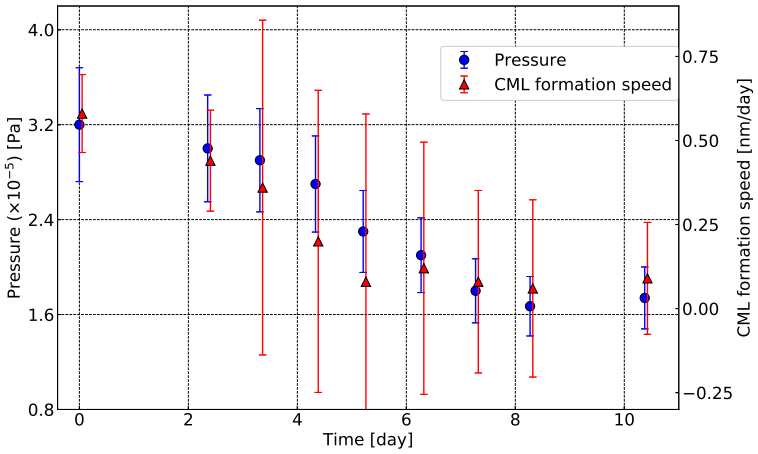

Figure 6.7: Trend of the pressure at room temperature vacuum and CML formation speed during the cryogenic operation. The error bars of pressure are due to the uncertainty of the vacuum gauge.

was obtained by measuring the finesse oscillation induced by CML formation [58]. Here, CML formation speed is assumed to be proportional to the vacuum pressure at room-temperature part ΔP, and a solid angle of Ω from the center of the mirror to the room temperature part. The solid angle is calculated as

$$\Omega = 2\pi \left(1 - \frac{z}{\sqrt{z^2 + r^2}}\right), \tag{6.9}$$

where z is the distance from the mirror to the edge of cryogenic duct and r is the radius of the duct. For the case of KAGRA, $z = 5\,\mathrm{m}$ and $r = 270\,\mathrm{mm}$ are assumed, and the solid angle becomes 2 msr. In our setup, substituting $z = 300\,\mathrm{mm}$ and $r = 20\,\mathrm{mm}$ to Eq. 6.9, the solid angle to the room-temperature vacuum becomes 14 msr, which is 7 times larger than that of KAGRA. Moreover, the vacuum level of our setup is about 6 times worse than the previous study [58]. Considering these difference, the expected CML formation speed in our setup from measurement in KAGRA becomes

$$\eta_{\mathrm{expect}} = 27\,\mathrm{nm/day} \times 7 \times 6 \approx 1.1 \times 10^3\,\mathrm{nm/day}. \tag{6.10}$$

On the other hand, the experimentally obtained formation speed in our setup is only 0.6 nm/day at most, which is about 2×10^3 times smaller than the theoretically expected value from the KAGRA case. Such a large discrepancy in

Table 6.2: Comparison with the previous measurement in KAGRA [59].

	in KAGRA	our setup
Configuration of cavity	Fabry-Perot	Folded
Wavelength	1064 nm	1550 nm
Solid angle	2 msr	14 msr
Vacuum level	5×10^{-6} Pa	3×10^{-5} Pa
Method	finesse oscillation	cavity enhanced ellipsometry
Formation speed	(27 ± 2) nm/day	(0.6 ± 0.1) nm/day

the CML formation speed may be generated by the difference in the geometry of the vacuum system between KAGRA and a table top experiment. Further studies are needed to understand this difference in the CML formation speed.

It should be noted that the measurement in KAGRA assumed the constant CML formation though the formation rate may not be constant in practice [58]. The cavity enhanced ellipsometry enables the measurement of the formation rate even if the rate is not constant, which is one of the advantages of this technique. Further measurements in GWDs will help understand the CML formation rate combined with the simulation presented in the following section.

6.4 Estimation of the CML Formation Rate in Future GWDs

So far, we have revealed that the CML can hinder the cryogenic operation of future GWDs even though its thickness is less than 1 nm. Here, we compute the CML formation rate, in the same manner as in a previous study [59], to estimate the timescale that the heat input due to the CML becomes a problem. The timescale can be regarded as an index for designing the cryogenic systems of future GWDs. We assume a simple beam duct model for order estimation of CML formation rate during the stationary state.

In order to evaluate the formation rate, first, we derive the sticking probability of residual molecules, $\mathscr{P}_{\mathrm{st}}$, which describes the ratio between the number of molecules that input to the cryogenic surface and that adhere to the surface.

The sticking probability can be expressed as [86].

$$\mathscr{P}_{\mathrm{st}} = \alpha\{1 - \tanh[\beta(T - \gamma E_{\mathrm{des}})]\}, \tag{6.11}$$

where α, β and γ are the parameters to reproduce the experimental results and E_{des} is the desorption energy. These values are listed in Table 6.3.

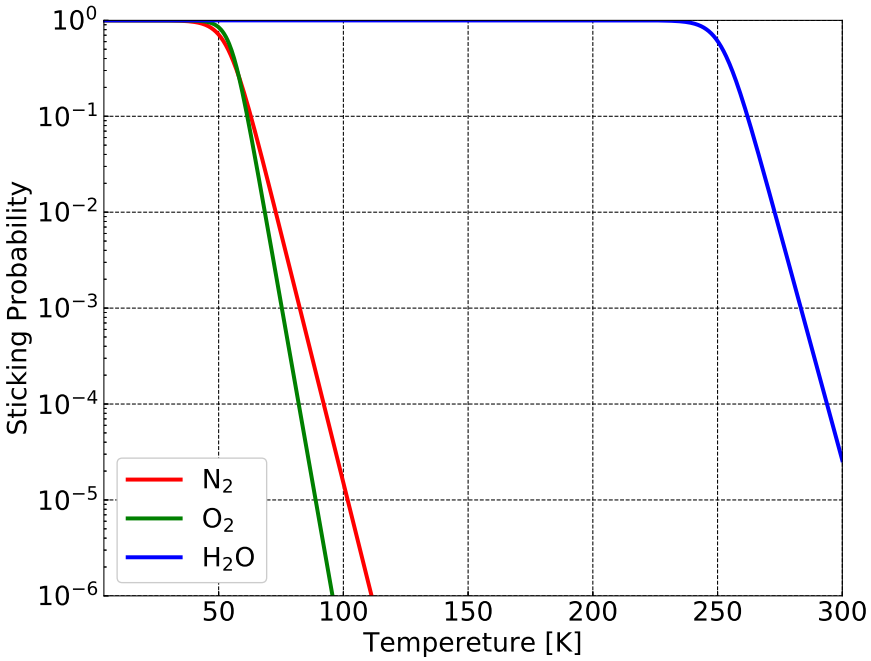

Figure 6.8: Sticking probability of several molecules. The parameters to calculate the sticking probabilities are listed in Tab. 6.3. At the cryogenic temperature of 10 K, almost all residual gas molecules can stick to the cryogenic surface.

Fig. 6.8 shows the sticking probabilities of H_2, N_2, O_2, and H_2O molecules as functions of temperature. The sticking probability of water molecules can be treated as equal to 1 below about 250 K. In addition, the sticking probabilities of other molecules are also almost unity at 10 K. Therefore, the measured finesse fluctuation can be induced by the mixture layer of these molecules.

In order to evaluate the molecular layer formation rate, an MC simulator package developed at CERN, Molflow+ [87], is used. A previous study shows that the numerical simulation using Molflow is valid for order estimation [58]. Here we make 3D CAD models of cryogenic duct of the ET and LIGO Voyager based on the Refs. [30, 88]. By using these models for MC simulation, one can obtain the formation rate of CML as following. Assumed parameters for the cryogenic duct are listed in Tab. 6.4.

Table 6.3: The parameters used to calculate the sticking probability [86]. E_{des} denotes the desorption energy.

Molecule	β	γ	E_{des}
N_2	0.12	0.043	1250
O_2	0.17	0.042	2320
H_2O	0.11	0.042	6000

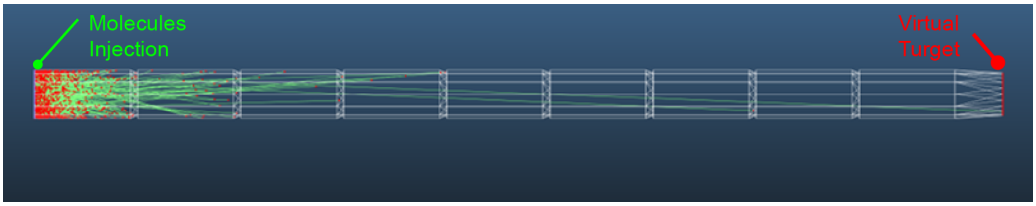

Figure 6.9: Model for the conductance simulation of the space between the duct shield and the test mass. The particles are injected from the left-end facet, and the number of particles which reach to the right-end facet are counted.

First, we define the volumetric flow rate Q as

$$Q = C\Delta P, \tag{6.12}$$

where C is the conductance of the system and ΔP is the pressure difference. Here we consider the cylindrical beam tube. MC simulation is one of the best approaches to estimate the conductance. By using the transmission probability (or Clausing factor), K, the conductance of the beam tube can be expressed as

$$C = C_0 K, \tag{6.13}$$

where C_0 is the opening conductance of the system which can be expressed as

$$C_0 = r^2\sqrt{\frac{\pi k_{\mathrm{B}} T}{2m}}. \tag{6.14}$$

Here r is the radius of the duct, k_{B} is the Boltzmann constant, T is the temperature and m is the mass of the molecule. The CML grows with time due to the continuous residual molecular flow from the beam tube. The formation rate can be calculated as

$$\eta = \frac{mQ}{S\rho k_{\mathrm{B}} T}\,[\mathrm{m/s}], \tag{6.15}$$

Table 6.4: The assumed parameters of cryogenic duct of the ET and LIGO Voyager.

Name	The ET	Voyager
Diameter	0.75 m	0.50 m
Temperature	4 K and 77 K	80 K
Length	5 m / 4 K + 50 m / 77 K	$\sim$ 10 m

where S is the area of the cryogenic mirror surface and ρ is the density of the molecule. Assuming the pressure difference between the beam duct and the cryostat, one can estimate the formation rate of the CML from Eq. 6.15.

The Einstein Telescope

We consider the case of the ET. The cryogenic beam duct of the ET consists of two parts — 50 m long 77 K cryotrap, and 5 m long 4 K cryotrap. The conductance can be calculated as

$$C_{\mathrm{ET}} = \frac{1}{1/C_{77\mathrm{K}} + 1/C_{4\mathrm{K}}}, \tag{6.16}$$

where $C_{77\mathrm{K}}$, and $C_{4\mathrm{K}}$ are conductance of each cryotrap.

The transmission probability of 77 K cryotrap, $K_{\mathrm{trans},77\mathrm{K}}$, for each molecule is simulated as

$$K_{\mathrm{trans},77\mathrm{K}} = \begin{cases} 4.9 \times 10^{-5} & (\mathrm{H_2O}), \\ 2.0 \times 10^{-4} & (\mathrm{N_2}), \\ 5.0 \times 10^{-3} & (\mathrm{O_2}). \end{cases} \tag{6.17}$$

That for 4 K cryotrap also is calculated as

$$K_{\mathrm{trans},4\mathrm{K}} = 5.5 \times 10^{-3} \quad (\mathrm{H_2O}, \mathrm{N_2}, \mathrm{O_2}). \tag{6.18}$$

Here we assumed that the sticking probability of these molecules are the unity at 4 K.

Then we compute the conductance. The opening conductance of each cry-

otrap is calculated as

$$C_{0,77\mathrm{K}} = \begin{cases} 3.6 \times 10^{-3} & (\mathrm{H_2O}), \\ 6.0 \times 10^{-3} & (\mathrm{N_2}), \\ 3.3 \times 10^{-1} & (\mathrm{O_2}). \end{cases} \tag{6.19}$$

$$C_{0,4\mathrm{K}} = \begin{cases} 3.6 \times 10^{-1} & (\mathrm{H_2O}), \\ 1.6 \times 10^{-1} & (\mathrm{N_2}), \\ 1.5 \times 10^{-1} & (\mathrm{O_2}). \end{cases} \tag{6.20}$$

Substituting these values into Eqs. 6.13 and 6.16, one can obtain the conductance of cryotrap as

$$C_{\mathrm{ET}} = \begin{cases} 3.6 \times 10^{-3} & (\mathrm{H_2O}), \\ 5.8 \times 10^{-3} & (\mathrm{N_2}), \\ 1.1 \times 10^{-1} & (\mathrm{O_2}). \end{cases} \tag{6.21}$$

The residual gas inside the room temperature beam duct is estimated as 5×10^{-9} Pa for H_2O, and 1×10^{-10} Pa for the others [30]. As the vacuum level in the cryostat chamber is much better than the room temperature beam duct because of the cryopumping, it is natural to adopt these values as pressure difference between the beam duct and the cryostat chamber. Thus the molecular flow can be estimated as

$$Q_{\mathrm{ET}} = \begin{cases} 1.8 \times 10^{-11} & (\mathrm{H_2O}), \\ 2.9 \times 10^{-13} & (\mathrm{N_2}), \\ 5.3 \times 10^{-12} & (\mathrm{O_2}). \end{cases} \quad \mathrm{Pa \cdot m/s} \tag{6.22}$$

It should be noted that we assumed $\Delta P = 5 \times 10^{-11}$ Pa for N_2 and O_2. From Eq. 6.15, the formation rate is calculated as

$$\eta_{\mathrm{ET}} \sim \begin{cases} 6 \times 10^{-5} & (\mathrm{H_2O}), \\ 4 \times 10^{-6} & (\mathrm{N_2}), \\ 6 \times 10^{-5} & (\mathrm{O_2}). \end{cases} \quad \mathrm{nm/day} \tag{6.23}$$

Assuming that the CML is a mixture of these molecules, the formation rate of CML is approximately 1.2×10^{-4} nm/day ~ 0.05 nm/yr for the ET. Therefore, the CML formation can be tolerable for about 4-year operation of the ET as long as it achieves the designed vacuum level with approximately 50 m cryotraps.

Figure 6.10: Schematic of CAD model of Voyager cryogenic duct. The length is 10 m with 500 mm diameter. Baffles are located at 1 m intervals. The yellow part represents the space between the end of the duct and mirror surface.

LIGO Voyager

LIGO Voyager is planning to employ cryogenic ducts at temperature of 80 K to isolate thermal radiation [88]. The length of cryogenic shield is about 10 m as LIGO Voyager utilize the facility of LIGO.

Temperature of LIGO Voyager test mass is designed as 123 K where only H_2O can be adsorbed, i.e., the adsorption of other species are negligible. Therefore, here we only consider the adsorption of H_2O molecules. Fig. 6.10 shows the CAD model of Voyager cryogenic duct. The transmission probability K_{trans} of the LIGO Voyager cryogenic duct is simulated as

$$K_{\mathrm{trans,80K}} = 4.5 \times 10^{-4}. \tag{6.24}$$

It should be noted that the transmission probability without baffles is computed as 6.0×10^{-4}. Therefore, the baffles reduces the transmitted molecules approximately by 25 %. Opening conductance is also calculated as

$$C_{0,\mathrm{Voyager}} = 23.37. \tag{6.25}$$

Then, the conductance of the Voyager cryogenic duct becomes

$$C_{\mathrm{Voyager}} = 1.3 \times 10^{-2}. \tag{6.26}$$

For the case of LIGO Voyager, residual water molecules inside the beam tube is estimated as $\sim 1 \times 10^{-10}$ Torr $= 1.33 \times 10^{-8}$ Pa [35]. Thus, the molecular flow is calculated as

$$Q_{\mathrm{Voyager}} = 1.7 \times 10^{-10}\,\mathrm{Pa \cdot m^3/s}. \tag{6.27}$$

Finally, the formation rate is estimated as

$$\eta_{\mathrm{Voyager}} \sim 7 \times 10^{-4}\,\mathrm{nm/day}. \tag{6.28}$$

Table 6.5: The estimated formation rate with designed vacuum level. The values for the KAGRA case are derived from the reference [59].

Detector	Molecules	Formation Rate [nm/day]
KAGRA	H_2O	6×10^{-1}
	N_2	3×10^{-1}
	O_2	2×10^{-1}
The ET	H_2O	6×10^{-5}
	N_2	4×10^{-6}
	O_2	6×10^{-5}
Voyager	H_2O	7×10^{-4}

This result indicates that the thickness of CML can become approximately 0.2 nm after one year run, which can deteriorate the detector performance. It should be noted that the actual diameters of cryotraps can become larger than assumed here to avoid beam clippings. If the diameter of the beam duct is larger, the formation rate is also enhanced, and the CML becomes a problem much faster than the estimation shown above. Moreover, the unexpected leakage or degas can happen during the operation, resulting in the CML formation. Therefore, the formation rate calculated here is an optimistic estimation. Careful treatments on vacuum system and cryogenic mirror are still necessary.

The estimated results including KAGRA case are summarized in Tab. 6.5.

Table 6.6: Assumed parameters to compute the CML formation rate.

Molecule	Density [kg/m^3]	Mass [kg]
H_2O	940	2.99×10^{-26}
N_2	1026	4.65×10^{-26}
O_2	1520	5.32×10^{-26}

6.5 Possible Solutions to Mitigate the Impacts of the CML

The optical absorption induced by the CML can become a critical problem within one or two years operation with current proposed design. In this section,

we propose several approaches, which can mitigate the impact of the CML.

6.5.1 Longer Cryotrap

Cryotraps mitigate the CML formation as it reduces the molecular flow from the room temperature vacuum. Not only the CML formation, but also the heat input to the test mass by thermal radiation is reduced by longer cryotrap. In a cryogenic system, unknown heat sources may exist, which prevent one to cool down the system to the target temperature. Therefore, the designing of the cryogenic system with extra cooling capacity will be desirable in case of unforeseen heat sources. This can be achieved by employing longer cryotraps for the case of the ET, in which a radiation heat from room temperature vacuum is critical.

Current design of the ET adopts 5 m long for the 4 K cryotrap and 50 m for 77 K, and they reduce the thermal radiation from the room temperature to approximately 70 mW. Furthermore, by making the 4 K cryotrap 3 m longer, i.e., by employing 8 m long 4 K cryotrap, one can achieve less thermal radiation. It is estimated that such cryotrap can reduce the thermal radiation to approximately 10 mW. Thus, the heat input due to the absorption of coatings and thermal radiation becomes ~ 30 mW. This smaller heat input relieves the tolerance on the CML, and can handle with unexpected heat source. Moreover, the formation rate of the CML is also reduced. The conductance of 8 m long 4 K cryotrap becomes

$$C_{4\mathrm{K},8\mathrm{m}} = \begin{cases} 7.2 \times 10^{-2} & (\mathrm{H_2O}), \\ 3.3 \times 10^{-2} & (\mathrm{N_2}), \\ 3.1 \times 10^{-2} & (\mathrm{O_2}), \end{cases} \tag{6.29}$$

and the formation rate is

$$\eta \sim \begin{cases} 6 \times 10^{-5} & (\mathrm{H_2O}), \\ 4 \times 10^{-6} & (\mathrm{N_2}), \\ 2 \times 10^{-5} & (\mathrm{O_2}). \end{cases} \quad \mathrm{nm/day} \tag{6.30}$$

Thus, the formation rate of the CML becomes approximately 8×10^{-5} nm/day $\sim$ 0.03 nm/yr.

As shown above, longer cryotraps can mitigate the impacts of the CML. By employing 8 m long 4 K cryotraps, heat input due to the thermal radiation and absorption of coatings becomes approximately 30 mW. In other words, the ET can tolerate about 70 mW unexpected heat input, which corresponds to the heat input caused by 1 nm thick CML. The CML formation also can be

mitigated as 0.03 nm/yr. Thus, the ET can be operated with 10 K test masses for about 30 years.

For the case of LIGO Voyager, as the current LIGO facility will be used, longer cryotraps are difficult to be installed. Cosmic Explorer (CE), a next generation GWD planned in the US, may better employ 50 m-scale cryotraps from the view point of the CML formation though the 10 m long cryotrap is enough from the view point of the thermal radiation.

6.5.2 Cooling Order

One possible approach to prevent the CML formation during the cooling period is to cool down the mirror at the last stage of the cooling process, i.e., cool down the surrounding components first, then start to cool down the test mass. During this process, the residual gas molecules are adsorbed by the surrounding cryogenic components, which mitigates the CML formation on the test mass mirror surface. LIGO Voyager will employ radiative cooling system in which cryotraps are cooled down prior to the test mass, resulting in the adsorption of residual molecules to the cryotraps. Therefore, the CML formation on the mirror during cooling process can be mitigated for LIGO Voyager. For the case of the ET, long cryotraps are installed in the beam tube. By cling down the cryotraps first, they can adsorb the residual gas molecules and the CML formation on the test mass mirror is much reduced.

However, still the unwanted leakage or degas can happen accidentally. They may cause unexpected CML formation, which cannot be predicted by the simulation. The monitoring system, which can witness the CML, may be necessary to check the status of the mirror.

6.5.3 Monitoring and Desorption System

The CML formation can degrade detector's performance, and the system which can witness the CML may be needed to identify the optical loss source. As a starting point, we propose a conceptual design of a monitoring system which is inspired by the P-S splitting measurement.

The schematic picture of the monitoring system is shown in Fig. 6.11. In this scheme, the auxiliary cavity is employed in which the test mass mirror takes the role of folding mirror. One can probe the cryogenic mirror surface by monitoring the resonant frequency shift between two polarizations. This enables to confirm the status of the mirror surface; whether the CML is formed or not.

Tab. 6.7 describes the assumed parameters. Here we consider the case of the ETM in the ET, and assume the mirror coating as proposed in the

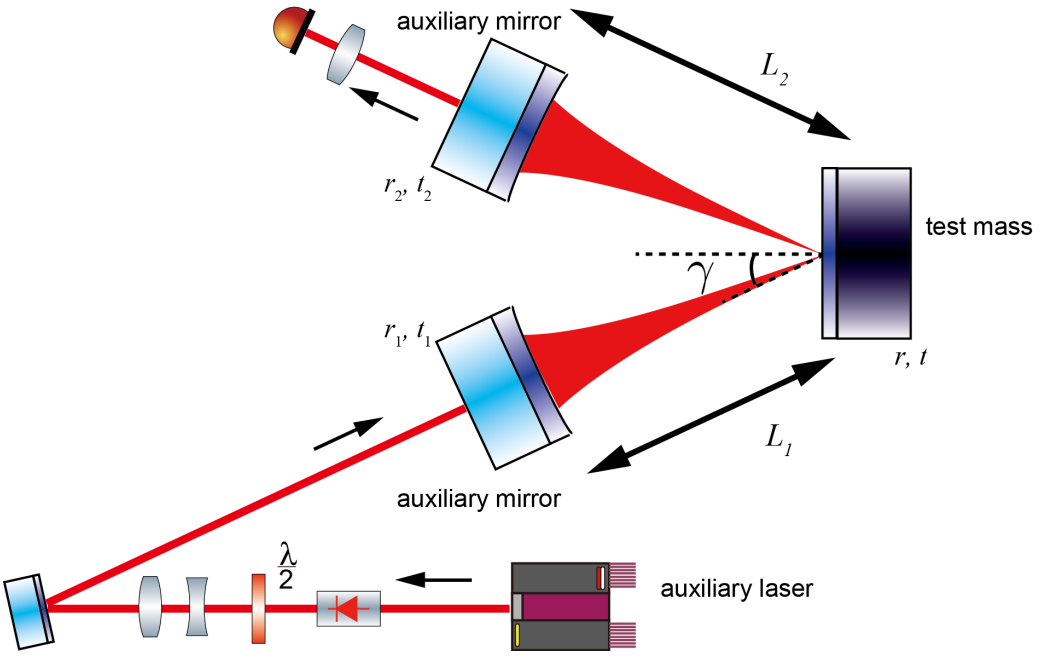

Figure 6.11: Conceptual design of cryogenic mirror surface monitoring system. Two auxiliary mirrors compose input and output mirrors, and the test mass mirror takes the role of folding mirror. Hence these three mirrors consist a folding cavity. By detecting transmitted beam using a PD, one can measure the two resonant peaks depending on the polarization.

reference [32]. We assume the finesse of the auxiliary cavity as 5×10^3. Then the frequency shift can be calculated by using a characteristic matrix as

$$\Delta\nu(d_{\mathrm{CML}} = 0\,\mathrm{nm}) = -7.547\,\mathrm{MHz}. \tag{6.31}$$

As the FWHM is approximately 10 kHz and the transverse mode spacing is 28.7 MHz, the shifted peak is not contaminated by other modes. Therefore, one can detect the both P- and S- polarization transmitted peak.

Fig. 6.12 shows the response of frequency shift against the CML formation. The frequency shift changes linearly against the CML formation at very thin region. Such response can be fitted by

$$\Delta\nu\,[\mathrm{MHz}] = 0.022\,[\mathrm{MHz/nm}] \times d_{\mathrm{CML}}\,[\mathrm{nm}] - 7.547\,[\mathrm{MHz}]. \tag{6.32}$$

By using this relationship, one can estimate the optical thickness of the CML at thin region.

For the case of the ITM, the finesse of the auxiliary cavity becomes smaller than that of the ETM due to lower reflectance of the ITM. The finesse of the

Table 6.7: Assumed parameters for the monitoring system.

Parameters	Value
Wavelength	1550 nm
Finesse	$\sim 5 \times 10^3$
Cavity length	$L_1 = 1.5\,\mathrm{m}$
	$L_2 = 1.5\,\mathrm{m}$
	$L = L_1 + L_2 = 3\,\mathrm{m}$
Free spectral range	50 MHz
Transverse mode spacing	33.7 MHz
FWHM	7.5 kHz
Beam size on the input/output mirror	1.7 mm
Beam size on the folding mirror	1.4 mm
Radius of curvature	10 m
Folding angle	45 deg

ITM auxiliary cavity is 500 at most, hence $\nu_{\mathrm{FWHM}} = 75\,\mathrm{kHz}$. The resonant frequency split with very thin CML is approximated as

$$\Delta\nu\,[\mathrm{MHz}] = 0.022\,[\mathrm{MHz/nm}] \times d_{\mathrm{CML}}\,[\mathrm{nm}] - 7.487\,[\mathrm{MHz}]. \tag{6.33}$$

As the resonant frequency separation is still larger than the FWHM, the monitoring system can be valid for the ITM though the resolution of the frequency split gets worse due to the lower finesse. Further tuning such as slightly different laser wavelength may improve the performance of the system.

In order for precise P-S measurement using such monitoring system, calibration lines around the split peak is useful.From the separation of the calibration line and resonant peak, one can determine the scanning efficiency of the laser frequency. By using the obtained scanning efficiency, the resonant frequency split is calculated, and the thickness of the CML can be estimated from Eq. 6.32. Also, the reduction of the mirror motion is important factor for precise measurement. The beam jitter generated by the mirror motion leads to the fluctuations in the split frequency. When the beam jitter is less than 200 μrad, the fluctuations in the split frequency becomes less than 7 kHz. Then, one can measure the thickness of the CML with an accuracy of 0.3 nm. A single or double pendulum can reduce the vibration contamination to the mirrors, and enable the estimation of the CML thickness.

One advantage of such monitoring system is the linearity of response to the molecular layer formation. In addition, this system does not require a robust control system to maintain the resonant condition for the P-S measurement.

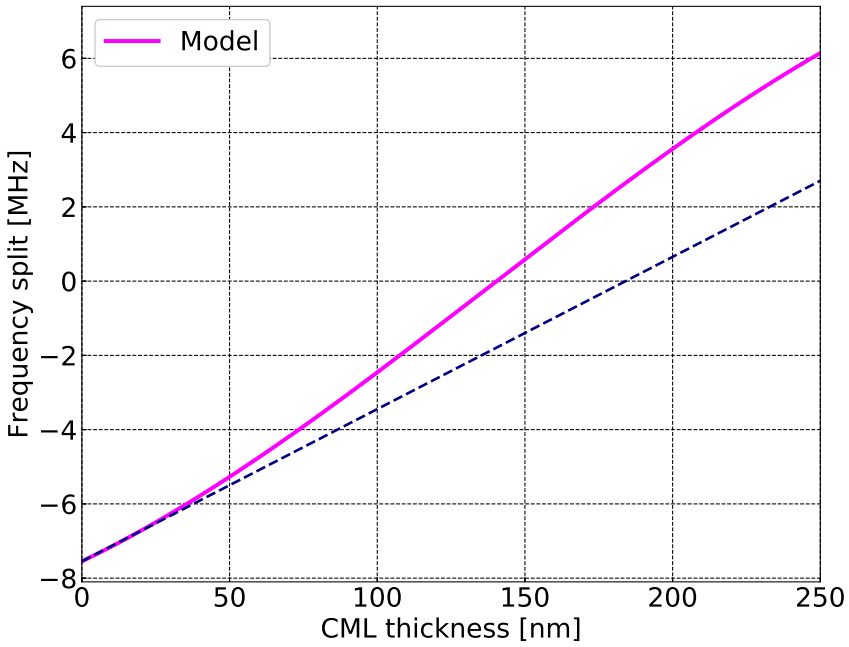

Figure 6.12: Example response of the resonant frequency shift of assumed monitoring system. Dashed line is a linear approximation at the thin region.

However, the sensitivity of monitoring system becomes about one order of magnitude smaller than our setup though the folding angle is larger which improves the sensitivity. This is because of the longer cavity length of the monitoring system. In other words, the FSR of the monitoring system becomes about two orders of magnitude smaller than our setup, resulting in less sensitivity as shown in Fig. 6.5. Here we assumedthe cavity length to be 3 m in order not to clip the main laser of the GWD.

The resonant width becomes small as the FSR decreases. Therefore, the error due to the resonant width also is unchanged in terms of the CML thickness. The systematic error induced by the CML refractive index also does not change because the error manifests itself as an error in the phase shift $\Delta\phi$, which is scaled by the FSR as shown in Eq. 4.72 when converted to the frequency shift. Therefore, the only error which increases as the FSR decreases is the statistical error. This error can be reduced by increasing the number of averaging to a large number like 10^4. Manually performing such a large number of measurements is impractical. Therefore, it is necessary to develop

an automatic measurement system to perform the scan, data acquisition and peak finding by a fit without human intervention.

The monitoring system proposed here should take an important role in not only operation period, but also commissioning phase. During the commissioning, it is important to identify the noise sources and technical problems which hinder the cryogenic operation. The cryogenic mirror monitoring system can provide significant information to determine the excess optical loss source. Such monitoring system assists the commissioning work and achieve the design sensitivity, resulting in discoveries in the Universe.

Towards the future GWDs, implementation in prototypes and optimization of the geometric parameters will be of importance. Also, the obtained results by the measurements in the prototypes can provide insights into the design of the vacuum system such as length of the cryotrap and vacuum level. Further studies will help developing the vacuum and cryogenic systems, and increase the feasibility of future cryogenic GWDs.

6.5.4 Laser Induced Desorption System

The development of the system, which can actively remove the CML will also be important. Previous study shows the possibility to desorb the CML by illuminating an auxiliary CO_2 laser [59]. A CO_2 laser can increase the temperature of a mirror. A thermal compensation system which employs a CO_2 laser is installed in current GWD such as aLIGO [89]. This previous study indicates that the adsorbed water molecules can be desorbed by increasing the temperature to about 170 K. However, such desorption has not been demonstrated with an optical cavity. The cryogenic folded cavity and the cavity enhanced ellipsometry, which we have developed, can be used as a test bench for the laser induced desorption system. Further studies utilizing the folded cavity can pave the way to develop a desorption system for future cryogenic GWDs, which will be able to solve the problem generated by the CML.

6.6 Future Prospects

The cryogenic folded cavity developed in this study can be utilized for development of low thermal noise coating toward cryogenic GWDs. By locking two higher-order modes to this cavity and taking beat note of them, one can measure the coating thermal noise of folding mirror [90, 91]. The device we developed here will enable the direct measurement of coating thermal noise even at cryogenic temperature in addition to the optical loss. Combining these measurements, one can develop high-end coatings for cryogenic GWDs.

In order to achieve the direct measurement of coating thermal noise, a vibration isolation system is necessary as the vibration contamination prevent the precision measurements of coating thermal noise. Developments of additional optical and readout systems are also required. Further studies utilizing the cryogenic folded cavity will be able to contribute to the future cryogenic GWDs.

Chapter 7

Summary and Conclusion

The detection of GW opened a new window to the Universe, which is called GW astronomy. Future cryogenic gravitational-wave detectors will be able to provide further discoveries such as the formation scenarios of massive black holes by improving the sensitivity. The development of cryogenically cooled mirror is an important key to achieve the future cryogenic GWDs. A number of studies were conducted to realize cryogenically cooled mirrors in future GWDs. CLIO and KAGRA are pioneers toward the development of a cryogenic GWD. For the construction and cryogenic operation of KAGRA, experimental studies were performed to estimate the degradation time of PRG and to estimate the CML formation speed. Based on these studies, KAGRA was designed and constructed.

In future GWDs such as the ET or LIGO Voyager, employment of cryogenically cooled mirrors is an indispensable technology. These GWDs are planing to employ longer wavelength laser than that of KAGRA to utilize silicon mirrors. At these longer wavelength, amorphous ice, which is a main component of a CML, has two orders of magnitude larger absorption coefficient. Therefore, studies to investigate the impacts of CML at these wavelength is important for future GWDs.

We have theoretically estimated the impacts on optical loss induce by the CML for future GWDs, which have not taken into account for their current design. The results show the optical absorption by the CML can deteriorate the performance of GWDs. The PRG, which is a merit of optical performance of GWD, decreases due to the CML formation. We estimated the tolerable CML thickness at which the degradation of PRG becomes 10%. The tolerable thicknesses for the ET and LIGO Voyager are 60 nm and 25 nm, respectively, while that of KAGRA is about 750 nm. Therefore, the optical performance of future GWDs can be easily deteriorated by the CML formation.

Moreover, as the CML will be exposed to high power beam, it absorbs a

large amount of heat. Assuming the Lambert-Beer law, the author revealed that heat input to the cryogenic mirror can exceed the cooling capacity even if its thickness is about 1 nm, which can hinder one to reach the target temperature, resulting in worse sensitivity.

The heat input to the cryogenic mirror can exceed the cooling capacity even at a ppm level optical loss and a nanometer level thickness for the case of the ET because the absorption coefficient of CML is expected to be 2 ppm/nm from the literature value of amorphous ice absorption coefficient. Therefore, the optical loss characterization at a ppm level and a nanometer thickness level is necessary to investigate the possible impacts on GWDs. Previous studies investigated the impacts of CML on KAGRA, which employs shorter wavelength laser than the ET or LIGO Voyager. However, the impacts of CML at longer wavelength such as 1550 nm or 2000 nm had not been studied so far. In order to characterize the optical loss and thickness of the CML with a ppm and nanometer levels at 1550 nm wavelength, we have developed a cryogenic folded cavity which consists of three mirrors — input and output mirrors, and one folding mirror. The device enables optical loss measurement by ring-down method at broadband temperature range, i.e., from room temperature to ~ 10 K cryogenic temperature. One advantage of folding configuration is that one can characterize the optical loss of very high reflective mirror. Moreover, the folding mirror enables cavity enhanced ellipsometry measurement which utilizes the phase shift induced by the folding mirror. The device and experimental method developed here enables us to characterize the optical loss and thickness of CML at longer wavelength, 1550 nm, where the impacts of CML has not been studied so far.

The measurement of frequency shift between P- and S-polarization, called P-S splitting measurement here, turned out to be a useful method to monitor the cryogenically cooled mirror surface. As the frequency split shifts with CML growth, one can estimate the CML thickness. The sensitivity of this measurement to the CML thickness is mainly determined by the geometrical parameters, folding angle and FSR of the cavity. In our setup, folding angle is set to 22.5 deg and FSR is 1.84 GHz. Also we assumed the CML refractive index as $n_{\mathrm{CML}} = 1.19$. From these values, the sensitivity to CML thickness can be calculated as 0.56 MHz/nm. The uncertainty in the measurement of the CML thickness is introduced by the statistical error, measurement error related to the resonant width and systematic error due to the CML refractive index. Measurement error related to the resonant width and systematic error due to the CML refractive index are calculated as ± 0.09 MHz and ± 0.01 MHz/nm, respectively. In our setup, the error due to the resonant width is converted as $(\pm 0.09\,\mathrm{MHz})/(0.56\,\mathrm{MHz/nm}) = \pm 0.16$ nm. Tak-

ing these into consideration, the uncertainty of the CML thickness becomes $(\pm 0.38 \pm 0.16 \pm 0.07)\,\mathrm{nm} = \pm 0.42\,\mathrm{nm}$.Therefore, the CML thickness can be measured by the cavity enhanced ellipsometry with an accuracy of about 0.5 nm. By increasing the folding angle γ and the FSR of the cavity f_{FSR}, a sensitivity to CML thickness can be enhanced. Further optimizations of these geometrical parameters may enable CML thickness measurements with higher accuracy. Through these measurements, we have achieved the optical loss characterization of CML at a ppm level and a nanometer level.

The measured optical loss of the CML shows large values even if its thickness is a few nanometer. When the thickness of the CML is $2.38 \pm 0.27\,\mathrm{nm}$, the optical loss becomes $7.3 \pm 1.1\,\mathrm{ppm}$. This result indicates that heat input to the test mass in the ET becomes larger than 100 mW with 2.4 nm thickness, i.e., the heat input exceeds the cooling capacity. On the other hand, the obtained result indicate that the Lambert-Beer law does not hold in very thin region as it shows the discrepancy from the fitted curve assuming the Lambert-Beer law. A recent simulation study by the LIGO Voyager group indicate that the optical absorption of a CML can deviate from the Lambert-Beer law at very thin region. However, the amount of deviation is too large compared to our experimental results. Further investigations are needed to precisely characterize the optical loss for a very thin layer.

CML formation speed is an important factor from the view point of maintaining a performance of cryogenic GWD. The study performed in KAGRA shows the CML formation speed of 27 nm/day. Our setup has worse vacuum level and larger solid angle to room temperature part compared to those of KAGRA. Therefore, large CML formation speed can be expected in our measurement, about $1.1 \times 10^3\,\mathrm{nm/day}$. However, the CML formation speed measured in our setup is only 0.6 nm/day, and about 2×10^3 times smaller than the theoretical expectation from previous study in KAGRA. One possible reason is that this difference may come from the difference in geometry of vacuum system between KAGRA and a table top experiment. Further studies are needed to understand the CML formation speed both in GWDs and table top experiments.

Besides the experimental study, we conducted numerical simulation to estimate the order of CML formation rate in the future GWDs. For the case of the ET, the CML formation can be tolerable for 4 years with current design. By employing 8 m long 4 K cryotrap instead of 5 m long one, the heat input is reduced and the CML formation can be tolerable for 30 years. LIGO Voyager can suffer the formation of CML after a half year of operation even if it achieves designed vacuum level. As the length of the cryotrap in LIGO Voyager is limited to about 10 m, it is difficult to mitigate the CML formation by

employing longer cryotraps. Though they achieve the designed vacuum level, unexpected degas or leakage can suddenly happen during long term operation, and a certain amount of CML might be formed. Such accidental contamination reduces the detector's performance and cannot be easily identified. Based on the cavity enhanced ellipsometry measurement, we propose a conceptual design of monitoring system for cryogenic mirror surface which can detect the CML formation with high sensitivity. Such monitoring system will be able to identify the CML formation and be useful not only for operation but also for commissioning.

In the future, the device and ellipsometric measurement, developed in this study, cab be used to develop the vacuum and cryogenic systems toward future cryogenic GWDs. One possible application is a measurement in the prototype detector such as Mariner, a prototype for LIGO Voyager [92]. Measurements for characterization of the CML in such prototypes will provide the insights into the formation rate or optical loss of the CML. Moreover, the cryogenic folded cavity can be utilized for the R&D of the CML desorption system and the direct measurement of coating thermal noise.

Our study revealed that the cryogenic molecular layer can become a critical problem in future cryogenic GWDs. The developed cryogenic folded cavity and cavity enhanced ellipsometry will help the design and the construction of future cryogenic gravitational-wave detectors.

Appendix A

Direct Measurement of Thermal Noise

The mirrors and their suspensions are thermally fluctuated because they are at a finite temperature. Thermal noise can be estimated by the fluctuation-dissipation theorem (FDT) and relates to the mechanical loss materials. As the mechanical loss of coating materials is much larger than that of substrates, thermal noise from dielectric coatings, called coating thermal noise (CTN), sets a limit in precision measurements such as gravitational-wave detection [20]. In order to realize future cryogenic GWDs, the development of low thermal noise coatings are necessary. Direct measurement of CTN at cryogenic temperature is important to develop new coatings. In this appendix, the direct CTN measurement technique and possible upgrade plans toward the direct CTN measurement are introduced.

A.1 Coating Thermal Noise

In order for a high reflective mirror such as a test mass in interferometric GWD, multilayer coatings are indispensable though which introduced thermal noise — this noise is called coating thermal noise (CTN). Thermal noise in coatings limits the sensitivity of the current gravitational wave detectors, the frequency reference and macroscopic quantum measurements. In other words, the improvement in the sensitivity of GWDs can be achieved by reducing the CTN with low mechanical loss coating, resulting in larger number of detection of GWs.

The fluctuation-dissipation theorem (FDT) describes the relationship between a fluctuating force and mechanical dissipation [93]. The single side power

spectral density (PSD) of the observable is given by [94]

$$S_x(f) = \frac{8k_{\mathrm{B}}T}{(2\pi f)^2}\frac{W_{\mathrm{diss}}}{F_0^2}, \tag{A.1}$$

where k_{B} is the Boltzmann's constant, T is the temperature and f is the frequency. And W_{diss} is the averaged dissipated energy in the coatings when subjected to a sinusoidal force $F(t) = F_0 \cos 2\pi f t$, where F_0 is the magnitude of the applied force to the system. The main mechanism which causes the dissipation in coatings is the mechanical loss, and the dissipation can be expressed as

$$W_{\mathrm{diss}}(f) = \frac{2F_0^2 d(1+\sigma)(1-2\sigma)\phi_{\mathrm{c}}}{w_0^2 Y} f, \tag{A.2}$$

where σ and Y are the Poisson ratio and Young's modulus of the coatings, respectively, and w_0 is the beam size.

A.2 Reduction of CTN

In order to reduce the thermal noises, several approaches are taken or being developed. Thermal noise reduction methods are explained below.

A.2.1 Cryogenic Mirror

Thermal noise can be reduced by employing a cryogenic test mass because thermal noise is proportional to the temperature. KAGRA employs cryogenic sapphire mirrors for test masses and they are cooled down to 20 K [20]. The future gravitational-wave detectors such as Einstein Telescope (ET) in Europe is also planning to use cryogenic mirrors to improve the sensitivity [69].

Cryogenic mirror, however, can induce vibration contamination through the heat links which in turns an undesirable noise. In order to achieve very low test mass temperature i.e., below 100 K where the radiation is not dominant, heat links are indispensable to extract heat from test masses. Heat links carry not only heat but also vibration and become noise sources. Moreover, residual gas molecules form molecular layers on cryogenic mirror surfaces which introduces optical loss i.e., scattering and absorption and reduce the finesse of the cavity [16, 58]. Therefore, one has to develop sophisticated cryogenic systems to use cryogenic mirrors in gravitational-wave detectors.

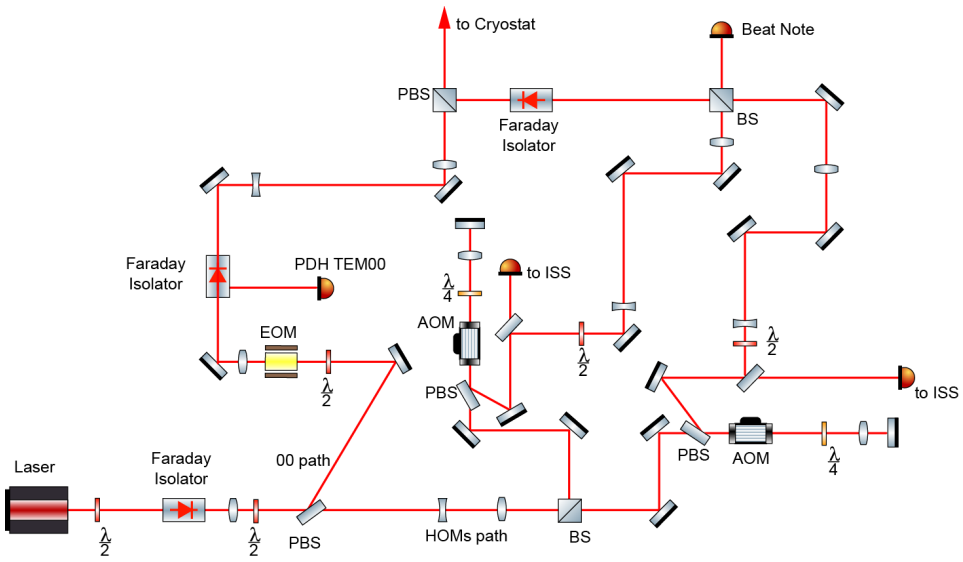

Figure A.1: A schematic view of planned input optics for direct measurement of coating thermal noise. There are three optical paths — one is to lock TEM00 mode, and other two are to lock TEM02/20 modes. The two higher-order-modes are generated by shifting the laser frequency using AOMs. By taking the beat note between TEM02 and TEM20 modes, one can measure the CTN. The details of measurement scheme are reported in the reference [90, 91].

A.2.2 Beam Size and Shape

As the CTN scales the beam size, the larger beam size leads to smaller CTN. In order for larger beam size, however, bigger mirror substrates have to be developed. In addition, high quality polishing of mirror surface and coating deposition are necessary. Therefore, enlarging the beam size involves several technical problems.

Another approach is to use a different beam shape. The substrate size can be maintained in this scheme while the effective beam area is larger. Different beam shapes can reduce the CTN such as mesa beam [95] or Laguerre-Gaussian 33 mode [96]. On the other hand, such beam shapes require special mirror shape and can be unstable due to the parametric instability [97].

A.3 Direct CTN Measurement by Using a Folded Cavity

Direct measurement of CTN by using a folded cavity is achieved at room temperature [90, 91]. In our experiment, a similar geometric folded cavity is used. Therefore, the cryogenic folded cavity developed here can be utilized for direct measurement of CTN with several upgrades in the future. Fig. A.1 shows a planned schematic layout of the input optics.

A.3.1 Three Different Spatial Modes

In MIT experiment, they employ three different spatial modes to probe the CTN.

Hermite-Gauss Modes

Laser beam has spatial modes which is called Hermite-Gauss (HG) modes. The complete set of transverse distribution of HG modes can be expressed as [81]

$$u_{mn}(x,y,z) = (2^{n+m-1}n!m!\pi)^{-1/2}\frac{1}{w(z)}\exp[i(m+n+1)\Psi(z)] \times H_n\left(\frac{\sqrt{2}x}{w(z)}\right)H_m\left(\frac{\sqrt{2}x}{w(z)}\right)\exp\left[-i\frac{k(x^2+y^2)}{2R_{\mathrm{C}}(z)}-\frac{x^2+y^2}{w^2(z)}\right], \tag{A.3}$$

where n and m are the mode numbers. The order of the mode is $n+m$ and $H_n(x)$ is the Hermite polynominals of order n.

In this measurement, three different spatial modes are used: one is TEM00, and the other two are HOMs called TEM02 and TEM20. TEM00 mode is used for stabilization of the laser frequency via PDH locking. Then, the CTN is sensed by two HOMs which have different spatial distribution.

TEM00 mode

TEM00 is the fundamental spatial mode of Hermite-Gaussian beam. In this experiment, TEM00 mode is used to stabilize the laser frequency via PDH scheme. The TEM00 beam is kept on resonance by feeding back the error signal to the laser.

TEM00 beam is phase modulated using EOM at 29.1 MHz for PDH locking to a folded cavity, which stabilizes the laser frequency by feedback control. Then the frequency stabilized laser will be split and shifted their frequencies by double-pass AOMs in order to generate HOMs.

TEM02/20 modes

TEM02/20 modes are the second lowest higher-order of HG beam which is used to sense the CTN in this experiment. There are a number of reasons to choose the TEM02 and TEM20 modes for the CTN measurement. First, as they are the second lowest higher order modes, coupling into these modes has no first order sensitivity to the misalignment of the cavity axis relative to the input beam axis. Secondly, even order modes of the optical cavity can be excited by the input beam in the fundamental mode. No special optics are required to achieve 12% of the power coupling. Lastly, modes of the same order are required to maintain a small separation in their resonant frequencies and keep high common mode rejection to the cavity noises.

These modes are generated by shifting the laser frequency by using AOMs. In our setup, two additional optical paths with double-pass AOMs are planed to be employed to lock the TEM02/20 modes, and measure the CTN.

A.4 Related Noise

Direct measurement of CTN involves a number of noises. Here we introduce several main noise sources which can prevent the measurement.

A.4.1 Seismic Noise

When we do precision measurements on the ground, seismic noise is an inevitable noise source which is dominant at lower frequency range. Seismic motion causes mechanical vibration of optical table which couples to the readout signal via several mechanisms.

Fluctuations of the cavity length induced by the seismic motion couples to the readout signal. The coupling can be reduced by common mode rejection. Residual coupling between the TEM02 and TEM20 modes can be expressed by

$$N_{02/20} = \frac{\Delta f_{02/20}}{f_0} N_{\text{length}} \tag{A.4}$$

where f_0 = is the laser frequency and $\Delta f_{02/20}$ is the frequency difference between the two HOMs.

Vibrations of the cavity mirrors cause backscattering noise which couples to the readout signal, which can be expressed as [90]

$$N_{02/20}(f) = (\alpha_{02} \cos\theta_{02} - \alpha_{20} \cos\theta_{20})\, N(f). \tag{A.5}$$

The backscattering coefficient α can be determined by

$$\alpha = \sqrt{\mathrm{BRDF}\frac{\lambda^2}{\pi w_0^2}}, \tag{A.6}$$

where BRDF $\sim 10^{-6}\,\mathrm{sr}^{-1}$ is the bidirectional reflectance distribution function of the sample mirror. Backscattering coefficients are slightly different from each other as TEM02/20 modes sense the different area of the sample mirror surface.

Mechanical motion of the input mirror induces noise in two ways. First, the longitudinal motion L_{input} modulates the phase of the beams according to the equation

$$N_{02/20}(f) = \frac{L_{\mathrm{input}}}{\lambda} 2\pi \frac{f}{f_0} L. \tag{A.7}$$

Also the angular motion of the input mirrors modulates the intra-cavity power which couples to the readout signal through the photothermal noise.

These noises induced by vibration are dominant at lower frequency region. In order to reduce the vibration noise, a vibration isolation system is necessary. Such an isolation system not only reduce the noise, but also vibration contamination from a cryocooler, which hinders the lock of the laser. On the other hand, a vibration isolation system reduces not only the vibration contamination, but also the cooling capacity below $\sim 100\,\mathrm{K}$. Further studies are needed to implement the vibration isolation system which can work at cryogenic temperature.

Residual gas noise

The residual gas along the optical path induces fluctuations in the phase of light through their refractive index. The noise level of the residual gas noise is expressed as

$$S_{\mathrm{gas}} = \sqrt{8\pi L}\frac{(n_0-1)^2}{(A_0/V_0)u_0\sqrt{\lambda}}\left(\frac{p}{p_0}\right)\left(\frac{T_0}{T}\right)^{3/2}, \tag{A.8}$$

where n_0 is the refractive index of the gas, V_0 is the volume of one mole of gas at the standard temperature, T_0, A_0 is the Avogadro's number and u_0 is the mean velocity of the gas molecule at the standard temperature [98]. At cryogenic temperature, the vacuum level is enough high due to the cryopumping, and the residual gas noise can be much smaller than the CTN.

Shot Noise

Shot noise is fundamental noise which is derived from the nature of quantum mechanics. Shot noise can be understood as photon counting error at a PD in a classical view [99]. In a modern picture, it can be considered as a consequence of the vacuum fluctuation in the electric magnetic field. It results in white noise and can be expressed as

$$S_{\mathrm{shot}} = \frac{\lambda}{8\mathcal{F}}\sqrt{\frac{2h\nu}{P_{\mathrm{in}}}}\frac{\sqrt{1-J_0^2(\Gamma)M}}{\sqrt{2}MJ_0(\Gamma)J_1(\Gamma)}, \tag{A.9}$$

where $J_k(\Gamma)$ is the k-th order of the Bessel functions and M is the mode-matching ratio. As the shot noise is in proportion to the inverse of the square root of the laser power, its noise level can be reduced by increasing the laser power. Larger laser power, however, introduces large heat input to the cryogenic folding mirror. Careful choice of the laser power may be required to measure the CTN.

Appendix B

Angular Response

In this appendix, we introduce the analytical calculation method for angular response of an optical cavity which reduces the cost for calculation.

Angular drifts directly introduce misalignment in the cavity axis. Such a misalignment can deteriorate detector sensitivity and stability by increasing a few noise couplings including those to length fluctuation and beam jitter. Moreover, angular misalignment causes light in the fundamental mode to be coupled into higher-order spatial modes, reducing the amount of power injected to the main part of gravitational wave detector. This directly decreases the detector sensitivity. Therefore, it is crucial to maintain the alignment of the IMC to achieve the detector operation with the best performance. In order to reduce angular misalignment, an alignment sensing and control (ASC) system is adopted by using the wave front sensing (WFS) technique [100, 101].

The WFS technique is sensitive to small tilts of the mirrors, and the WFS signals are obtained by demodulating signals detected by quadrant photodiodes (QPDs) [102]. Since the signals derived by the WFSs have a Gouy phase dependence, one has to precisely estimate its behavior and choose the QPD positions carefully in order to discriminate which mirror causes misalignments in either pitch or yaw. Previous report shows the analytical calculation of the WFS signals [102, 103]. These approaches, however, contain complexities due to the fact that the non-diagonal matrix elements are fully incorporated in the calculation. Therefore, the WFS signals of the IMC have been traditionally computed by simulation tools such as Finesse [104] or Optickle [105], and it was not easy to acquire intuitive interpretations.

The x and y axes of the coordinate system are chosen to be transverse to the beam propagation (z axis) which is perfectly aligned. We additionally assume that the y axis always points upwards regardless of the propagation direction. This automatically means that the x axis needs to be mirrored every time the light is reflected by a mirror. One can expand any paraxially approximated

electromagnetic fields of light beams by a set of Hermit-Gaussian (HG) modes as [76]

$$E(x,y,z) = \sum_{lm} \langle lm|E\rangle U_{lm}(x,y,z), \tag{B.1}$$

$$\langle lm|E\rangle \equiv \int_{-\infty}^{\infty}\int_{-\infty}^{\infty} U^{*}_{lm}(x,y,z)E(x,y,z)\mathrm{d}x\mathrm{d}y. \tag{B.2}$$

The coefficients $\langle lm|E\rangle$ can be represented as the elements of the vector in the modal space. For small misalignment due to the mirror tilts, the only important modes are fundamental TEM00 mode and the second lowest-order transverse modes, TEM10 and TEM01 [102]. Angular motions of a mirror in pitch correspond to rotations of the mirror about x axis and excites a small amount of the TEM01 mode. Similarly, yaw is a rotation about the r axis, exciting a TEM10 mode. For simplicity, we assume that an angular misalignment exists only in pitch and leave TEM01 mode only into the consideration in the rest of this section.

We now consider a simple setup as shown in Fig. B.1 and shows how the linear approximation can be placed. Although a simple example is used, the argument here holds for any optical cavities as long as angular misalignment are sufficiently small. We define a collection of the field vectors containing the two sets of the fields i.e., one set from node 1 and the other from node 2.

$$\vec{E}_{00} \equiv \begin{pmatrix} \langle 00|E\rangle_1 \\ \langle 00|E\rangle_2 \\ \langle 00|E\rangle_3 \end{pmatrix}. \tag{B.3}$$

These fields are related to each other and can be expressed in a matrix form [81],

$$\begin{pmatrix} 0 & 0 & r_1 \mathrm{e}^{-i\Phi_1} \\ r_2 \mathrm{e}^{-i\Phi_2} & 0 & 0 \\ 0 & r_3 \mathrm{e}^{-i\Phi_3} & 0 \end{pmatrix} \begin{pmatrix} \langle 00|E\rangle_1 \\ \langle 00|E\rangle_2 \\ \langle 00|E\rangle_3 \end{pmatrix} + \begin{pmatrix} t_1\langle 00|E\rangle \\ 0 \\ 0 \end{pmatrix} = \begin{pmatrix} \langle 00|E\rangle_1 \\ \langle 00|E\rangle_2 \\ \langle 00|E\rangle_3 \end{pmatrix}, \tag{B.4}$$

where Φ_i $(i = 1, 2, 3)$ is a one-way trip phase shift and r_i are reflectivities of each mirror. The incoming beam is assumed to be perfectly aligned to the cavity. In other words, only a TEM00 mode is pumped into the system.

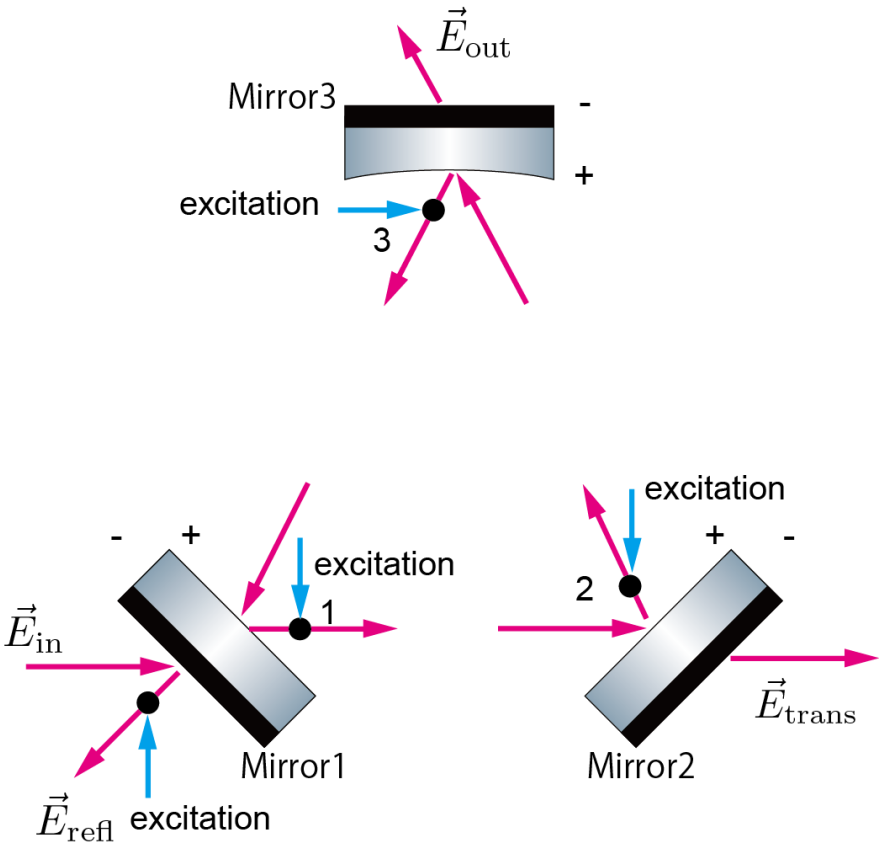

Figure B.1: The electric fields and nodes of a triangular cavity system. Red arrows and black dots represent electric fields and nodes, respectively. The misalignment of input mirror induces perturbation in the promptly reflection. The sign flip upon reflection of fields is labeled by "+" and "−" symbols.

To reduce clutter, we introduce a matrix and vectors as

$$\hat{M}_{00} \equiv \begin{pmatrix} 0 & 0 & r_1 e^{-i\Phi_1} \\ r_2 e^{-i\Phi_2} & 0 & 0 \\ 0 & r_3 e^{-i\Phi_3} & 0 \end{pmatrix}, \tag{B.5}$$

$$\vec{E}_{00,\text{in}} \equiv \begin{pmatrix} t_1 \langle 00|E\rangle \\ 0 \\ 0 \end{pmatrix}. \tag{B.6}$$

Then, one can rewrite Eq. (B.4) as

$$\hat{M}_{00}\vec{E}_{00} + \vec{E}_{00,\text{in}} = \vec{E}_{00}. \tag{B.7}$$

Similarly, the TEM01 mode fields satisfy the following relation,

$$\hat{M}_{01}\vec{E}_{01} = \vec{E}_{01}, \tag{B.8}$$

where

$$\vec{E}_{01} \equiv \begin{pmatrix} \langle 01|E\rangle_1 \\ \langle 01|E\rangle_2 \\ \langle 01|E\rangle_3 \end{pmatrix}, \tag{B.9}$$

$$\hat{M}_{01} \equiv \begin{pmatrix} 0 & 0 & r_1 \mathrm{e}^{-i(\Phi_1+\eta_1)} \\ r_2 \mathrm{e}^{-i(\Phi_2+\eta_2)} & 0 & 0 \\ 0 & r_3 \mathrm{e}^{-i(\Phi_3+\eta_3)} & 0 \end{pmatrix}. \tag{B.10}$$

η_i $(i = 1, 2, 3)$ represents a Gouy phase shift.

Small angular misalignments are introduced in pitch which transfers a fraction of the TEM00 modes to TEM01 and vice versa [102]. We will express these perturbations using normalized rotation angles, $\Theta_i, (i = 1, 2)$. These angles are normalized by divergence angle of the beam, $\lambda/\pi w(z)$, and expressed as

$$\Theta_i \equiv 2\frac{\pi w(z)}{\lambda}\theta_i, \tag{B.11}$$

where the θ_i is a small rotation of each mirror, λ is the wavelength of light and $w(z)$ is a beam size at a position of z [102]. By using this normalized angle, the angular misalignment matrix is defined as

$$\hat{\Theta} \equiv \begin{pmatrix} 0 & 0 & -ir_1 \mathrm{e}^{-i\Phi_1'}\Theta_1 \\ -ir_2 \mathrm{e}^{-i\Phi_2'}\Theta_3 & 0 & 0 \\ 0 & -ir_3 \mathrm{e}^{-i\Phi_3'}\Theta_2 & 0 \end{pmatrix}, \tag{B.12}$$

where Φ_i' represents the one-way trip phase shift for TEM00 or TEM01 modes. Then one can express the fields with pitch angular misalignments as

$$\hat{M}_{00}\vec{E}_{00} + \vec{E}_{00,\mathrm{in}} + \hat{\Theta}\vec{E}_{01} = \vec{E}_{00}, \tag{B.13}$$

$$\hat{M}_{01}\vec{E}_{01} + \hat{\Theta}\vec{E}_{00} = \vec{E}_{01}. \tag{B.14}$$

Since the incoming beam is pure TEM00 mode, TEM01 mode only exists when there is an angular misalignment. The fields of TEM01 mode can be written as

$$\begin{aligned} \vec{E}_{01} &= (I - \hat{M}_{01})^{-1}\hat{\Theta}\vec{E}_{00} \\ &= (I - \hat{M}_{01})^{-1}\hat{\Theta}(I - \hat{M}_{00})^{-1}(\vec{E}_{00,\mathrm{in}} + \hat{\Theta}\vec{E}_{01}), \end{aligned} \tag{B.15}$$

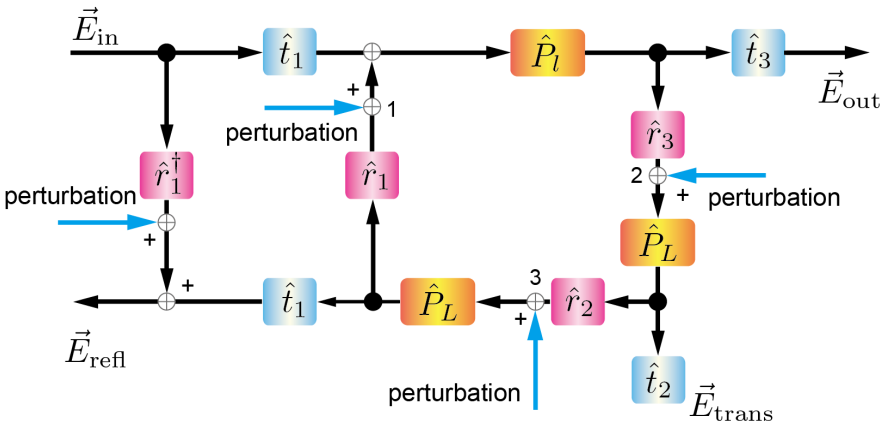

Figure B.2: The block diagram.

where I is the identity matrix Here we substituted $\vec{E}_{00}$ given by Eq. (B.13). Since the angular misalignment angle is so small that one can ignore higher order term $O(\hat{\Theta}^2)$. In fact, this is the essence of our linear approximation. With this linear approximation, TEM01 fields excited by angular misalignments can be expressed as

$$\vec{E}_{01} \approx (I - \hat{M}_{01})^{-1}\hat{\Theta}(I - \hat{M}_{00})^{-1}\vec{E}_{00,\rm in}. \tag{B.16}$$

One can express TEM10 fields introduced by angular misalignments in the same manner.

Our method, in comparison to the previous study which accompanies higher orders to compute the angular response as shown in Fig. 4 in Ref. [102], obviously simplifies the resulting solutions at a cost of losing the accuracy in particular when the amount of misalignment is large. However, in practical experiments, the angular drifts are suppressed by active controls and therefore the amount of misalignment is typically small enough that our approximation is valid.

Besides, another advantage of the linearization is that the entire analysis can be expressed by a block diagram as shown in Fig. B.2 similarly to those used in the classical feedback control theory [106]. Such block diagrams can help ones to acquire comprehensive physical pictures and one can visualize how the misalignment grows up inside the optical cavity.

B.1 Angular Response of a Triangular Cavity

We now consider the case in which a triangular cavity is in the form of isosceles triangle with the length of one side much shorter than the other two.The

incoming laser beam is assumed to be injected to the shorter side. Fig. B.2 shows a block diagram for the system with the mirrors misaligned by some small amounts.

The free-space propagator can be defined as

$$\hat{P}_{L,l} = \mathrm{diag}\left(\mathrm{e}^{-i\Phi_{L,l}}, \mathrm{e}^{-i(\Phi_{L,l}-\eta_{L,l})}, \mathrm{e}^{-i(\Phi_{L,l}-\eta_{L,l})}\right), \tag{B.17}$$

where its subscript, L and l, correspond to the length of propagation. The matrices $\hat{t}$ and $\hat{r}$ denote the transmission and reflection matrix of the mirror as,

$$\hat{r}_i = \mathrm{diag}(r_i, -r_i, r_i), \tag{B.18}$$
$$\hat{t}_i = \mathrm{diag}(t_i, t_i, t_i), \tag{B.19}$$

where the subscripts, $i = 1, 2, 3$, express each mirror of the IMC. It should be noted that the sign of reflectivity for TEM10 is negative due to the mirroring effect which flips the coordinates left-to-right in the horizontal plane. Combining these matrices, the cavity round-trip propagator, $\hat{P}_{\mathrm{rt}}$, can be expressed as

$$\begin{aligned}\hat{P}_{\mathrm{rt}} &\equiv \hat{P}_L\hat{r}_2\hat{P}_L\hat{r}_3\hat{P}_l\hat{r}_1 \\ &= r\mathrm{e}^{-i\Phi_{\mathrm{rt}}}\mathrm{diag}\left(1, -\mathrm{e}^{i\eta_{\mathrm{rt}}}, \mathrm{e}^{i\eta_{\mathrm{rt}}}\right),\end{aligned} \tag{B.20}$$

where $r \equiv r_1 r_2 r_3$ is a total reflectivity of the system which is merely a multiplication of the amplitude reflectivity from all the mirrors and η_{rt} represents a round-trip Gouy phase. Using the round-trip propagator, one can express the fields inside the cavity as

$$\vec{E}_{\mathrm{cav}} = (I - \hat{P}_{\mathrm{rt}})^{-1}\hat{t}_1\vec{E}_{\mathrm{in}}. \tag{B.21}$$

In practical experiments, the phase modulated laser beam which can be split into the carrier and the sidebands is widely used in order to lock the laser to the cavities. Assuming that the cavity is kept resonant for the carrier i.e., $\mathrm{e}^{-i\Phi_{\mathrm{rt}}} = 1$, then one can define the cavity gain for the carrier in the form of each HG modes as

$$G_{00} \equiv \frac{1}{1-r}, \tag{B.22}$$
$$G_{10} \equiv \frac{1}{1+r\mathrm{e}^{i\eta_{\mathrm{rt}}}}, \tag{B.23}$$
$$G_{01} \equiv \frac{1}{1-r\mathrm{e}^{i\eta_{\mathrm{rt}}}}. \tag{B.24}$$

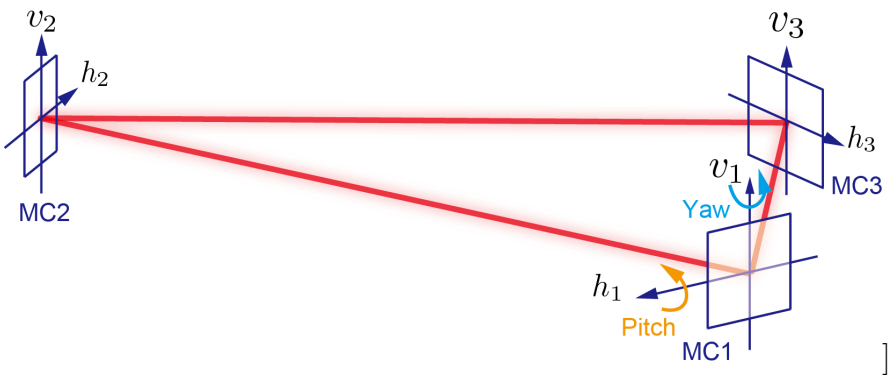

Figure B.3: The block diagram.

It should be noted that the sign of cavity gain is flipped between TEM01 and TEM10 modes due to the mirroring effect for horizontal axis.

On the other hand, the cavity gain for the sidebands which are kept off-resonant can be written as

$$G_{00}^{\mathrm{SB}} \equiv \frac{1}{1+r}. \tag{B.25}$$

Here we assumed that the reflectivity for both upper and lower sidebands are identical. When the reflectivities of mirrors are high i.e., $r_i \approx 1$, the cavity gain for the sidebands are much smaller than that of the carrier. Therefore, ignoring the effect of the sidebands inside the cavity, we will consider only the carrier field for the intra-cavity fields. Then Eq. (B.21) can be rewritten as

$$\vec{E}_{\mathrm{cav}} = \mathrm{diag}(G_{00}, G_{10}, G_{01})\hat{t}_1\vec{E}_{\mathrm{in}}. \tag{B.26}$$

Thus each HG mode excited by angular misalignment is built up inside the cavity as characterized by each cavity gain.

B.2 Beam Spot Response

The response to the beam spot positions is one of the most important properties to understand the behavior of a triangular cavity. The lateral shift of the beam on each mirror can be derived by evaluating the real part of the coefficients for the 01 and 10 modes. For the purpose, let us expand a field into real and imaginary parts as,

$$A\,(U_{00} + CU_{01,10}) \tag{B.27}$$

where C is a complex number which can be expressed using a small beam translation a and a small tilt α [107],

$$C = \frac{a}{w_0} + i\frac{kw_0}{2}\alpha, \tag{B.28}$$

where w_0 is the beam size at its waist and k is the wavenumber. Eq. (B.28) tells the real part of C denotes the beam translation and the imaginary part denotes the beam tilt. Therefore, the beam spot translation can be derived from the real part of normalized coefficient, C, of TEM01/10. The notations of angular tilts and axes on the mirrors are as shown in Fig.B.3.

Evalating the real part of the field on each mirror and approximating all the mirrors to be a perfect reflector i.e., $r_i = 1\,(i = 1, 2, 3)$, one can find the following relation between the mirror tilts and resulting variation in the beam spot as

$$\begin{pmatrix} y_1 \\ y_2 \\ y_3 \end{pmatrix} = -R \begin{pmatrix} g & 1 & g + \frac{2l}{R} \\ 1 & 1 & 1 \\ g + \frac{2l}{R} & 1 & g \end{pmatrix} \begin{pmatrix} \theta_1 \\ \theta_2 \\ \theta_3 \end{pmatrix}, \tag{B.29}$$

where g is the g-factor, defined as

$$g \equiv 1 - \frac{L + l}{R}, \tag{B.30}$$

and $y_i\,(i = 1, 2, 3)$ describe vertical displacements of the beam along the y-axis. A detailed calculation for obtaining Eq. (B.29) is presented in Appendix A.

Since MCs 1 and 3 have an incident angle of approximately $\pi/4$, the y_1 axis and the y_3 axis are rotated $\pi/4$ around the z axis with respect to the y axis [104]. Therefore, an effective misalignment angle in pitch is reduced by $\cos(\pi/4) = 1/\sqrt{2}$, so that

$$\psi_{1,3} = \frac{1}{\sqrt{2}}\theta_{1,3}. \tag{B.31}$$

The axis y is same as the axis on the mirror v. Hence the beam spot displacement on the mirror can be written as

$$\begin{pmatrix} v_1 \\ v_2 \\ v_3 \end{pmatrix} = -\frac{R}{\sqrt{2}} \begin{pmatrix} g & \sqrt{2} & g + \frac{2l}{R} \\ 1 & \sqrt{2} & 1 \\ g + \frac{2l}{R} & \sqrt{2} & g \end{pmatrix} \begin{pmatrix} \psi_1 \\ \psi_2 \\ \psi_3 \end{pmatrix}. \tag{B.32}$$

Eq. (B.32) shows us how the eigenmode of triangular cavity transforms as a function of the tilt of each mirror.

Mirror positions may not always be preferable DoFs. They can be converted into the ones representing the translation and tilt of the beam at the waist, and the spot position on MC2 as

$$\begin{pmatrix} y_{\mathrm{w}} \\ \theta_{\mathrm{w}} \\ v_2 \end{pmatrix} \equiv \begin{pmatrix} \frac{v_1+v_3}{2} \\ \frac{v_1-v_3}{2l} \\ v_2 \end{pmatrix} = \begin{pmatrix} \frac{1}{2} & 0 & \frac{1}{2} \\ \frac{1}{2l} & 0 & -\frac{1}{2l} \\ 0 & 1 & 0 \end{pmatrix} \begin{pmatrix} v_1 \\ v_2 \\ v_3 \end{pmatrix}. \tag{B.33}$$

In addition, we convert the actuation basis into MCs 1 and 3 common and differential motions expressed as

$$\begin{pmatrix} \psi_{\mathrm{c}} \\ \psi_{\mathrm{d}} \\ \psi_2 \end{pmatrix} \equiv \begin{pmatrix} \frac{\psi_1+\psi_3}{2} \\ \frac{\psi_1-\psi_3}{2} \\ \psi_2 \end{pmatrix} = \begin{pmatrix} \frac{1}{2} & 0 & \frac{1}{2} \\ \frac{1}{2} & 0 & -\frac{1}{2} \\ 0 & 1 & 0 \end{pmatrix} \begin{pmatrix} \psi_1 \\ \psi_2 \\ \psi_3 \end{pmatrix}. \tag{B.34}$$

By using these bases, the beam spot response to pitch angular misalignment can be summarized as

$$\begin{pmatrix} y_{\mathrm{w}} \\ \theta_{\mathrm{w}} \\ v_2 \end{pmatrix} = \begin{pmatrix} \sqrt{2}(L-R) & 0 & -R \\ 0 & \sqrt{2} & 0 \\ -\sqrt{2}R & 0 & -R \end{pmatrix} \begin{pmatrix} \psi_{\mathrm{c}} \\ \psi_{\mathrm{d}} \\ \psi_2 \end{pmatrix}. \tag{B.35}$$

Eq. (B.35) shows that misalignment in MC2 cannot access to the tilt at the waist position, and only shift the plane of cavity eigenmode. Common angular tilt rotates cavity eignemode around the center of curvature as shown in figure 19. in [108]. Differential tilt does not change the spot on the curved mirror and the waist, though the tilt at waist is rotated.

In the same way, yaw misalignment can be computed as

$$\begin{pmatrix} x_1 \\ x_2 \\ x_3 \end{pmatrix} = \begin{pmatrix} \xi & -\frac{l}{g} & -\xi \\ -\frac{l}{g} & \frac{L+l}{g} & -\frac{l}{g} \\ -\xi & -\frac{l}{g} & \xi \end{pmatrix} \begin{pmatrix} \phi_1 \\ \phi_2 \\ \phi_3 \end{pmatrix}. \tag{B.36}$$

where xi is defined as $\xi \equiv L + l(1 - L/R)/g$. When the displacements perpendicular to the beam, x_1 and x_3, are projected on each mirror, MCs 1 and 3, the displacements on the mirror surface are enhanced by $1/\cos(\pi/4) = \sqrt{2}$. Therefore, Eq. (B.36) can be written as

$$\begin{pmatrix} h_1 \\ h_2 \\ h_3 \end{pmatrix} = \begin{pmatrix} \sqrt{2}\xi & -\sqrt{2}\frac{l}{g} & -\sqrt{2}\xi \\ -\frac{l}{g} & \frac{L+l}{g} & -\frac{l}{g} \\ -\sqrt{2}\xi & -\sqrt{2}\frac{l}{g} & \sqrt{2}\xi \end{pmatrix} \begin{pmatrix} \phi_1 \\ \phi_2 \\ \phi_3 \end{pmatrix}. \tag{B.37}$$

The bases can be converted in the manner same as that for pitch by using the relationship expressed as

$$\begin{pmatrix} x_{\mathrm{w}} \\ \theta_{\mathrm{w}} \\ h_2 \end{pmatrix} \equiv \begin{pmatrix} \frac{(h_1+h_3)\cos(\pi/4)}{2} \\ \frac{(h_1-h_3)\cos(\pi/4)}{2l} \\ h_2 \end{pmatrix} = \begin{pmatrix} \frac{1}{2\sqrt{2}} & 0 & \frac{1}{2\sqrt{2}} \\ \frac{1}{2\sqrt{2}l} & 0 & -\frac{1}{2\sqrt{2}l} \\ 0 & 1 & 0 \end{pmatrix} \begin{pmatrix} h_1 \\ h_2 \\ h_3 \end{pmatrix}, \tag{B.38}$$

$$\begin{pmatrix} \phi_{\mathrm{c}} \\ \phi_{\mathrm{d}} \\ \phi_2 \end{pmatrix} \equiv \begin{pmatrix} \frac{\phi_1+\phi_3}{2} \\ \frac{\phi_1-\phi_3}{2} \\ \phi_2 \end{pmatrix} = \begin{pmatrix} \frac{1}{2} & 0 & \frac{1}{2} \\ \frac{1}{2} & 0 & -\frac{1}{2} \\ 0 & 1 & 0 \end{pmatrix} \begin{pmatrix} \phi_1 \\ \phi_2 \\ \phi_3 \end{pmatrix}. \tag{B.39}$$

It should be noted that the effect of $\sqrt{2}$ enhancement due to the projection on MCs 1 and 3 is cancelled. Then the beam spot response to yaw misalignments can be expressed as

$$\begin{pmatrix} x_{\mathrm{w}} \\ \theta_{\mathrm{w}} \\ h_2 \end{pmatrix} = \begin{pmatrix} 0 & -2L & 0 \\ \frac{2(-L+R)}{L-R+l} & 0 & -\frac{R}{L-R+l} \\ \frac{2Rl}{L-R+l} & 0 & -\frac{R(L+l)}{L-R+l} \end{pmatrix} \begin{pmatrix} \phi_{\mathrm{c}} \\ \phi_{\mathrm{d}} \\ \phi_2 \end{pmatrix}. \tag{B.40}$$

Eq. (B.40) shows that only misalignment in MCs 1 and 3 differential motion can access to the beam waist shift. The beam waist tilt and MC2 spot position change can be expressed by a combination of MCs 1 and 3 differential motion and MC2 motion.

These results are fully consistent with the previous analysis based on the geometrical argument [108]. Therefore, this linear approximation offers an alternative method to compute variations in the spot positions without elaborating the geometrical analysis.

B.2.1 Wave Front Sensing Signals of the IMC

The WFS technique is sensitive to small tilts of the mirrors. The signals are obtained by demodulating the intensity information detected by quadrant photodiodes (QPDs) [102] in similar manner to the Pound-Drever-Hall (PDH) technique [77]. When one of the mirrors is misaligned, it excites the second lowest-order transverse modes, namely the TEM10 or TEM01 in the carrier. The WFS signals are essentially the interference between the TEM00 of the sidebands and the TEM01 or TEM10 modes of the carrier.

We assume that the incoming light is a purely phase modulated TEM00 mode described as

$$\vec{E}_{\mathrm{in}} = \begin{pmatrix} \langle 00|E\rangle_{\mathrm{in}} \\ 0 \\ 0 \end{pmatrix}. \tag{B.41}$$

Phase modulated input laser beam, which is used in PDH scheme, can be expressed as

$$\langle 00|E\rangle_{\rm in} \approx [J_0(m)\mathrm{e}^{i\Omega t}+J_1(m)\mathrm{e}^{i(\Omega+\omega_m)t} - J_1(m)\mathrm{e}^{i(\Omega-\omega_m)t}] \times \langle 00|E\rangle \tag{B.42}$$

where Ω corresponds to the angular frequency of the carrier field, $\omega_{\rm m}$ is the modulation angular frequency, m is the modulation depth and $J_k(m)$ is Bessel functions of the first kind.

By measuring the differential of reflected field using a horizontally and vertically split photodiodes, QPD, for pitch and yaw, one can obtain the intensity information, $S_{\rm QPD}$, which can be expressed as

$$S_{\rm QPD} \propto \int_0^\infty \mathrm{d}x \left(\vec{E}^\dagger_{\rm refl} \cdot \vec{E}_{\rm refl}\right) - \int_{-\infty}^0 \mathrm{d}x \left(\vec{E}^\dagger_{\rm refl} \cdot \vec{E}_{\rm refl}\right). \tag{B.43}$$

The fields at reflection port of each mode can be calculated by multiplying propagators. The WFS signals are obtained by demodulating the signals, $S_{\rm QPD}$, with the modulation angular frequency, $\omega_{\rm m}$. After some math, one can derive the WFS signals described as

$$\mathrm{WFS} = iP_0J_0(m)J_1(m)\big[U^*_{00}(G_{00}G_{10,01}\mathrm{e}^{i\bar{\eta}}\Theta U_{10,01}) - U_{00}(G_{00}G_{10,01}\mathrm{e}^{i\bar{\eta}}\Theta U_{10,01})^*\big], \tag{B.44}$$

where P_0 denotes the optical power of the input laser beam and $\bar{\eta}$ is a spcific Gouy phase which depends on the misaligned mirror. When we apply parameters of KAGRA IMC, the WFS signals can be calculated as shown in Fig. B.4.

B.3 Implication to Experiment

The IMC has three DoFs for angular misalignments in both pitch and yaw. On the other hand, the number of observable DoFs by the WFS technique is only two since the WFSs sense the difference between the two beams — the incoming and intra-cavity beams. In this section, the observable degrees of freedom (DoFs) of the IMC are discussed for the case where the incoming beam is injected to the shorter side of the IMC such as KAGRA [20]. For the other case where the incoming beam is injected to longer side of the IMC such as aLIGO [23], the results are shown in Appendix B for completeness.

The singular value decomposition (SVD) is one of the useful tools in order to understand what DoFs can or cannot be sensed. The SVD is widely used

for data analysis [109]. The WFS signals contain beam tilt and translation components and are expressed as bellow by using a sensing matrix $\hat{S}$,

$$\begin{pmatrix} \text{tilt} \\ \text{trans.} \end{pmatrix} = \hat{S} \begin{pmatrix} \theta_1 \\ \theta_2 \\ \theta_3 \end{pmatrix}, \tag{B.45}$$

where $\hat{S}$ is a 2×3 matrix and its elements can be written by using the cavity gain and Gouy phase shift. This sensing matrix can be expressed by geometrical parameters with high reflective approximation ($r_i \approx 1$) and incoming beam is pure TEM00 mode. Then we will apply SVD to rewrite them to determine which DoFs are observable by the WFS technique.

In the case of the geometry used in KAGRA [20], one can obtain the relationship between the WFS signals and mirror tilt angles in pitch as

$$\begin{pmatrix} \text{tilt} \\ \text{trans.} \end{pmatrix}_{\text{Pitch}} = \sqrt{2}\gamma w_0 \begin{pmatrix} g\gamma & 0 & -g\gamma \\ -g & -\sqrt{2} & -g \end{pmatrix} \begin{pmatrix} \psi_1 \\ \psi_2 \\ \psi_3 \end{pmatrix}, \tag{B.46}$$

where $\gamma \equiv (L + l)/z_{\text{R}}$, and w_0 is beam size at its waist. Adopting the SVD analysis, one can arrive at

$$\hat{S}_{\text{Pitch}} = \sqrt{2}\gamma w_0 I \begin{pmatrix} g\gamma & 0 & 0 \\ 0 & 1 & 0 \end{pmatrix} \begin{pmatrix} 1 & 0 & -1 \\ -g & -\sqrt{2} & -g \\ 1 & -\sqrt{2}g & 1 \end{pmatrix}. \tag{B.47}$$

It is clear that one the DoF shown in the lowest row in the rightmost matrix. On the other hand, the first and second rows are observable. They correspond to MCs 1 and 3 differential motion and the combination of MCs 1 and 3 common and MC2 motion, respectively. Comparing to Eq. (B.35), one can identify that the observable DoFs correspond to the beam waist tilt and translation.

For the case of yaw, the sensing matrix can be written as

$$\begin{pmatrix} \text{tilt} \\ \text{trans.} \end{pmatrix}_{\text{Yaw}} = \sqrt{2}\gamma w_0 \begin{pmatrix} -g & 1 & -g \\ -g\gamma & 0 & g\gamma \end{pmatrix} \begin{pmatrix} \phi_1 \\ \phi_2 \\ \phi_3 \end{pmatrix}. \tag{B.48}$$

The decomposed form can be expressed as

$$\hat{S}_{\text{Yaw}} = \sqrt{2}\gamma w_0 I \begin{pmatrix} g & 0 & 0 \\ 0 & g\gamma & 0 \end{pmatrix} \begin{pmatrix} -1 & \frac{1}{g} & -1 \\ -1 & 0 & 1 \\ 1 & 2g & 1 \end{pmatrix}. \tag{B.49}$$

The observable DoFs are the combination of MCs 1 and 3 common and MC2 motion and MCs 1 and 3 differential motion. Similarly to the pitch case, these observable DoFs correspond to the beam waist tilt and translation. Therefore, when the beam is injected to the shorter side of the IMC, the beam waist tilt and translation are observable.

B.4 Conclusion

We have presented the linear approximation method that can simplify the analytical calculation of angular response of optical cavities. The method enables us not only to simplify the calculation but also to make equivalent block diagrams which can bring comprehensive pictures.

The method was applied to a triangular cavity called the input mode cleaning cavity. The angular response to the shift in the beam spots and the WFS signals of the IMC in gravitational wave detectors were explicitly given by this approach. The results are consistent with the previous report which conducted a completely different approach — geometrical analysis.

Finally, the WFS sensing matrices are analyzed via the singular value decomposision scheme in order to study the observable DoFs of the IMC. When the incoming beam is injected to the shorter side of the IMC, the observable DoFs by the WFS scheme are determined to be the beam waist tilt and translation.

The linear approximation method presented in this article can be applied to optical systems which are more involved, including the main interferometer of gravitational wave detectors. The linear approximation method should be able to give deeper insight into the fundamental comprehension of the gravitational wave interferometers.

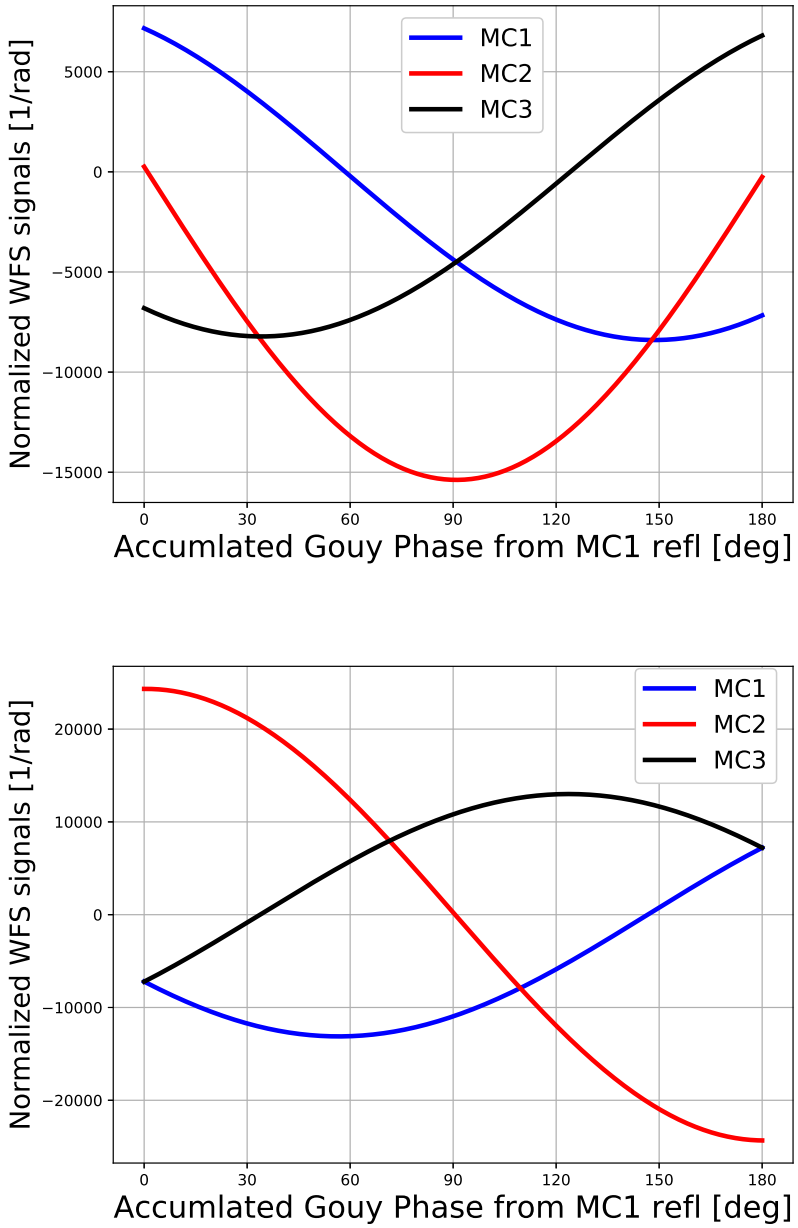

Figure B.4: The WFS signals of KAGRA IMC. Upper figure shows the pitch WFS signals and lower figure shows that of yaw.

Acknowledgements

First of all, I am grateful to professor Yoichi Aso, who has supervised me. He gave me a good opportunities to work on the various fields in gravitational wave detection.

I thank Dr. Kiwamu Izumi for giving me an attractive and instructive talk. I learned the interferometric techniques from him.

I would like to professor Matthew Evans, and Dr. Slawomir Gras who supervised me when I visited MIT LIGO Lab.

I would like to thank the people who have helped me out — Ryutaro Takahashi, Tomotada Akutsu, Matteo Leonardi, Naohisa Sato, Naoatsu Hirata, Yoshikazu Namai, Ayako Ueda, Koki Okutomi, Yoshinori Fujii, Kunihiko Hasegawa and Naoki Aritomi.

The administrative office members in NAOJ, Mizuho Yoshizumi, Mikiko Harada, Megumi Ohyama, Mie Ueda, and Eri Sakamoto supported me by taking care of paperwork when purchasing something, attending meetings, going on trips, and so on. Thanks to their help, I was able to concentrate my research.

This work was supported by JSPS KAKENHI Grant Number JP18K03681 and JSPS Grant-in-Aid for Specially Promoted Research 26000005. This work was partially supported by Research Fund for Students (2017) of the Department of Astronomical Science, The Graduate University for Advanced Studies, SOKENDAI.

Finally, I thank my parents, brother, and grandparents for allowing me to do the research.

Bibliography

[1] A. Einstein. Die grundlage der allgemeinen relativitätstheorie [adp 49, 769 (1916)]. *Annalen der Physik*, 14(S1):517–571, 2005.

[2] Albert Einstein. Über Gravitationswellen. *Sitzungsberichte der Königlich Preußischen Akademie der Wissenschaften (Berlin*, pages 154–167, January 1918.

[3] Bernard Schutz. *A first course in general relativity; 2nd ed.* Cambridge Univ. Press, Cambridge, 2009.

[4] S. L. Shapiro and S. A. Teukolsky. *Black Holes, White Dwarfs, and Neutron Stars*. Wiley-VCH, 1983.

[5] Michele Maggiore. *Gravitational waves*. Oxford University Press, 2008.

[6] R. Abbott et al. Gwtc-2: Compact binary coalescences observed by ligo and virgo during the first half of the third observing run, 2020.

[7] Curt Cutler and Daniel E. Holz. Ultrahigh precision cosmology from gravitational waves. *Phys. Rev. D*, 80:104009, Nov 2009.

[8] B. P. Abbott et al. Search for the isotropic stochastic background using data from advanced ligo's second observing run. *Phys. Rev. D*, 100:061101, Sep 2019.

[9] P.R. Saulson. *Fundamentals of Interferometric Gravitational Wave Detectors*. World Scientific, 1994.

[10] Brian J. Meers. Recycling in laser-interferometric gravitational-wave detectors. *Phys. Rev. D*, 38:2317–2326, Oct 1988.

[11] Yuhang Zhao et al. Frequency-dependent squeezed vacuum source for broadband quantum noise reduction in advanced gravitational-wave detectors. *Phys. Rev. Lett.*, 124:171101, Apr 2020.

[12] L. McCuller, C. Whittle, D. Ganapathy, K. Komori, M. Tse, A. Fernandez-Galiana, L. Barsotti, P. Fritschel, M. MacInnis, F. Matichard, K. Mason, N. Mavalvala, R. Mittleman, Haocun Yu, M. E. Zucker, and M. Evans. Frequency-dependent squeezing for advanced ligo. *Phys. Rev. Lett.*, 124:171102, Apr 2020.

[13] Gabriela González. Suspensions thermal noise in the LIGO gravitational wave detector. *Classical and Quantum Gravity*, 17(21):4409–4435, oct 2000.

[14] Kentaro Somiya and Kazuhiro Yamamoto. Coating thermal noise of a finite-size cylindrical mirror. *Phys. Rev. D*, 79:102004, May 2009.

[15] Kazuhiro Agatsuma, Koji Arai, Masa-Katsu Fujimoto, Seiji Kawamura, Kazuaki Kuroda, Osamu Miyakawa, Shinji Miyoki, Masatake Ohashi, Toshikazu Suzuki, Ryutaro Takahashi, Daisuke Tatsumi, Souichi Telada, Takashi Uchiyama, and Kazuhiro Yamamoto and. Thermal-noise-limited underground interferometer CLIO. *Classical and Quantum Gravity*, 27(8):084022, apr 2010.

[16] Shinji Miyoki, Takayuki Tomaru, Hideki Ishitsuka, Masatake Ohashi, Kazuaki Kuroda, Daisuke Tatsumi, Takashi Uchiyama, Toshikazu Suzuki, Nobuaki Sato, Tomiyoshi Haruyama, Akira Yamamoto, and Takakazu Shintomi. Cryogenic contamination speed for cryogenic laser interferometric gravitational wave detector. *Cryogenics*, 41(5):415 – 420, 2001.

[17] Yuki Ikushima, Rui Li, Takayuki Tomaru, Nobuaki Sato, Toshikazu Suzuki, Tomiyoshi Haruyama, Takakazu Shintomi, and Akira Yamamoto. Ultra-low-vibration pulse-tube cryocooler system – cooling capacity and vibration. *Cryogenics*, 48(9):406 – 412, 2008.

[18] Takashi Uchiyama, Shinji Miyoki, Souichi Telada, Kazuhiro Yamamoto, Masatake Ohashi, Kazuhiro Agatsuma, Koji Arai, Masa-Katsu Fujimoto, Tomiyoshi Haruyama, Seiji Kawamura, Osamu Miyakawa, Naoko Ohishi, Takanori Saito, Takakazu Shintomi, Toshikazu Suzuki, Ryutaro Takahashi, and Daisuke Tatsumi. Reduction of thermal fluctuations in a cryogenic laser interferometric gravitational wave detector. *Phys. Rev. Lett.*, 108:141101, Apr 2012.

[19] Kentaro Somiya. Detector configuration of KAGRA–the japanese cryogenic gravitational-wave detector. *Classical and Quantum Gravity*, 29(12):124007, jun 2012.

[20] Yoichi Aso, Yuta Michimura, Kentaro Somiya, Masaki Ando, Osamu Miyakawa, Takanori Sekiguchi, Daisuke Tatsumi, and Hiroaki Yamamoto. Interferometer design of the kagra gravitational wave detector. *Phys. Rev. D*, 88:043007, Aug 2013.

[21] T Akutsu et al. First cryogenic test operation of underground km-scale gravitational-wave observatory KAGRA. *Classical and Quantum Gravity*, 36(16):165008, jul 2019.

[22] T Akutsu and othres. Overview of KAGRA : Detector design and construction history. *Progress of Theoretical and Experimental Physics*, 08 2020. ptaa125.

[23] Chris L. Mueller et al. The advanced LIGO input optics. *Review of Scientific Instruments*, 87(1):014502, 2016.

[24] Shigeo Nagano et al. Development of a light source with an injection-locked Nd:YAG laser and a ring-mode cleaner for the TAMA 300 gravitational-wave detector. *Review of Scientific Instruments*, 73(5):2136–2142, 2002.

[25] Y Akiyama et al. Vibration isolation system with a compact damping system for power recycling mirrors of KAGRA. *Classical and Quantum Gravity*, 36(9):095015, apr 2019.

[26] Tomohiro Yamada, Takayuki Tomaru, Toshikazu Suzuki, Takafumi Ushiba, Nobuhiro Kimura, Suguru Takada, Yuki Inoue, and Takaaki Kajita. High performance heat conductor with small spring constant for cryogenic applications, 2020.

[27] K. Komori, Y. Michimura, and K. Somiya. "Parameters for the latest estimated sensitivity of KAGRA", JGW-T1707038, 2017.

[28] J. D. E. Creighton and W. G. Anderson. , *Gravitational-Wave Physics and Astronomy: An Introduction to Theory, Experiment and Data Analysis*. Wiley-VCH, New York, 2011.

[29] Lee Samuel Finn and David F. Chernoff. Observing binary inspiral in gravitational radiation: One interferometer. *Phys. Rev. D*, 47:2198–2219, Mar 1993.

[30] R. Abernathy Matthew et al. Einstein gravitational wave Telescope (ET) conceptual design study, ET-0106C-10. https://tds.ego-gw.it/ql/?c=7954, 2010.

[31] Jessica Steinlechner, Iain W. Martin, Jim Hough, Christoph Krüger, Sheila Rowan, and Roman Schnabel. Thermal noise reduction and absorption optimization via multimaterial coatings. *Phys. Rev. D*, 91:042001, Feb 2015.

[32] Kieran Craig, Jessica Steinlechner, Peter G. Murray, Angus S. Bell, Ross Birney, Karen Haughian, Jim Hough, Ian MacLaren, Steve Penn, Stuart Reid, Raymond Robie, Sheila Rowan, and Iain W. Martin. Mirror coating solution for the cryogenic einstein telescope. *Phys. Rev. Lett.*, 122:231102, Jun 2019.

[33] R. Abbott, , et al. Gw190521: A binary black hole merger with a total mass of 150 $M_{\odot}$. *Phys. Rev. Lett.*, 125:101102, Sep 2020.

[34] B. P. Abbott et al. Binary black hole population properties inferred from the first and second observing runs of advanced LIGO and advanced virgo. *The Astrophysical Journal*, 882(2):L24, sep 2019.

[35] R X Adhikari et al. A cryogenic silicon interferometer for gravitational-wave detection. *Classical and Quantum Gravity*, 37(16):165003, jul 2020.

[36] C. A. Swenson. Recommended values for the thermal expansivity of silicon from 0 to 1000 k. *Journal of Physical and Chemical Reference Data*, 12(2):179–182, 1983.

[37] Stefan Hild, Harald Lück, Walter Winkler, Ken Strain, Hartmut Grote, Joshua Smith, Michaela Malec, Martin Hewitson, Benno Willke, James Hough, and Karsten Danzmann. Measurement of a low-absorption sample of oh-reduced fused silica. *Appl. Opt.*, 45(28):7269–7272, Oct 2006.

[38] Jérôme Degallaix, Christophe Michel, Benoit Sassolas, Annalisa Allocca, Gianpetro Cagnoli, Laurent Balzarini, Vincent Dolique, Raffaele Flaminio, Danièle Forest, Massimo Granata, Bernard Lagrange, Nicolas Straniero, Julien Teillon, and Laurent Pinard. Large and extremely low loss: the unique challenges of gravitational wave mirrors. *J. Opt. Soc. Am. A*, 36(11):C85–C94, Nov 2019.

[39] Eiichi Hirose, GariLynn Billingsley, Liyuan Zhang, Hiroaki Yamamoto, Laurent Pinard, Christoph Michel, Danièle Forest, Bill Reichman, and Mark Gross. Characterization of core optics in gravitational-wave detectors: Case study of kagra sapphire mirrors. *Phys. Rev. Applied*, 14:014021, Jul 2020.

[40] Anja Schroeter, Ronny Nawrodt, Roman Schnabel, Stuart Reid, Iain Martin, Sheila Rowan, Christian Schwarz, Torsten Koettig, Ralf Neubert, Matthias Thürk, Wolfgang Vodel, Andreas Tünnermann, Karsten Danzmann, and Paul Seidel. On the mechanical quality factors of cryogenic test masses from fused silica and crystalline quartz, 2007.

[41] R Nawrodt, A Zimmer, T Koettig, C Schwarz, D Heinert, M Hudl, R Neubert, M Thürk, S Nietzsche, W Vodel, P Seidel, and A Tünnermann. High mechanical q-factor measurements on silicon bulk samples. *Journal of Physics: Conference Series*, 122:012008, jul 2008.

[42] M. J. Keevers and M. A. Green. Absorption edge of silicon from solar cell spectral response measurements. *Applied Physics Letters*, 66(2):174–176, 1995.

[43] Simon C. Tait, Jessica Steinlechner, Maya M. Kinley-Hanlon, Peter G. Murray, Jim Hough, Graeme McGhee, Felix Pein, Sheila Rowan, Roman Schnabel, Cassady Smith, Lukas Terkowski, and Iain W. Martin. Demonstration of the multimaterial coating concept to reduce thermal noise in gravitational-wave detectors. *Phys. Rev. Lett.*, 125:011102, Jul 2020.

[44] G. Cole, W. Zhang, M. Martin, et al. Tenfold reduction of brownian noise in high-reflectivity optical coatings. *Nature Photon*, 7:644–650, Aug 2013.

[45] Garrett D. Cole, Wei Zhang, Bryce J. Bjork, David Follman, Paula Heu, Christoph Deutsch, Lindsay Sonderhouse, John Robinson, Chris Franz, Alexei Alexandrovski, Mark Notcutt, Oliver H. Heckl, Jun Ye, and Markus Aspelmeyer. High-performance near- and mid-infrared crystalline coatings. *Optica*, 3(6):647–656, Jun 2016.

[46] A V Cumming, K Craig, I W Martin, R Bassiri, L Cunningham, M M Fejer, J S Harris, K Haughian, D Heinert, B Lantz, A C Lin, A S Markosyan, R Nawrodt, R Route, and S Rowan. Measurement of the mechanical loss of prototype GaP/AlGaP crystalline coatings for future gravitational wave detectors. *Classical and Quantum Gravity*, 32(3):035002, jan 2015.

[47] Jessica Steinlechner, Alexander Khalaidovski, and Roman Schnabel. Optical absorption measurement at 1550 nm on a highly-reflective si/SiO 2 coating stack. *Classical and Quantum Gravity*, 31(10):105005, apr 2014.

[48] R. Birney, J. Steinlechner, Z. Tornasi, S. MacFoy, D. Vine, A. S. Bell, D. Gibson, J. Hough, S. Rowan, P. Sortais, S. Sproules, S. Tait, I. W. Martin, and S. Reid. Amorphous silicon with extremely low absorption: Beating thermal noise in gravitational astronomy. *Phys. Rev. Lett.*, 121:191101, Nov 2018.

[49] Jun-Yen Tewg, Yue Kuo, and Jiang Lu. Suppression of crystallization of tantalum oxide thin film by doping with zirconium. *Electrochemical and Solid-State Letters*, 8(1):G27, 2005.

[50] Huang-Wei Pan, Shun-Jin Wang, Ling-Chi Kuo, Shiuh Chao, Maria Principe, Innocenzo M. Pinto, and Riccardo DeSalvo. Thickness-dependent crystallization on thermal anneal for titania/silica nm-layer composites deposited by ion beam sputter method. *Opt. Express*, 22(24):29847–29854, Dec 2014.

[51] Ling-Chi Kuo, Huang-Wei Pan, Chi-Li Chang, and Shiuh Chao. Low cryogenic mechanical loss composite silica thin film for low thermal noise dielectric mirror coatings. *Opt. Lett.*, 44(2):247–250, Jan 2019.

[52] Oliver Burmeister, Michael Britzger, André Thüring, Daniel Friedrich, Frank Brückner, Karsten Danzmann, and Roman Schnabel. All-reflective coupling of two optical cavities with 3-port diffraction gratings. *Opt. Express*, 18(9):9119–9132, Apr 2010.

[53] Frank Brückner, Daniel Friedrich, Tina Clausnitzer, Michael Britzger, Oliver Burmeister, Karsten Danzmann, Ernst-Bernhard Kley, Andreas Tünnermann, and Roman Schnabel. Realization of a monolithic high-reflectivity cavity mirror from a single silicon crystal. *Phys. Rev. Lett.*, 104:163903, Apr 2010.

[54] Y. Enomoto. X arm cavity characterization with good spot positions. http://klog.icrr.u-tokyo.ac.jp/osl/?r=7307, 2018.

[55] Y. Enomoto. Fogged ITMY. http://klog.icrr.u-tokyo.ac.jp/osl/?r=9377, 2019.

[56] Werner G. Baechler. Cryopumps for research and industry. *Vacuum*, 37(1):21 – 29, 1987.

[57] Jessica Steinlechner and Iain W. Martin. Thermal noise from icy mirrors in gravitational wave detectors. *Phys. Rev. Research*, 1:013008, Aug 2019.

[58] Kunihiko Hasegawa, Tomotada Akutsu, Nobuhiro Kimura, Yoshio Saito, Toshikazu Suzuki, Takayuki Tomaru, Ayako Ueda, and Shinji Miyoki. Molecular adsorbed layer formation on cooled mirrors and its impacts on cryogenic gravitational wave telescopes. *Phys. Rev. D*, 99:022003, Jan 2019.

[59] Kunihiko Hasegawa. *Optical and thermal study of molecular thin layers on cryogenic mirrors in next-generation gravitational wave telescopes.* PhD thesis, The University of Tokyo, 2020.

[60] B. Schmitt, E. Quirico, F. Trotta, and W. M. Grundy. *Optical Properties of Ices From UV to Infrared*, pages 199–240. Springer Netherlands, Dordrecht, 1998.

[61] Satoshi Tanioka, Kunihiko Hasegawa, and Yoichi Aso. Optical loss study of molecular layer for a cryogenic interferometric gravitational-wave detector. *Phys. Rev. D*, 102:022009, Jul 2020.

[62] S L Danilishin, C Gräf, S S Leavey, J Hennig, E A Houston, D Pascucci, S Steinlechner, J Wright, and S Hild. Quantum noise of non-ideal sagnac speed meter interferometer with asymmetries. *New Journal of Physics*, 17(4):043031, apr 2015.

[63] L. Pinard, C. Michel, B. Sassolas, L. Balzarini, J. Degallaix, V. Dolique, R. Flaminio, D. Forest, M. Granata, B. Lagrange, N. Straniero, J. Teillon, and G. Cagnoli. Mirrors used in the ligo interferometers for first detection of gravitational waves. *Appl. Opt.*, 56(4):C11–C15, Feb 2017.

[64] Jean-Yves Vinet, Violette Brisson, and Stefano Braccini. Scattered light noise in gravitational wave interferometric detectors: Coherent effects. *Phys. Rev. D*, 54:1276–1286, Jul 1996.

[65] Ryutaro Takahashi, Koji Arai, Seiji Kawamura, and Michael R. Smith. Direct measurement of the scattered light effect on the sensitivity in tama300. *Phys. Rev. D*, 70:062003, Sep 2004.

[66] J. M. Elson, J. P. Rahn, and J. M. Bennett. Relationship of the total integrated scattering from multilayer-coated optics to angle of incidence, polarization, correlation length, and roughness cross-correlation properties. *Appl. Opt.*, 22(20):3207–3219, Oct 1983.

[67] James E. Harvey, Narak Choi, Sven Schroeder, and Angela Duparré. Total integrated scatter from surfaces with arbitrary roughness, correlation widths, and incident angles. *Optical Engineering*, 51(1):1 – 12, 2012.

[68] Chris A. Mack. Analytic form for the power spectral density in one, two, and three dimensions. *Journal of Micro/Nanolithography, MEMS, and MOEMS*, 10(4):1 – 3, 2011.

[69] M. Punturo et al. The einstein telescope: a third-generation gravitational wave observatory. *Classical and Quantum Gravity*, 27(19):194002, sep 2010.

[70] Masaki Ando, Keita Kawabe, and Kimio Tsubono. Signal-separation technique for a power-recycled interferometric gravitational wave detector. *Physics Letters A*, 237(1):13 – 20, 1997.

[71] Vincent Kofman, Jiao He, Inge Loes ten Kate, and Harold Linnartz. The refractive index of amorphous and crystalline water ice in the UV–vis. *The Astrophysical Journal*, 875(2):131, apr 2019.

[72] David T Limmer and David Chandler. Theory of amorphous ices. *Proceedings of the National Academy of Sciences of the United States of America*, 111(26):9413—9418, July 2014.

[73] Stephen G. Warren and Richard E. Brandt. Optical constants of ice from the ultraviolet to the microwave: A revised compilation. *Journal of Geophysical Research: Atmospheres*, 113(D14), 2008.

[74] T Akutsu et al. Overview of KAGRA: Detector design and construction history. *Progress of Theoretical and Experimental Physics*, 08 2020. ptaa125.

[75] Ichiro Ushijima, Masao Takamoto, and Hidetoshi Katori. Operational Magic Intensity for Sr Optical Lattice Clocks. *Phys. Rev. Lett.*, 121:263202, Dec 2018.

[76] Anthony E. Siegman. *Lasers*. University Science Books, 1986.

[77] R. W. P. Drever, J. L. Hall, F. V. Kowalski, J. Hough, G. M. Ford, A. J. Munley, and H. Ward. Laser phase and frequency stabilization using an optical resonator. *Applied Physics B*, 31(2):97–105, Jun 1983.

[78] S Courts. One year stability of Cernox™ and DT-670-SD silicon diode cryogenic temperature sensors operated at 77 K. *Cryogenics*, 107:103050, 2020.

[79] Kenji Numata, Jordan Camp, Michael A. Krainak, and Lew Stolpner. Performance of planar-waveguide external cavity laser for precision measurements. *Opt. Express*, 18(22):22781–22788, Oct 2010.

[80] H. MacLeod. *Thin-Film Optical Filters*. CRC Press, 03 2010.

[81] Andreas Freise and Kenneth Strain. Interferometer techniques for gravitational-wave detection. *Living Reviews in Relativity*, 13(1):1, Feb 2010.

[82] Satoshi Tanioka, Gui guo Ge, Keiko Kokeyama, Masayuki Nakano, Junegyu Park, and Kiwamu Izumi. Angular response of a triangular optical cavity analyzed by a linear approximation method, 2020.

[83] A. Brooks. aLIGO LGO logbook. https://alog.ligo-wa.caltech.edu/aLOG/index.php?callRep=34853, 2017.

[84] Christopher Wipf. personal communication.

[85] E. A. Donley, T. P. Heavner, F. Levi, M. O. Tataw, and S. R. Jefferts. Double-pass acousto-optic modulator system. *Review of Scientific Instruments*, 76(6):063112, 2005.

[86] Jiao He, Kinsuk Acharyya, and Gianfranco Vidali. STICKING OF MOLECULES ON NONPOROUS AMORPHOUS WATER ICE. *The Astrophysical Journal*, 823(1):56, may 2016.

[87] R. Kersevan and J.-L. Pons. Introduction to molflow+: New graphical processing unit-based monte carlo code for simulating molecular flows and for calculating angular coefficients in the compute unified device architecture environment. *Journal of Vacuum Science & Technology A*, 27(4):1017–1023, 2009.

[88] Brett Shapiro, Rana X. Adhikari, Odylio Aguiar, Edgard Bonilla, Danyang Fan, Litawn Gan, Ian Gomez, Sanditi Khandelwal, Brian Lantz, Tim MacDonald, and Dakota Madden-Fong. Cryogenically cooled ultra low vibration silicon mirrors for gravitational wave observatories. *Cryogenics*, 81:83 – 92, 2017.

[89] Ryan Lawrence, Michael Zucker, Peter Fritschel, Phil Marfuta, and David Shoemaker. Adaptive thermal compensation of test masses in advanced LIGO. *Classical and Quantum Gravity*, 19(7):1803–1812, mar 2002.

[90] S. Gras, H. Yu, W. Yam, D. Martynov, and M. Evans. Audio-band coating thermal noise measurement for advanced ligo with a multimode optical resonator. *Phys. Rev. D*, 95:022001, Jan 2017.

[91] S. Gras and M. Evans. Direct measurement of coating thermal noise in optical resonators. *Phys. Rev. D*, 98:122001, Dec 2018.

[92] R. Adhikari et al. "Mariner Overview", LIGO-L2000216, 2020.

[93] Herbert B. Callen and Richard F. Greene. On a theorem of irreversible thermodynamics. *Phys. Rev.*, 86:702–710, Jun 1952.

[94] Yu. Levin. Internal thermal noise in the ligo test masses: A direct approach. *Phys. Rev. D*, 57:659–663, Jan 1998.

[95] Erika D'Ambrosio, Richard O'Shaugnessy, Kip Thorne, Phil Willems, Sergey Strigin, and Sergey Vyatchanin. Advanced LIGO: non-gaussian beams. *Classical and Quantum Gravity*, 21(5):S867–S873, feb 2004.

[96] Benoît Mours, Edwige Tournefier, and Jean-Yves Vinet. Thermal noise reduction in interferometric gravitational wave antennas: using high order TEM modes. *Classical and Quantum Gravity*, 23(20):5777–5784, sep 2006.

[97] S. Gras, D. G. Blair, and L. Ju. Opto-acoustic interactions in gravitational wave detectors: Comparing flat-top beams with gaussian beams. *Phys. Rev. D*, 81:042001, Feb 2010.

[98] D. Shoemaker, R. Schilling, L. Schnupp, W. Winkler, K. Maischberger, and A. Rüdiger. Noise behavior of the garching 30-meter prototype gravitational-wave detector. *Phys. Rev. D*, 38:423–432, Jul 1988.

[99] P.R. Saulson. *Fundamentals of Interferometric Gravitational Wave Detectors*. World Scientific, 1994.

[100] Euan Morrison, Brian J. Meers, David I. Robertson, and Henry Ward. Automatic alignment of optical interferometers. *Appl. Opt.*, 33(22):5041–5049, Aug 1994.

[101] Nergis Mavalvala, Daniel Sigg, and David Shoemaker. Experimental test of an alignment-sensing scheme for a gravitational-wave interferometer. *Appl. Opt.*, 37(33):7743–7746, Nov 1998.

[102] Yaron Hefetz, Nergis Mavalvala, and Daniel Sigg. Principles of calculating alignment signals in complex resonant optical interferometers. *J. Opt. Soc. Am. B*, 14(7):1597–1606, Jul 1997.

[103] Daniel Sigg and Nergis Mavalvala. Principles of calculating the dynamical response of misaligned complex resonant optical interferometers. *J. Opt. Soc. Am. A*, 17(9):1642–1649, Sep 2000.

[104] Andreas Freise, Daniel Brown, and Charlotte Bond. Finesse, Frequency domain INterferomEter Simulation SoftwarE, 2013.

[105] Matthew Evans. Optickle LIGO Document T070260-00. https://dcc.ligo.org/public/0027/T070260/001/Optickle.pdf.

[106] B. Lurie and P. Enright. *Classical Feedback Control: With MATLAB*. Automation and Control Engineering. Taylor & Francis, 2000.

[107] K. Kawabe, N. Mio, and K. Tsubono. Automatic alignment-control system for a suspended Fabry–Perot cavity. *Appl. Opt.*, 33(24):5498–5505, Aug 1994.

[108] F Kawazoe, R Schilling, and H Lück. Eigenmode changes in a misaligned triangular optical cavity. *Journal of Optics*, 13(5):055504, apr 2011.

[109] Orly Alter, Patrick O. Brown, and David Botstein. Singular value decomposition for genome-wide expression data processing and modeling. *Proceedings of the National Academy of Sciences*, 97(18):10101–10106, 2000.